INFORMATION TO USERS

Electron-induced surface radiation damage in V_2O_5, ReO_3 and CaF_2

Ai, Xiaohong Rebecca, Ph.D.

Northwestern University, 1992

NORTHWESTERN UNIVERSITY

ELECTRON-INDUCED SURFACE RADIATION DAMAGE

IN V_2O_5, ReO_3 AND CaF_2

A DISSERTATION

SUBMITTED TO THE GRADUATE SCHOOL
IN PARTIAL FULFILLMENT OF THE REQUIREMENTS

for the degree

DOCTOR OF PHILOSOPHY

Field of Materials Science and Engineering

By

Xiaohong Rebecca Ai

EVANSTON, ILLINOIS

December 1992

ABSTRACT

ELECTRON-INDUCED SURFACE RADIATION DAMAGE
IN V_2O_5, ReO_3 and CaF_2

Xiaohong Rebecca Ai

The effects of electron irradiation in V_2O_5, ReO_3 and CaF_2 have been investigated as a function of controlled experimental parameters such as electron beam fluxes and energies, crystal orientations and surface environments. *In-situ* structural and chemical changes, the desorbed species and the rate at which the damaged layer extended into the bulk were evaluated by high resolution electron microscopy (HREM), electron diffraction, multislice image simulation, x-ray photoelectron spectroscopy (XPS) and mass spectrometry.

For V_2O_5 , electron irradiation resulted in the preferential loss of positive oxygen ions at the surface and consequently a phase transformation to lower oxides in both non-UHV and UHV environments. The phase transformation route depended strongly on electron beam fluxes and energies, and crystal orientations. Three new phases: V_4O_9, β-V_6O_{13} and VO were observed and they had well defined orientation relationships with V_2O_5. The kinetics of the phase transformation were determined to be flux dependent. To explain this observation, a theoretical model for the process as an one-dimensional problem with oxygen loss from the surface and coupled interface- and diffusion-controlled growth was proposed. The model reproduced the flux dependence of the phase transformation routes.

ReO_3 was found to be stable under electron beam irradiation in a carbon-free environment. In the presence of carbon, an electron-stimulated reaction occurred, resulting in the formation of a high temperature, high pressure metastable phase, ReC. The reaction was independent of electron beam fluxes and energies, and crystal orientations. ReC has a preferred orientation of [110]. The kinetics of the reaction were linear.

The damage in CaF_2 was a two-step process: the metallization to Ca resulted from the desorption of fluorine atoms followed by the oxidation of Ca to CaO by the oxygen-containing species in the vacuum. The surface environment was observed to be a major factor in the microstructure of CaO.

An Auger electron spectrometer (AES) for a Hitachi UHV H-9000 electron microscope has been developed. Preliminary studies showed that the AES has better a surface sensitivity than the Gatan parallel electron energy loss spectrometer.

Approved:

_____

Professor Laurence D. Marks (Thesis Advisor)
Department of Materials Science and Engineering
The Robert R. McCormick School of Engineering and Applied Science
Northwestern University
Evanston, Illinois
December 1992

" If you lose your head and you give up, then you neither live nor win "

Charles Whitman

To My Parents

ACKNOWLEDGEMENTS

TABLE OF CONTENTS

LIST OF FIGURES

LIST OF TABLES

CHAPTER 1   INTRODUCTION AND THEORY

§1.1   INTRODUCTION

Studies of electron-induced surface desorption and reactions are of both scientific and technological interest, and have therefore been the focus of many investigations in recent years. From the theoretical point of view, investigations of such processes provide insight into the nature of surface bonding (Madey 1984). The technological importance is in many areas. For example, the surface of a space shuttle experiences electron irradiation that stimulates surface desorption and reactions, resulting in materials degradation (Fellas 1981). In the laboratory, electron irradiation is encountered in every instrument that uses electron beams as a probe. In these cases, the electron-induced desorption and damage may be an unwanted side effect. However the processes of stimulated desorption have some unique characteristics that make them valuable for many applications. For example, a focused electron beam can be used to control surface reaction with high spacial resolution. Materials growth, modification and patterning using such methods is a very active research area (Osgood 1985 and Kern 1986).

This study is funded by the Air Force Office of Scientific Research and is motivated by concerns about the durability and performance of the structural, thermal, optical and electrical materials of spacecraft in long duration Low Earth Orbits (LEO, 200 - 600 km altitude) missions. The atmosphere of LEO mainly consists of atomic oxygen, micrometeoroids, electrons and photons. Under the combined irradiation, it was found that the surface of spacecraft experiences severe degradation. The damage includes

erosion, oxidation of metallic thin films, increased resistivity and shuttle glow, all of which limit the survivability of spacecraft in LEO (Bareiss 1986 and Green 1986). This initiated the need to systematically study the damage in the harsh environment of LEO and resulted in efforts to develop new erosion-resistant materials and coatings. In the past few years, our research group in the Center for Surface Radiation Damage Studies at Northwestern University has performed a systematic survey on the effects of electron irradiation on metal oxides which are commonly used in solar cell arrays and as protective coatings against atomic oxygen irradiation (Bank 1985). The work in this thesis has mainly focused on V_2O_5, ReO_3 and CaF_2. V_2O_5 and ReO_3 have been chosen due to their interesting electrical properties. While V_2O_5 is an semiconductor, ReO_3 is a metallic oxide, representing two broad types of metal oxides. V_2O_5 is a maximum valence transition metal oxide that undergoes electron-stimulated desorption via the inter-atomic Auger transition (Feibelman 1979) and has been studied extensively. However most of the studies have been focused on the surface chemical changes, very little is known about the surface structure left behind, where electron microscopy could make a contribution. CaF_2 is chosen to extend the existing studies to an new group of materials, alkaline earth fluorides. They have a number of significant differences from transition metal oxides. They are often attacked by water and oxygen and generally have very symmetric structures. Consequently under the electron irradiation surface reaction could be important in these materials.

The objectives of this study are three fold. First is to characterize the effects of electron irradiation as a function of controlled experimental parameters such as electron

beam energies and fluxes, crystal orientations and surface environments. The second is to elucidate the mechanisms by which the structures and properties are changed. The third is to study the kinetics of the damage processes. The approaches to the objectives are two. One is to detect the desorbing particles using mass spectrometry. The second is to characterize the surface left behind. X-ray photoelectron spectroscopy is used to study the changes of surface chemistry. Electron microscopy is used to study the changes of surface structures.

The development of the microscopy-compatible AES was driven by the need for a surface sensitive technique for chemical analysis during UHV electron microscopy. While the sensitivity of a parallel electron energy loss spectrometer has been proven to be limited to monolayer (Marks 1991), in many applications submonolayer sensitivity is often desired.

An understanding and survey of the theory of electron-induced surface radiation damage is very important to this study and presented in Chapter 1. Chapter 2 describes the experimental techniques and instruments used for this investigation. Detailed development of the AES is presented in Chapter 3. The effects of electron irradiation in V_2O_5 are reported in Chapter 4. The results on ReO_3 and CaF_2 are discussed in Chapter 5. Future research is suggested in Chapter 6.

§1.2 THEORY OF ELECTRON-INDUCED RADIATION DAMAGE

When electrons pass through a solid, they interact strongly with both atomic electrons and atomic nuclei via Columbic forces. In the process electrons are scattered, the direction of the momentum is changed and an appreciable amount of energy is transferred to the specimen. The interactions can be generally divided into two classes: elastic and inelastic.

During elastic scattering, the *kinetic energy* and *momenta* of the particles involved in the collision are conserved. For a small scattering angle, the energy transferred is less than 0.01 eV and is therefore negligible. Small angle elastic scattering accounts for the contrast in the electron image. However, for large scattering angles, a significant amount of energy can be transferred. Under certain conditions, the transferred energy can exceed the threshold energy E_d, beyond which an atom can be displaced from its lattice site to an interstitial site. This process is commonly known as ballistic knock-on displacement.

In inelastic scattering, the *total energy* and the *momenta* of the particles involved in the collision are conserved. The *kinetic energy* however is not a conserved quantity and part of it is converted to the electronic excitation energy as a result of electron-electron interaction.

There are a number of possible inelastic processes which can be divided into four categories (Reimer 1984):

(1) Excitation of phonons. In this process, energy is transferred to the solid by the excitation of phonons (lattice vibrations), i.e., heat. The energy deposited is typically on the order of 20 meV -1 eV.

(2) Excitation of plasmons. A plasmon is a collective oscillation of valence and conduction electrons.

(3) Ionization of inner atomic shell. Electrons in the inner shell are ionized, lead to the atom in an excited state with a core hole. If the core hole is filled by an electron from an outer shell, the excess energy is released as photons (x-ray) or to ionize atomic electrons, which are emitted as Auger electrons. The excess energy can also be transferred to the kinetic energy of atomic nuclei, causing permanent displacement.

(4) Creation of locally bound electron-hole pairs (exciton). In this process, a core electron is excited to a higher energy level, leaving behind a core hole. An exciton is a self trapped electron-hole pair.

The electron-induced damage processes can be induced by both elastic and inelastic interactions and are divided into three types: 1) ballistic knock-on displacement which is basically a large angle elastic scattering; 2) electronic excitation resulted from inelastic interaction between the incident electrons and atomic electrons and 3) thermal effects result from the thermal spike due to the excitation of phonons. The end results of these three types of damage are similar. In the bulk such processes result in the creation of point defects. At the surface the end result is the desorption of surface atoms. In this section the detailed theoretical background of the damage processes by knock-on and electronic excitation will be reviewed. In an electron microscope, the temperature rise during electron microscopy is generally less than $100°C$ (Buckett 1991). The thermal effects therefore can be neglected in this study.

§1.2.1 Knock-On

Knock-on collision is a process of direct momentum transfer resulting from large angle Ruthford (elastic) scattering. If a sufficient amount of energy is transferred, an atom will be displaced from its lattice site to an interstitial site. In some cases, the displaced atom may gain enough kinetic energy to displace other atoms, resulting in a displacement cascade or a focused replacement collision sequence (RCS). When the knock-on process takes place near the surface, surface atoms may be ejected into the vacuum.

In an electron microscope, a knock-on collision can be treated as an elastic collision between a stationary particle of mass M and a swift electron of mass m_e with a velocity of v. Using the conservation of kinetic energy and momenta, it can be shown that the energy transferred in one electron-nucleus collision is given by

$$T = \frac{2E_k}{Mc^2} (E_k + 2m_e c^2) \sin^2\frac{\theta}{2} \qquad (1.1)$$

where θ = the scattering angle

$$E_k = \text{kinetic energy} = \frac{1}{2} m_e v^2$$

The maximum transferred energy at $\theta = 180°$ is given by

$$T_{max} = \frac{2E_k}{Mc^2} (E_k + 2m_e c^2) \qquad (1.2)$$

The cross section for knock-on was first derived by Ruthford for nonrelativistic charged particles. For electrons the cross section is given by

$$\sigma_n = \frac{\pi b^2}{4} \cos(\frac{\theta}{2})\csc^3(\frac{\theta}{2}) \qquad (1.3)$$

where $b = \dfrac{2eQ}{\mu v^2}$

with: Q = charge of the particle in the solid

$$\mu = \frac{m_e M}{m_e + M}$$

The cross-section for the relativistic particles was first derived by Mott (1929) and

later simplified by McKlinley *et al* (1948):

$$\sigma_n = Z^2 4\pi a_H^2 U_R^2 \{ \frac{1-\beta^2}{m_e^2 c^4 \beta^4} \}(\frac{T_{max}}{T_{min}} + 2\pi\alpha\beta(\frac{T_{max}}{T_{min}})^{\frac{1}{2}} - $$
$$(\beta^2 + \pi\alpha\beta)\ln(\frac{T_{max}}{T_{min}}) - (1 - 2\pi\alpha\beta)\} \qquad (1.4)$$

where a_H = Bohr radius = 5.29×10^{-12} m

U_R = Rydberg energy = 13.6 eV

Z = Atomic number

α = Z/137

β = v/c

T_{min} = Energy of a vibrational quanta $\approx 10^{-2}$ eV

In order to displace an atom from its lattice site, a minimum amount of energy is

required to be transferred, which is defined as the displacement energy E_d. E_d is related

to the binding energy of the solid since atomic bonds must be broken before an atom can

be displaced. In ionic solids the binding energy arises from the cohesion provided by the

lattice Columbic energy. To displace an atom permanently, an excess amount of energy over the cohesive energy is required because the atom needs to jump across several saddle points to form a stable Frenkel pair. A simple estimation of the displacement energy in an ionic solid is about several times of the cohesive energy (Hobbs 1979).

The critical primary electron energy at which the kinetic energy transferred by knock-on equals to E_d is defined as the threshold energy and can be calculated using Equation (1.1). For most ionic solids, the threshold energy is on the order of 100 keV (Buckett 1991).

§1.2.2 Electronic Excitation

It is now well known that changes can be caused by electrons with energies well below the threshold energy for knock-on displacement. For such an effect to occur, a process by which an ion or a neutral atom desorbs from the surface with an acquired kinetic energy of a few eV (Clinton 1977) is required. Direct momentum transfer by low energy electrons is negligible. Therefore the energy transfer in this process must be attributed to electronic excitations.

From the microscopic point of view, electron-induced surface desorption or damage follows a sequence of four steps (Tully 1983):

(1) Excitation. Incident electrons transfer their kinetic energy to atoms in the solid via electronic excitation in at a time scale of 10^{-16} sec.

(2) Localization. The excitation energy is spatially localized for a time period longer than one atomic vibration ($\sim 10^{-15}$ sec).

(3) Displacement. In this period the excitation energy is transferred to the kinetic energy of the atomic nuclei via decay of the excited state. The time scale of this step is on the order of 10^{-14} - 10^{-13} sec. The end result is the formation of Frenkel pairs or the desorption of surface atoms.

(4) Modification. In this step the escaping species near the surface can be modified as a result of electron interactions or de-excitations which occur on a time scale of 10^{-13} sec.

Many mechanisms for electron-stimulated surface desorption have been proposed and reviewed in recent books (DIET I 1983, DIET II 1985, DIET III, DIET IV) and papers (Chuang 1983, Knoteck 1984, Madey 1984, Menzel 1986, Ho 1988 and Avouris 1989). In this section three basic mechanisms, the Menzel-Gomer-Redhead (MGR), the Knoteck-Feibelman (K-F) and the Pooley-Hersh mechanisms, will be discussed.

The MGR Mechanism

Because of its general nature, the MGR mechanism has been in many ways viewed as a general description for desorption induced by electronic transition. It is applicable to both ionic and covalent systems. The idea of this mechanism is very simple and involves a Frank-Condon electronic transition to a repulsive state. In this respect, the MGR model is analogous to dissociation of gas phase molecules. However, the surface can recapture or neutralize an excited atom, which dramatically reduces the desorption yield. The desorption yield is therefore given by

$$\sigma = \sigma_e P_e = \sigma_e \exp(-\alpha r) \tag{1.6}$$

where σ_e is the excitation cross-section, P_e is the escape probability, r is the distance from the surface, and α is a constant. The mechanism is schematically illustrated in Figure 1.1 and operates as follows: a valence electron from the bonding state is excited to an anti- or non-bonding state. As a result of this Frank-Condon excitation, the excited atom finds itself on a repulsive curve and begins to move away from the surface. As it moves away, there is a probability $P_q = 1 - \exp(-\alpha r)$ that the valence hole is filled, quenching the excited atom back to the ground state. The primary quenching mechanisms are resonant electron tunneling and Auger transitions. The requirement for a desorption to take place is that the excited atom stay at the repulsive curve long enough that sufficient kinetic energy can be gained before a quenching process occurs. If that is the case, the quenching process will result in the desorption of a particle in the ground state. If no quenching transitions take place, the desorption of a particle in the excited state is possible. Three major predictions of the MGR model have been verified. The first is that the threshold energy should be the excitation energy from the bonding state to the anti-bonding state. The second is that there should be an isotope effect, since particles of smaller mass on the same surface are moving faster and therefore have a better chance of escaping before the quenching processes take place. The third is that the desorption process has a low cross-section comparing to the dissociation of gas-phase molecules because the substrate provides a large amount of electrons for neutralization of the valance hole created by the initial excitation. Although the MGR model provides a
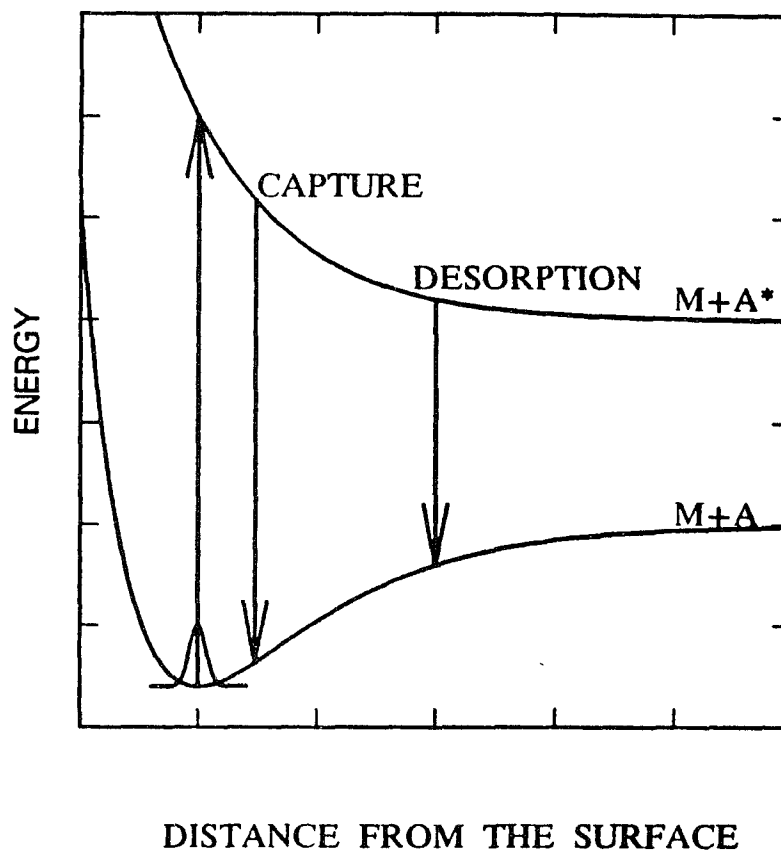
Figure 1.1 Schematic potential energy curves illustrating stimulated desorption by the MGR model (Avouris 1989).

generalized scheme for DIET, the initial excitations, the specific nature of the repulsive states and the relevant quenching processes are not specified. To account for these, many elaborated mechanisms have been proposed, most notably by Atoniewicz (1980) and Brenig (1983).

The K-F Mechanism

The K-F mechanism was first proposed to explain the desorption of positive ions from maximum valance transition metal oxides and is applicable mainly to ionic solids. Maximum valence transition metal oxides are oxides in which the cations have the electronic configurations of noble gases. This mechanism can be best illustrated using the energy level of TiO_2 as shown in Figure 1.2a. In TiO_2, Ti^{4+} is ionized to the electronic configuration of Argon and has no conduction electrons. The highest occupied state is 3p, laying ~34 eV below the Fermi level. If a core electron in a 3p level is ionized, the dominant core-hole decay process will be an inter-atomic Auger decay because there are no electrons in the Ti^{4+} conduction band. The decay of an O(2s) electron will release ~31 eV energy which is sufficient to ionize one or two more electrons from the O(2s) level. During this process an O^{2-} loses two or three electrons and became an O^o or an O^+. The Madelung potential experienced by the anion consequently reverses from attraction to repulsion as shown in Figure 1.2b, providing the driving force for the desorption of an O^+.

The K-F mechanism predicts two experimental observations which the MGR fails: 1) the desorption threshold and 2) the desorption of positive oxygen ions. Another

(a)

(b)
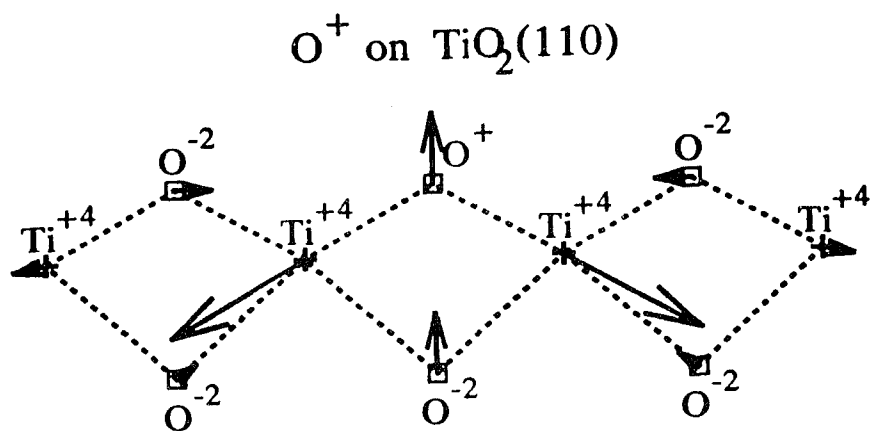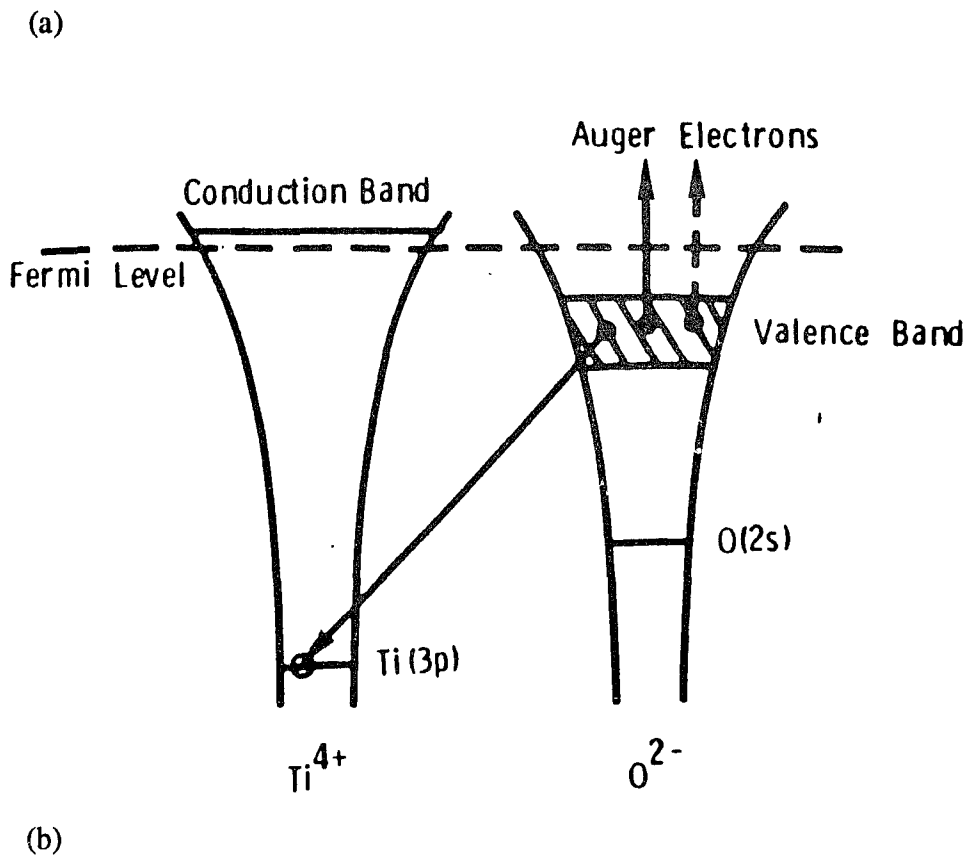
Figure 1.2   a) Schematic illustration of the K-F mechanism by an inter-atomic Auger decay (Knoteck 1978).

b) The forces arising from the formation of a positive ion at an anion site int TiO_2 (Avouris).

important prediction by the K-F mechanism is that the sub-maximal valence metal oxides should be less susceptible to damage via Auger decay because the intra-atomic processes dominate the decay. This prediction has been experimentally verified. Little desorption from materials such as NiO, Cr_2O_3, Ti_2O_3, VO_2 and Fe_2O_3 was observed (Knotek 1978, 1979, Lin 1979a, 1979b and Niehus 1981). While the argument that the desorption of positive ions is driven by the reversal madelung potential is plausible, it is difficult to account for the desorption of neutrals and negative ions (Hock 1978, Ayukhanov 1977, Yu 1979a and 1979b). On metals the potential would be screened long before the particles have the time to acquire the kinetic energy.

The Pooley-Hersh Mechanism

The exciton mechanism was proposed by Pooley (1965) and Hersh (1966) independently to explain color-center formation in alkaline halides. In this mechanism, the energy transfer is achieved by non-radiative decay of the self trapped excitons (self trapped electron-hole pairs) created by electronic excitations. Before going into the detailed description of the mechanism, it is convenient to define some point defects.

F-center: an electron trapped in an anion vacancy.

H-center: a hole trapped at an anion interstitial.

V_k-center: an electron trapped at a dihalide molecule.

Figure 1.3 shows the various stages of this mechanism. Figure 1.4 shows the energies of the ground state and the electron-hole pair state with respect to the energy of the perfect crystal in its lowest energy state "A" as a function of the separation of two anions
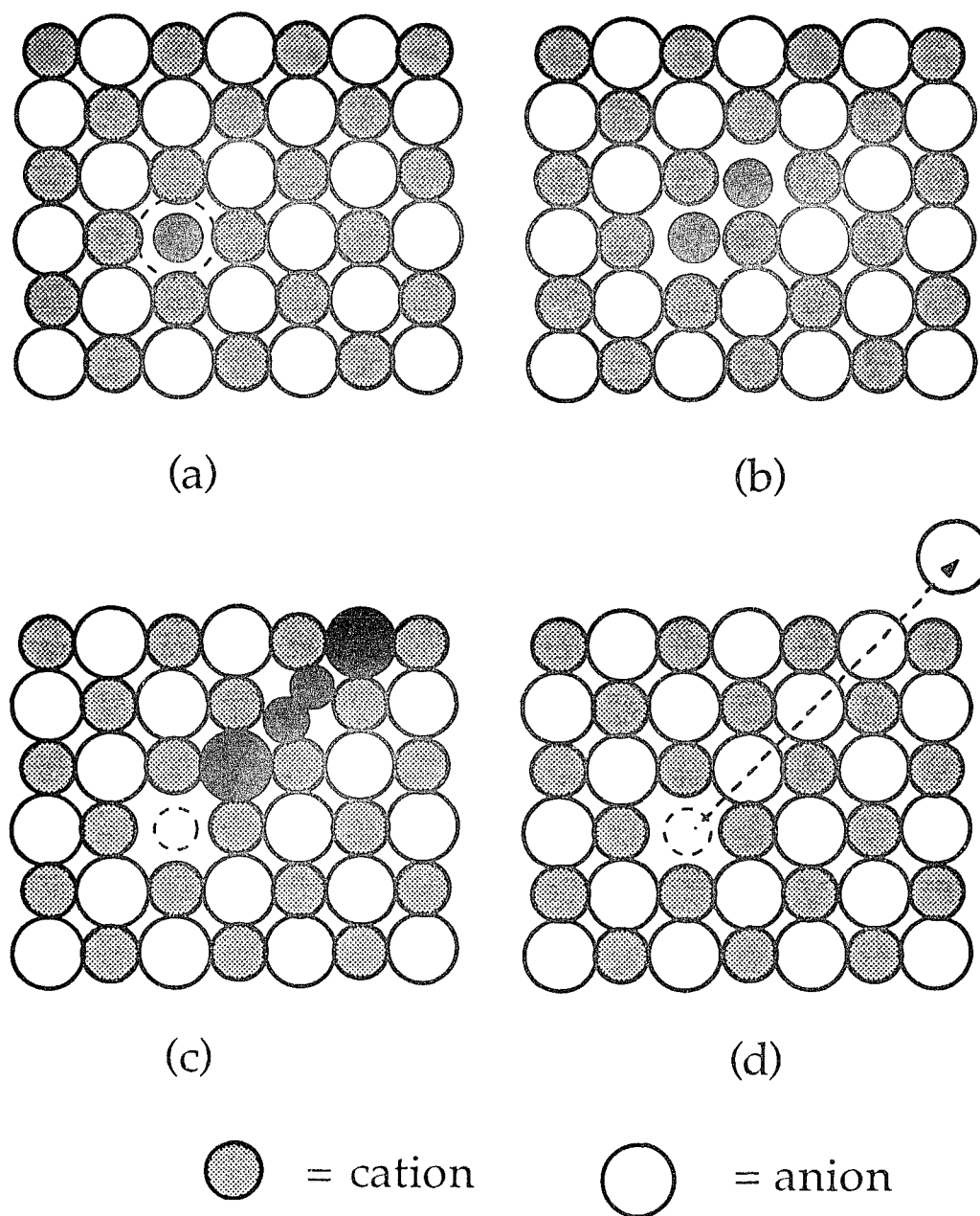
Figure 1.3   Schematic illustration of various stages of the Pooley-Hersh mechanism. (a) A self trapped exciton; (b) Relaxation of the exciton to one of its neighboring anion; (c) Replacement sequence leads to formation of a F-center and a H-center in the bulk; (d) Desorption of an atom at the surface.
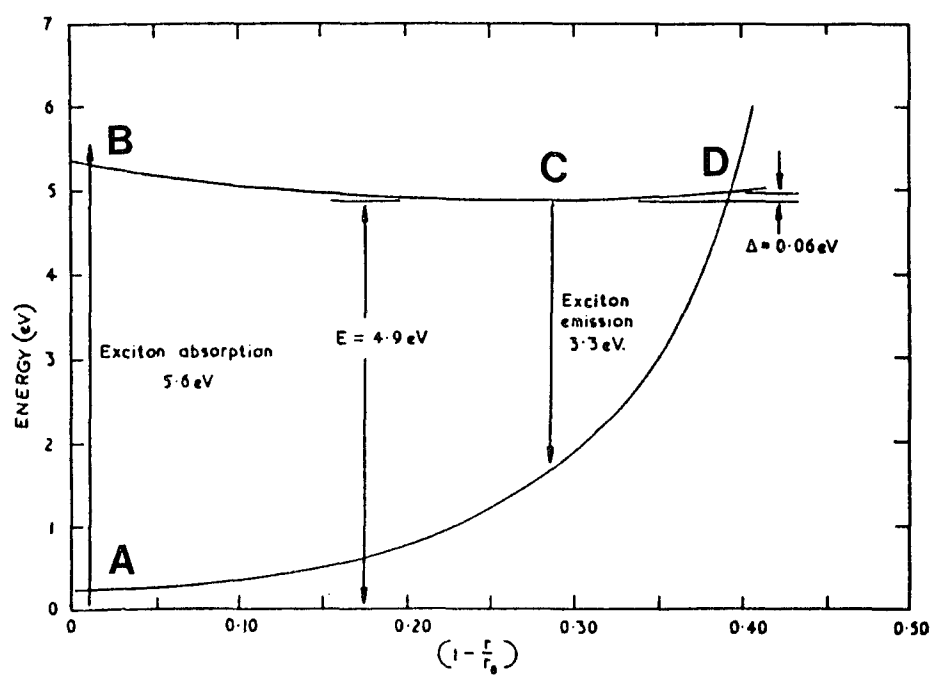
Figure 1.4 Energies of the ground state and the electron-hole pair state in KI as a function of the separation of the two halogen ions (Pooley 1965).

in KI. The process begins with the formation of an exciton by exciting an electron to a higher energy level. This exciton is at an excited state represented by "B" in Figure 1.4 and consequently will relax to a lower energy state "C" by forming an excited V_k-center with one of the halogen neighbors. At this stage, the electron at the higher energy level has a probability to recombine with the hole in the excited V_k-center, releasing an excess amount of energy which provides the activation energy ($\Delta E = 0.06$ eV) for the radiationless transition from the excited state "C" to the ground state "D". This transition gives 4.9 eV energy to the two halogen atoms with the momentum vector laying along [110]. If the energy is shared unequally, the more energetic halogen atom may start a replacement sequence, leading to the formation of a F-center and a H-center in the bulk, or a F-center and a desorbing neutral halogen atom at the surface. Several of the predictions of this model have been verified. For example, particles desorbed preferentially along [110] have been observed (Townsend 1976)

Experimental Observation

Since the first discovery of the desorption phenomena, vast amounts of data has been accumulated. In this section some primary observations are summarized. More complete reviews of the experimental findings can be found in the literature (Menzel 1975, 1982, Madey 1971, 1977, 1982 and Feibelman 1985). Here some major observations are summarized.

Products: Desorption of ions, mostly positive, but also negative (Liu 1981), and neutrals from surfaces of adsorbate-covered metal, semiconductor and ionic solids have

been observed.

Relative Abundances: Neutrals are the most abundant desorbed species found so far, especially in the case of primary valence excitations where only a few percent of the total desorbed particles are ions (Jeland 1973).

Total Desorption Cross Section: The total cross-section varies from 10^{-17} to 10^{-23} cm^{-2} (Madey 1971). The ion desorption cross sections are a factor of 10^2 or more smaller than the neutral cross sections.

Thresholds: For adsorbate-covered metal surfaces the thresholds for desorption are in the valence region. For ionic surfaces the thresholds are the excitation energies required to create cation core holes.

Energy Distributions: These have been investigated for positive ions only. The energies range from 0 up to 12 eV, with the maxima on the order of a few eV.

Angular Distributions: Positive ions desorb from the surface as a focussed beam in most cases. The beams usually have full width half maxima of 15 to 30° around the surface normal. No isotropic distributions have been observed.

CHAPTER 2 INSTRUMENTATION AND EXPERIMENTAL TECHNIQUES

The instruments used in this study include a Hitachi H-9000, a Hitachi UHV H-9000 high resolution electron microscopes, and a VG ESCA system. High resolution electron microscopy and electron diffraction were used for structural characterization. AES and XPS were employed for surface chemical analysis. Mass spectrometry was used to detect the desorbing species during electron irradiation.

§2.1 HITACHI H-9000 AND UHV H-9000 HIGH RESOLUTION ELECTRON MICROSCOPES

The Hitachi H-9000 high resolution electron microscope consists of three chambers: the electron gun house, microscope column and the viewing chamber. The microscope has a stable operation vacuum of 2×10^{-7} torr and a point to point resolution of better than 1.8 Å. The acceleration voltage can be varied from 100 kV to 300 kV. The microscope uses a La_6B filament to obtain a low energy spread and high brightness electron beam for high resolution imaging. Samples are loaded into the microscope using a double tilt ($\pm 10°$) top entry sample cartridge. An Apollo DN 3500 workstation is attached to the microscope so that images acquired on-line can be stored and analyzed in more detail later. A liquid nitrogen cold trap is provided near the sample region to reduce the hydrocarbon contaminations on samples during experimental observations.

The Hitachi UHV H-9000 high resolution electron microscope was developed by Hitachi in collaboration with Drs. L. D. Marks and P. C. Stair at Northwestern University.

19

It is essentially the same microscope as the H-9000. However the pumping and sealing systems have been completely redesigned to achieve a stable operation pressure of 2 x 10^{-10} torr. With a fully equipped surface science sample transfer chamber (STC), the UHV H-9000 has achieved the ultimate goal of surface studies at atomic resolution using electron microscopes in a clean and controlled environment. Detailed UHV design philosophy of the microscope has been given by Bonevich (1991).

Figure 2.1 shows the schematic of the microscope. The microscope column is very similar to that of the H-9000. The microscope has a point to point resolution of 2.0 Å. It uses a double tilt ($\pm$ 10°) side entry sample cartridge. The chemical analysis capabilities of the microscope include a transmission PEELS (Gatan 666 PEELS system) for bulk chemical analysis, an AES for surface chemical analysis and an Ametek quadruple mass spectrometer for monitoring the residual gases.

The STC is designed to provide a suitable environment for sample transfer and preparation. It is pumped by a 60 l/s ion pump and a 400 l/s titanium sublimation pump built in house to maintain the UHV. A turbo-molecular pump is used for three purposes. The first is to rough pump the STC. The second is to differentially pump the ion gun. The third is to provide pumping for the sample transfer mechanism designed by Bonevich (1991). Instruments attached to the STC include:

1)   A Perking-Elmer model 04-3000 triple source ion gun capable of delivering ion beams of energies of up to 5 keV and beam currents of up to 25 mA to a spot as small as 2 mm in diameter on samples. It is used to sputter clean and thin samples as well as a radiation source.

UHV-H9000 HREM

Transfer System

Auger

Leak Valve

Mass Spec.

Turbo pump

Ion Gun

PEELS/ CCD-TV
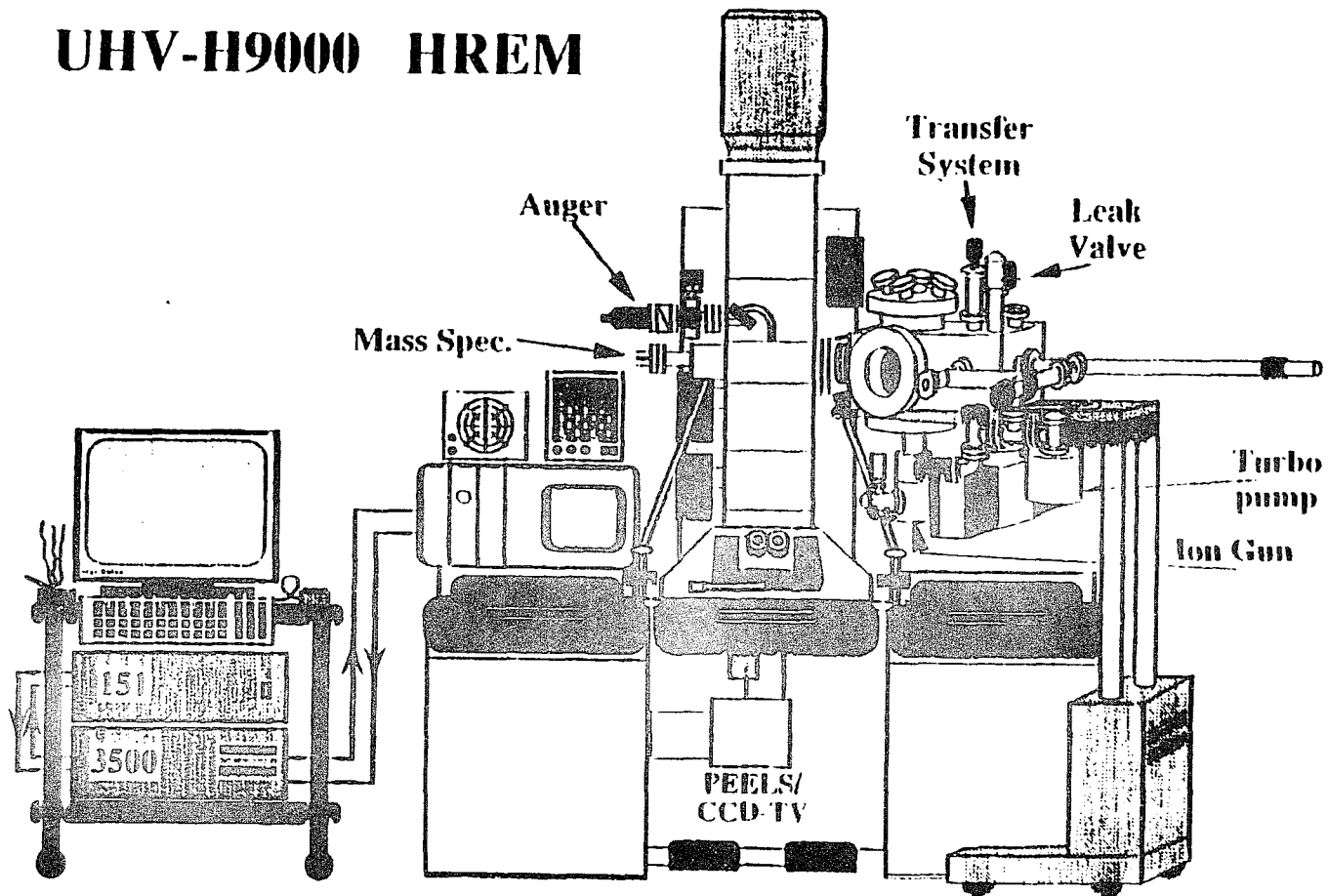
Figure 2.1   Schematic illustration of the Hitachi ultra high vacuum H-9000 high resolution electron microscope (Courtesy of J. E. Bonevich).

2)   A Kimball Physics model EMG-4 electron gun capable of providing electron beams of energies of up to 10 keV and emission currents of up to 3 mA in a spot as small as 1 mm in diameter. It is used for thermal annealing and as a radiation source.

3)   A white band optical annealing source for alternative thermal annealing

4)   An Ametek quadruple mass spectrometer for residual gas analysis.

5)   LEED/Auger optics for surface structural and chemical characterization.

6)   A magnetic coupled transfer rod to transfer samples between the STC and the microscope column through a gate valve.

7)   A home made evaporator for metallic thin film deposition.

8)   A UHV gas leak valve for gas dosing experiments.

The STC is fully bakable to 200°C. The pressure in the chamber after a 12 hour bakeout is on the order of 2×10^{-10} torr.

§2.2   VG ESCA SYSTEM

VG ESCA system consists of an airlock for sample introduction, an UHV preparation chamber for sample outgassing, a XPS analytical chamber and a secondary ion mass spectrometry (SIMS) chamber. The individual chambers are isolated by gate valves. Both the XPS and SIMS chambers have a base pressure on the order of 5×10^{-11} torr. The XPS chamber is equipped with a twin anode (Mg K_α and Al K_α) x-ray source and a concentric hemispherical energy analyzer (CHA). The SIMS chamber is equipped with a quadruple mass spectrometer and a low energy electron gun as a radiation source.

§2.3 HIGH RESOLUTION ELECTRON MICROSCOPY OF SURFACES

In recent years a resolution limit of better than 1.8 Å in transmission electron microscopes permits the study surface structures at the atomic level either in plane view or in profile. In addition to its high resolution, HREM for surface studies have several advantages compared to the standard surface analytical techniques. First of all, information from a small area can be linked with information from a larger area. Second, surface and bulk features can be imaged at the same time, allowing studies of relations between the two. Third, the information on crystallography obtained from the image can be combined with the information on chemical composition obtained from microanalysis.

Several techniques have been developed to make use of HREM for surface studies. Profile imaging developed by Drs. Marks and Smith (Marks 1983,1984,1985 and Smith 1985) takes full advantage of the high resolution of a TEM. The principle of this technique is schematically depicted by Figure 2.2. The edge of a thin crystal is oriented such that the incident electron beam is parallel to a zone axis and thus also to a row of atoms in the surface plane. Each row of atoms then will be projected to the image plane. Under certain imaging conditions, when a row of atoms is projected onto a small area of the image to give a single spot, without interfering with the next nearest row of atoms, the image will be a faithful representation of a monolayer in the object. This image provides an one-to-one mapping of the atomic potential, where "black dots" represent atomic columns and "white dots" represent channels between them. Using this technique the arrangement of surface atoms, surface reconstructions, surface faceting, and the presence of chemically different layers may be visible. For example the surface
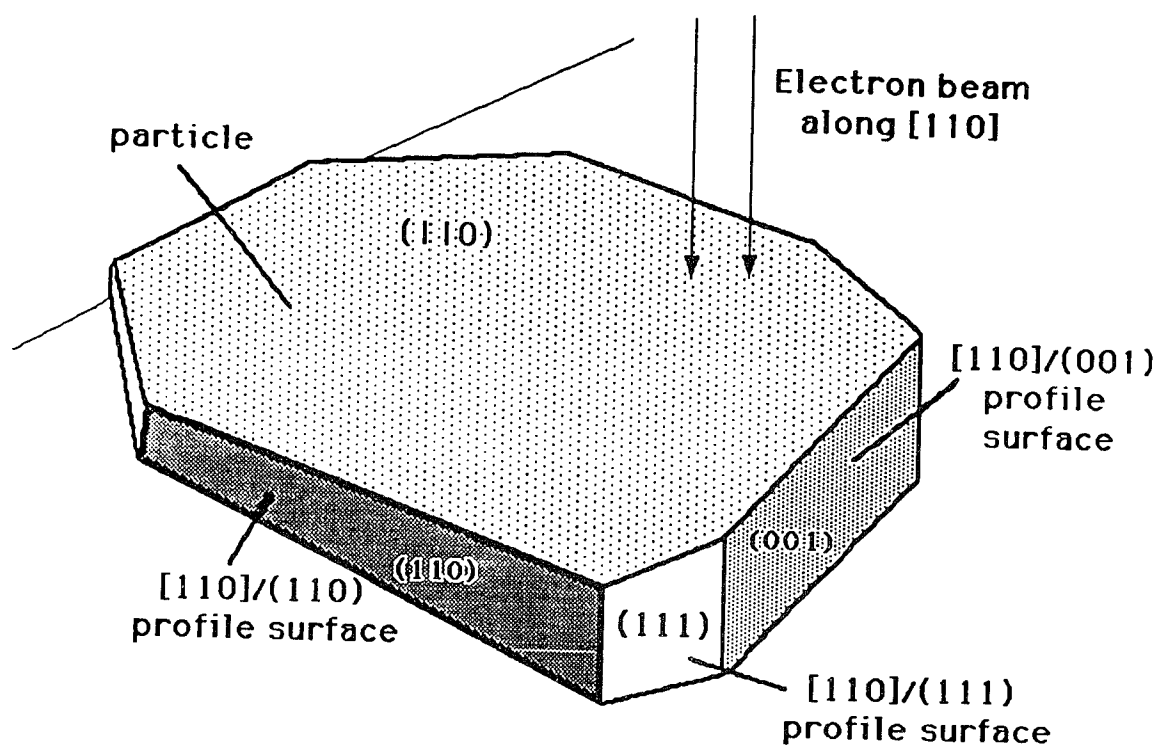
Figure 2.2 Schematic illustration of the principle of the profile imaging (Courtesy of Dr. M. I. Buckett).

relaxation on Au(100) surface has been detected by this technique (Marks 1984). Profile imaging of a thin edge of Au(110) by Marks (1983) clearly showed the 2×1 reconstruction in the [110] direction which is well known from LEED work. Using this technique, Sinclair (1981) observed atomic motion on the surface of semiconductors.

§2.4 AUGER ELECTRON SPECTROSCOPY

Auger electrons were first detected in 1925 by Pierre Auger (Auger 1925) who observed their tracks in a Wilson Cloud Chamber and correctly explained their origin. Auger electrons are produced by the process depicted in Figure 2.3 using a KLM energy diagram. In figure 2.3, the core K-shell is ionized by a primary electron leaving behind a hole. An electron in the L-shell can drop to fill the K-hole. The energy released (E_K - E_L) in this transition is either emitted as a photon or given to a third electron in the M-shell. If the energy is sufficient, this electron can be ejected from the surface with an energy of (E_K - E_L - E_M). This process is called a KLM Auger transition. The energy of the emitted Auger electron only depends on the energy levels involved in the transition, thus is characteristic of the parent atom. Therefore, elemental identification can be obtained by measuring the Auger electron energies. If Auger electrons with kinetic energies below 1500 eV, which have mean free paths of 3 - 15 Å and are emitted from the top three atomic surface layers, are detected, surface sensitive chemical analysis can be achieved.

An AES consists of three parts: a source for primary excitation, an analyzer and a detector system. The most commonly used excitation source has been an electron beam.
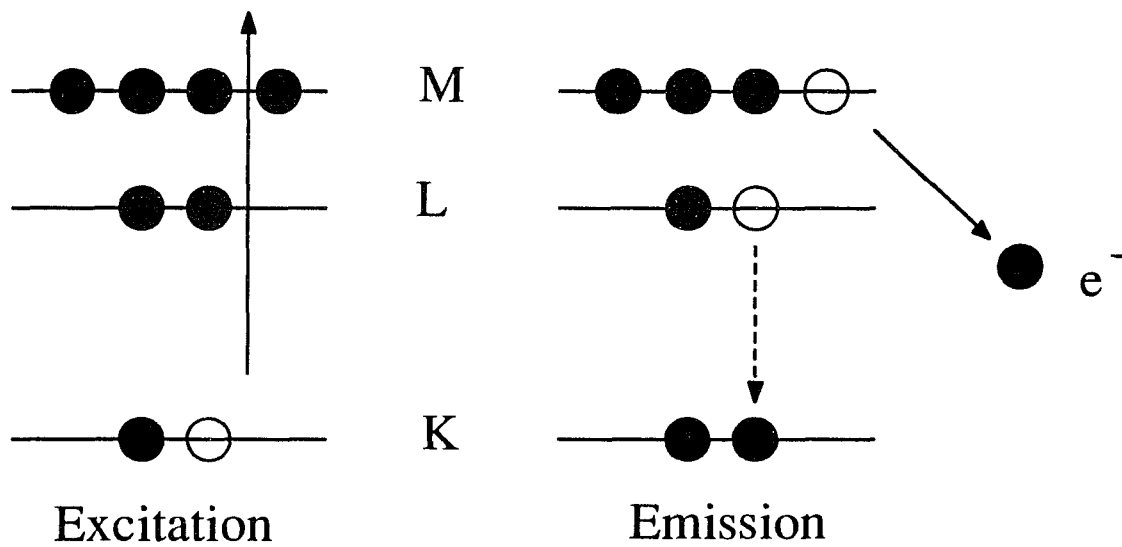
Figure 2.3 A schematic representation of the Auger electron mission process for a typical KLM energy level.

Electron energy analyzers can be made based upon electrostatic or magnetic principles. There are two types of electrostatic analyzers: the dispersive and the retarding field. Of the dispersive type, the cylindrical mirror analyzer (CMA, Palbmerg 1969) and the concentric hemispherical analyzers (CHA, Harris 1968 and Taylor 1969) have been successfully used. Of the retarding field type, the LEED/Auger device, which uses the LEED electron optics as the energy analyzer, has become very popular. The purpose of the detection stage is to enhanced the sensitivity of the spectrometer. The technique of pulse counting (detection of individual electrons) with repetitive energy sweeps is now widely used. Its advantages lies in the fact that high resolution and good signal-to-noise ratios are achievable at low count rates.

§2.5 X-RAY PHOTOELECTRON SPECTROSCOPY

The principle of XPS is depicted schematically in figure 2.4. which shows the typical energy level diagram of a solid. Below the Fermi level, core electrons are bound with various binding energy E_b. Near the Fermi level electrons form a band with a certain occupation density. By irradiating the solid with x-rays, electrons near the Fermi level or in the atomic core can be ejected with a kinetic energy E_{kin} given by

$$E_{kin} = h\nu - E_b - \phi$$

where ϕ is the work function defined as the energy necessary to transfer an electron from Fermi level to the vacuum level and $h\nu$ is the x-ray energy. XPS is very usefully in measuring small chemical shifts of atomic core levels.
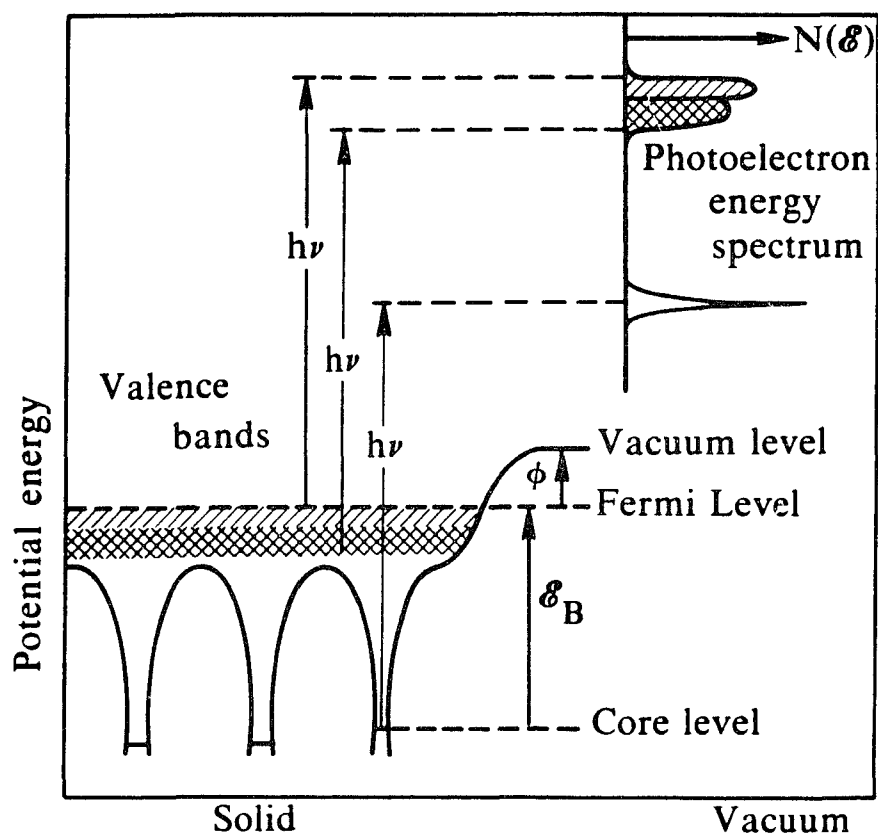
Figure 2.4 A schematic energy level diagram showing photoemission from the valence bands and a core level in a solid (Burns 1985).

CHAPTER 3   DEVELOPMENT OF AN *IN-SITU* MICROSCOPE- COMPATIBLE AUGER ELECTRON SPECTROMETER

§3.1   INTRODUCTION

Surface studies using an electron microscope require one to be able to determine surface structure and chemical composition at the same time. Surface structures alone do not provide complete information about the surface. Even though in principle high resolution structural images contain information on the number of atoms in an atomic column, in practice the process of obtaining this information is difficult and may be impossible. One approach to this problem is to develop an *in-situ* electron microscope compatible AES. In recent years, AES has been developed into one of the most sensitive methods of surface analysis. It is capable of uniquely identifying each element and is essentially a surface probe as Auger electrons come from the top five layers.

In this chapter, the detailed development of an AES for the Hitachi UHV H-9000 electron microscope will be presented. The AES takes advantage of the compact size of the analyzer (Comstock model AC-900) and the focusing action of the magnetic field of the objective pole piece. Section 3.2 is devoted to the detailed description of each part of the spectrometer. Calculations of the trajectories of Auger electrons in the magnetic field of the objective pole piece are presented in section 3.3. Section 3.4 describes developments of other microscope-compatible AES. The experimental characterization of the AES is discussed in section 3.5. Primary results, problems and future implementations are described in section 3.6.

29

§3.2 INSTRUMENTATION

§3.2.1 Experimental Arrangement

Figure 3.1 shows the schematic arrangement of the AES in the objective region of the Hitachi UHV-H9000 electron microscope. The AES consists of an Einzel focusing lens, an energy analyzer and a channelplate charged particle detector, which is housed in an oxygen-free copper box for electrical shielding. The size of the copper box is 4.3 × 5.7 × 7.0 cm^3. The whole assembly fits just above the objective pole piece, and has a hole drilled through it to allow the primary electron beam (100 - 300 keV) to reach the specimen.

Figure 3.2 shows the supporting electronics in the sector sweeping field mode. Auger electrons emitted from the specimen travel in the magnetic field of the pole piece in a spiral trajectory. In the magnetic field of the pole piece, Auger electrons are focused along the optical axis as will be shown in Section 3.3. A three-element electrostatic lens (Comstock EL-301 Einzel lens) focuses the Auger electrons into the entrance aperture. Energy selection is achieved using a concentric hemispherical analyzer (CHA). At the exit of the analyzer, an aperture at ground potential prevents the field penetration. The electron detector is a channelplate electron detector (Comstock CP-602), preferred for its small size and high gain. The pulses are led to a high voltage vacuum feedthrough by a short shielded cable with low capacitance. They are then injected to a preamplifier, where the signal is amplified, discriminated and shaped. The data can be collected by two methods: analog and pulse counting. In the pulse counting mode, data is accumulated in an Apollo DN-3500 workstation operating as a multichannel analyzer.

Microscope Objective Region
Cross-sectional View From Front

Halogen Lamps

μ-metal shield

electron energy
analyzer

Einzel lens

electron detector

Optical Probe

Cartridge
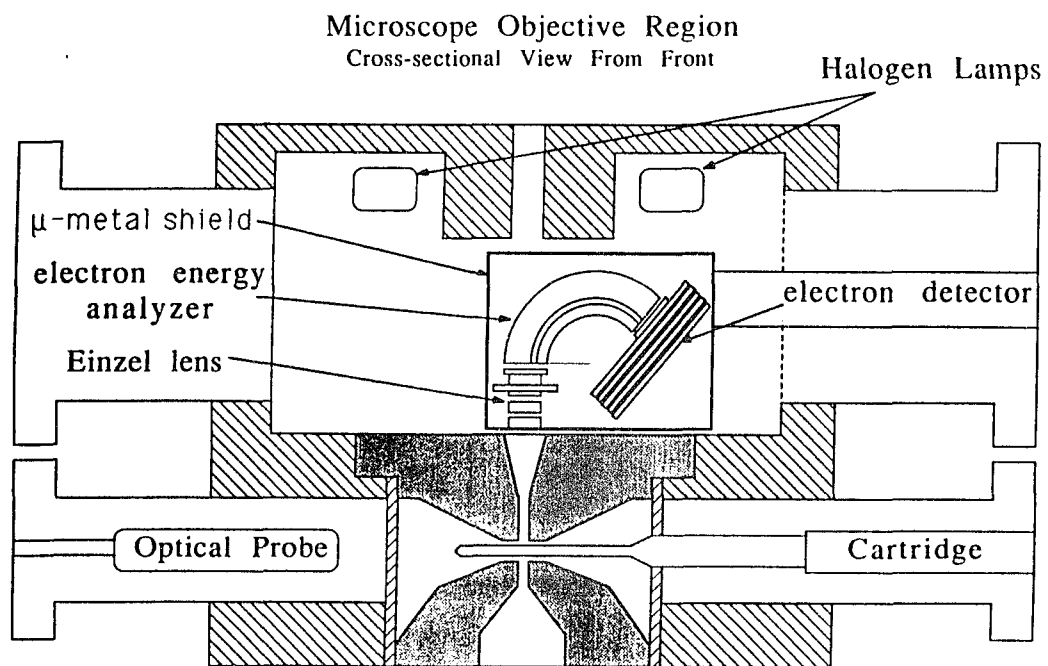
Figure 3.1   Schematic of the AES in the objective region of a UHV H-9000 electron
microscope (Courtesy of J. E. Bonevich).

ENTRANCE APERTURE ⟶

160° ANALYZER

500 k

500 k

EXIT APERTURE ⟶

CHANNEL PLATE
ELECTRON MULTIPLIER ⟶

15 Meg

10 Meg

+HV ⟵

100 K

100 pF

INPUT

ac REFERENCE ⟶

LOCK IN
AMPLIFIER

OUTPUT

RAMP VOLTAGE ⟶ X

X - Y
RECORDER

Y
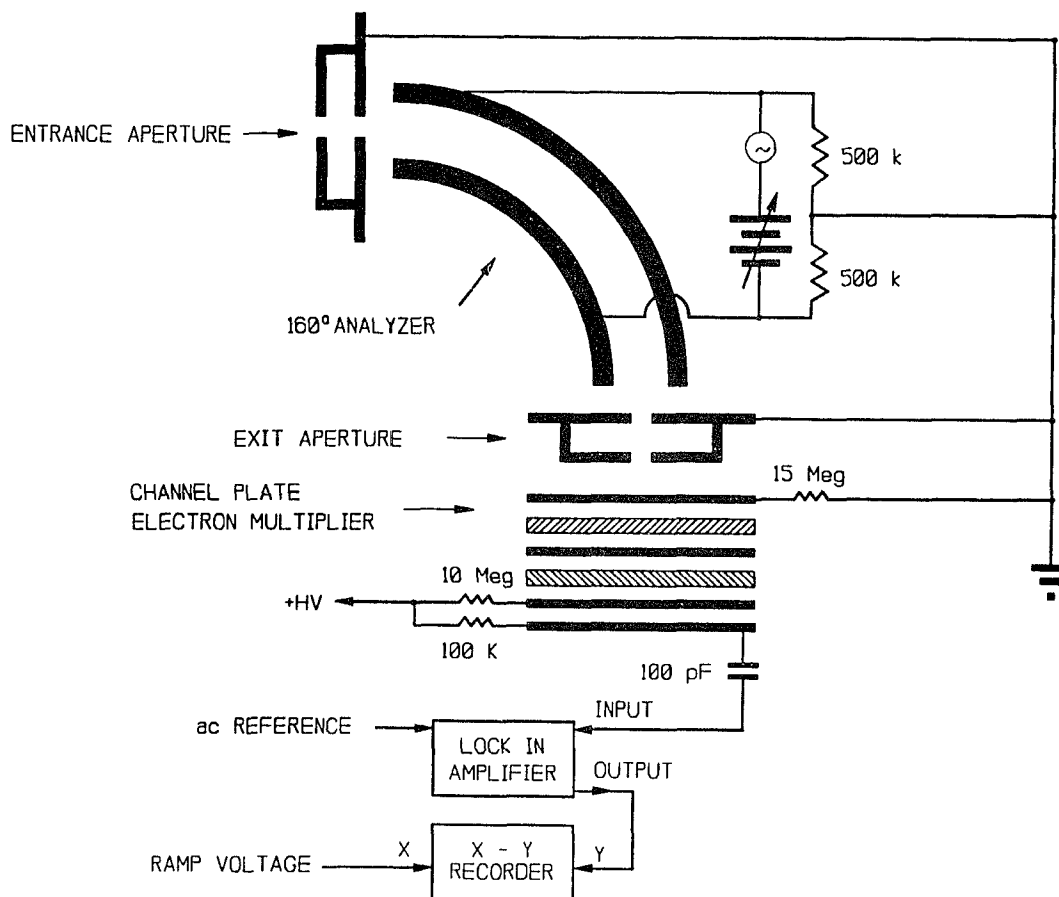
Figure 3.2   Schematic of the AES with the supporting electronics in the sector sweeping field mode.

The channel address is synchronized to the sweep voltage of the spectrometer. Whenever a pulse comes in at a certain energy, the computer will be triggered to increase the counts at the corresponding channel by 1. This data acquisition method is called gate pulse counting. Differentiation of the data is performed numerically.

In the analog mode, a preamplifier converts the current signal from the channelplate into a voltage signal. The spectrum is then recorded by a X-Y recorder. Differentiation of the data can be performed using a lock-in amplifier.

§3.2.2 Einzel Focusing Lens

The Comstock Einzel lens (Model EL-301) is a three element unipotential electrostatic lens system. The lens consists of three cylinders at potentials V_1, V_2 and V_3 (= V_1). Such a lens produces a focusing without changing the overall energy of the transmitted particles. Figure 3.3 depicts the focusing properties of the EL-301 for various values of V_1, V_2 and V_3 (= V_1).

§3.2.3 160° Concentric Hemispherical Analyzer

The electron energy analyzer consists of two concentric 160° spherical sector surfaces which are made of oxygen free copper. The focusing and energy dispersion properties of this type of energy analyzer were first investigated by Purcell (1938). When a voltage potential ΔV is applied between the inner sector and the outer sector, Auger electrons of energy E are transmitted if the potential difference ΔV between the inner and outer sector satisfies
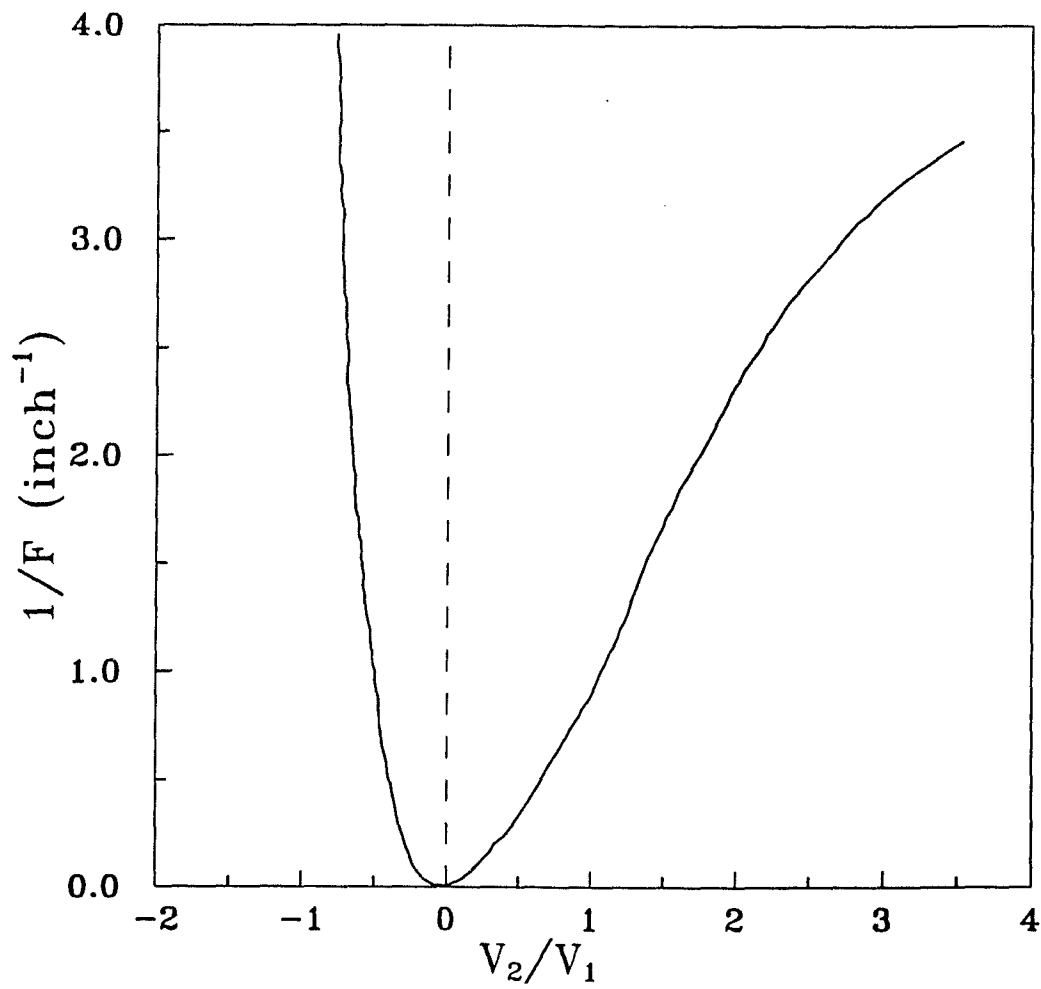
Figure 3.3   Focusing properties of the Einzel focusing lens at various V_1, V_2 and V_3 (= V_1).

$$E = \frac{\Delta V}{(\frac{r_1}{r_2} - \frac{r_2}{r_1})} \qquad (3.1)$$

where r_1 is the radius of the outer concave sector and r_2 is the radius of the inner convex sector. For the Comstock AC-900 energy analyzer, $r_1 = 2.02$ cm and $r_2 = 1.63$ cm, therefore equation (3.1) becomes

$$E = 2.3 \, \Delta V \qquad (3.2)$$

The relative energy resolution of the analyzer is given by

$$\frac{\Delta E}{E} = \frac{\omega}{R \, (1-\cos\phi) + l \, \sin\phi} \qquad (3.3)$$

where $\phi = 160°$, is the angle subtended by the analyzer sector, $l = 0.383$ cm, is the distance from the exit of the sector field to the final exit aperture, $R = 0.7185$ cm, is the mean sphere radius and ω is the entrance aperture size. For example, when $\omega = 2$ mm, the relative energy resolution is about 7.0 %.

To obtain an energy spectrum, the analyzer can be operated in two modes: the constant transmission mode (Figure 3.4a) and the sector sweeping field mode (Figure 3.4b). In the constant transmission mode, the electron pass energy is set at a predetermined value. A ramp voltage is applied to the entrance aperture to accelerate or decelerate the energy of the input electrons to the pass energy. Sweeping the ramp voltage on the entrance aperture will allow the spectrum to be analyzed. The characteristic of this mode is ΔE = constant. This method provides a simplest means for

(a)

(b)
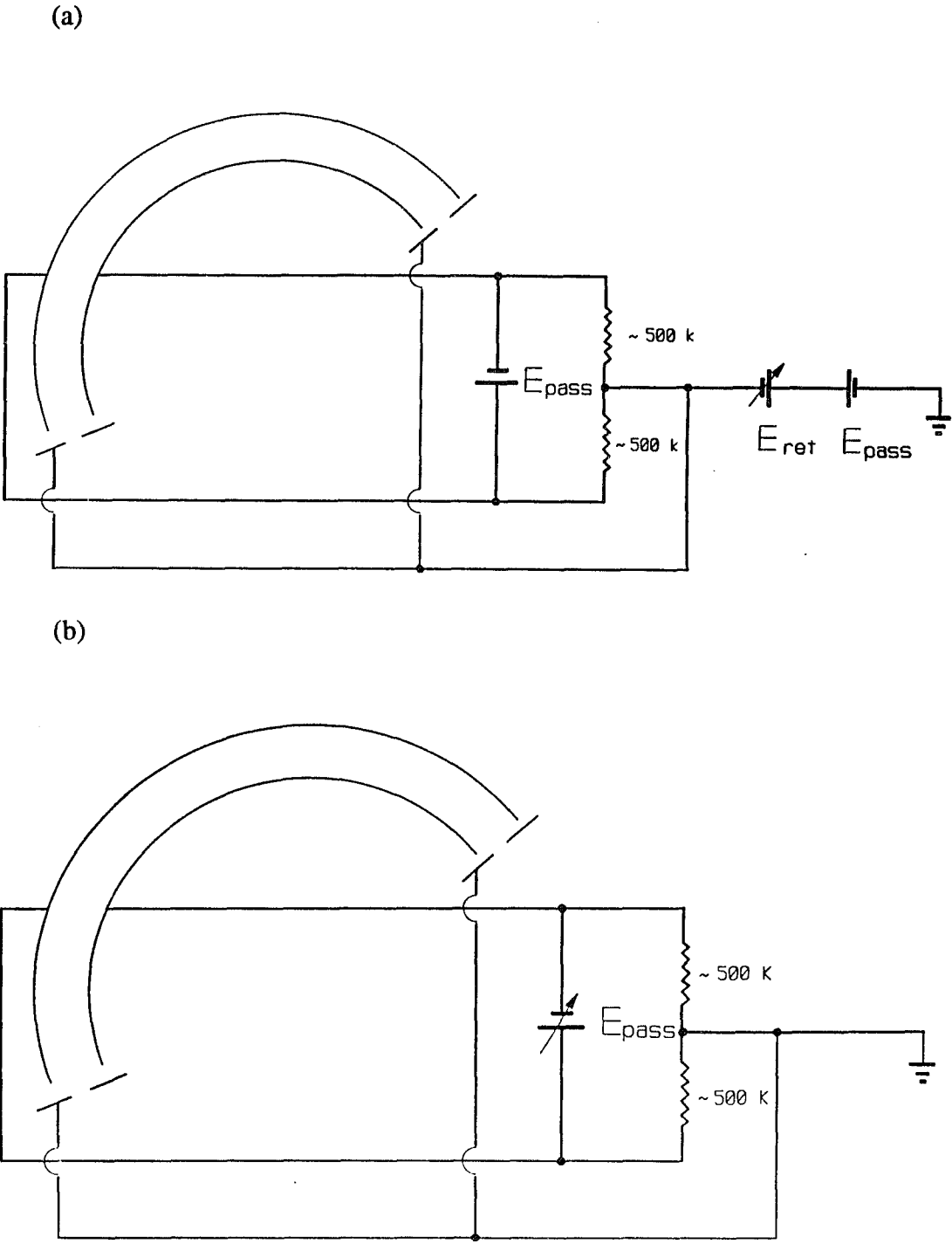
Figure 3.4 a) Electrical connection of the constant transmission mode.
b) Electrical connection of the sector sweeping field mode.

improving the resolution at higher energy.

In the sector sweeping field mode, equal and opposite ramp voltages are applied to the sector surfaces so that a changing ΔV causes the input spectrum to be analyzed. In this mode, $\dfrac{\Delta E}{E} = constant.$

§3.2.4 Dual Channelplate Charge Particle Detector

The electron detector is a channelplate charged particle detector (Comstock model CP-602). A schematic of the detector and its electrical connections are shown in Figure 3.5. The detector consists of two microchannel plates for serial gain. The unit features an off-center entrance aperture so that eventual loss of gain may be compensated by exposure of fresh plate surface through a simple rotation.

A microchannel plate (MCP) is a thin disk of lead glass possessing a great multitude of closely packed parallel tunnels or channels which connect the two planar surfaces. The lead glass is specially processed to have an exceptionally high secondary electron yield. With a voltage applied across the disk faces in a vacuum, each channel becomes a continuous dynode electron multiplier. Electrons impinging on the input face release electrons which are then accelerated along the channels, promoting further collisions with the channel walls, dislodging additional secondary electrons, and thus yielding an electron multiplication. The gain of a MCP is defined as the ratio of the output to input charge or output to input current. The CP-602 has a gain of 10^6 with an operation voltage of

100 pF
100 K
10 Meg
15 Meg

COLLECTOR
SIGNAL
GND/+HV
-HV/GND
ENTRANCE
+ions/electrons
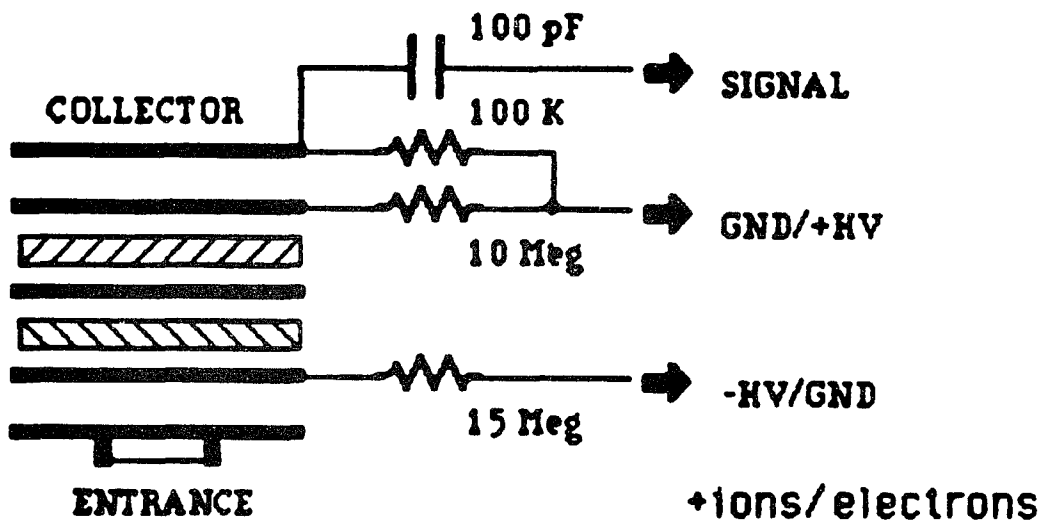
Figure 3.5   Schematic and typical electrical connection of the Comstock CP-602 channelplate charged particle detector (Courtesy of Comstock Inc.)

approximately 2000 V. Noise associated with the CP-602 increases with voltage. Nevertheless, the measured anode dark current is remarkably low and generally negligible when the multiplier devices are operated at less than 1000 V per MCP.

§3.3 THE TRAJECTORY OF AUGER ELECTRONS IN THE MAGNETIC FIELD OF THE POLE PIECE

Figure 3.6 shows the magnitude of the magnetic field along the optical axis in the region of the pole piece. The field is cylindrically symmetric with the optical axis and decays to zero inside the gap of the pole piece at a distance of about 1.0 cm away from the sample. The distance between the sample position and the top of the pole piece is about 3.0 cm (See Figure 3.1). This section presents the detailed calculation of electron trajectories in the magnetic field of the pole piece.

§3.3.1 Principle of the Magnetic Parallelizer

Recently, Kruit and Venables (1988) have demonstrated that high-spatial-resolution AES can be achieved using the parallelizing action of the magnetic field of the objective pole piece in an electron microscope. The principle of the magnetic parallelizer will be described below.

Assuming that an Auger electron is emitted from an sample at an angle θ with respect to the magnetic field direction (z-direction), it will undergo a helical motion. The radius of the helical motion is given by
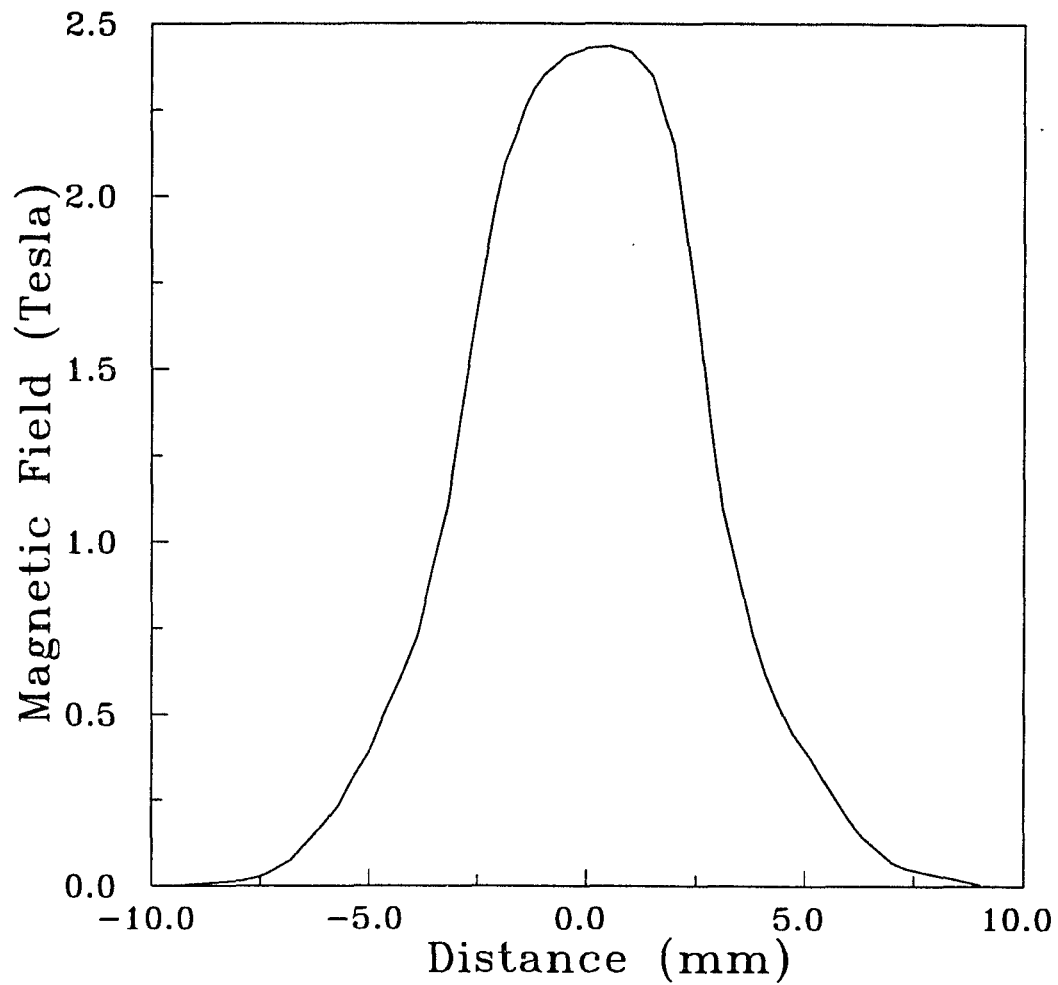
Figure 3.6   Axial magnetic filed of the pole piece of the Hitachi UHV H-9000
electron microscope as a function of the distance from the sample position
(Courtesy of Hitachi Corp.).

$$r = (\frac{2m}{e})^{1/2} \frac{E^{1/2}}{B} \sin\theta \qquad (3.4)$$

where e = electron charge

   m = electron mass

   E = electron energy

   B = magnetic field

The angular momentum with respect to the center of the spiral, L then can be written as

$$L = \frac{m^2 \, v^2 \, \sin^2\theta}{e \, B}, \qquad (3.5)$$

where $v = \sqrt{(\frac{2 \, E}{m})}$.

If the magnetic field is "adiabatic", i.e., the magnetic field experienced by the electron changes negligibly in the course of one revolution of the helical motion, the angular momentum is a conserved quantity (Farago 1970, Chen 1974 and Jackson 1975). Consequently, after the Auger electron emitted with an initial angle θ_i has traveled some distance along the magnetic field the final angle θ_f is given by

$$\frac{\sin\theta_f}{\sin\theta_i} = (\frac{B_f}{B_i})^{1/2} \qquad (3.6)$$

At the same time, the radius is determined by

$$\frac{r_f}{r_i} = (\frac{B_i}{B_f})^{1/2} \qquad (3.7)$$

where B_i = initial magnetic field

B_f = final magnetic field

r_i = initial radius

r_f = final radius

As the Auger electron moves to the lower field region, θ_f becomes smaller and r_f becomes larger. For example, the magnetic field of the pole piece of the UHV H-9000 electron microscope at the sample position is 2.43 T. At a distance of 7.9 mm away from the sample position, the magnetic field drops down to 1.59×10^{-2} T. Then $\dfrac{\sin\theta_f}{\sin\theta_i} = 0.28$, and $\theta_f = 14.08°$ for $\theta_i = 60°$, or $\theta_f = 16.32°$ for $\theta_i = 89°$. Thus many of the Auger electrons emitted from the sample are parallelized to within 16° of the axis by the magnetic field of the pole piece. If electrons can be extracted from the magnetic field without the loss of the parallelism, almost all the emitted electrons can be collected and analyzed.

If B_f decreases to zero, as in the case of the UHV H-9000, the above formulas imply that the electron will travel parallel with the z axis and the radius r will be infinity. This is obviously not the case. The reason is because the "adiabatic" approximation can not be satisfied in the nearly field free region. In fact, our trajectory calculations described in the next section show that in the nearly field free region where the "adiabatic" approximation breaks down, the electron will travel in a straight line with a smaller angle with respect to the z-axis due to the parallelizing effect.

§3.3.2 Ray Tracing

In an magnetic field, the equation of motion of an electron is

$$\vec{F} = m\vec{a} = -e\vec{v} \times \vec{B}$$

(3.8)

where $\vec{B}$ = magnetic field

$\vec{F}$ = magnetic force on the electron

$\vec{a}$ = acceleration

In the axially symmetric field ($B_\varphi = 0$) of an electron microscope, it is most convenient to use a cylindrical co-ordinate system (r, z, φ). In this case, equation (3.8) can be separated to the forms of

$$\frac{\partial}{\partial t}(mr^2\frac{\partial\varphi}{\partial t}) = rF_\varphi$$

(3.9a)

$$m\frac{\partial^2 z}{\partial t^2} = F_z$$

(3.9b)

$$m\frac{\partial^2 r}{\partial^2 t} = F_r + mr(\frac{\partial\varphi}{\partial t})^2$$

(3.9c)

Upon substituting the Lorentz force (equation 3.8) into equation (3.9) with $B_\varphi = 0$, Equation (3.9) can be transformed into

$$m\frac{\partial^2 r}{\partial t^2} = -eB_z r\frac{\partial \varphi}{\partial t} + mr(\frac{\partial \varphi}{\partial t})^2 \qquad (3.10a)$$

$$mr^2\frac{\partial \varphi}{\partial t} = \frac{e}{2}r^2 B_z + C \qquad (3.10b)$$

$$m\frac{\partial^2 z}{\partial t^2} = eB_r r\frac{\partial \varphi}{\partial t} \qquad (3.10c)$$

where B_z is the radial component of the magnetic field, B_r = longitudinal component of the magnetic field, and C is a constant given by

$$C = m\; r_0^2\; \frac{\partial \varphi}{\partial t}\big|_0 - \frac{e}{2}\; r_0^2\; B_{z,o}$$

where r_0, $B_{z,0}$ and $\frac{\partial \varphi}{\partial t}\big|_0$ are the initial values.

For meridional rays, i.e. rays with path initially in an axial plane $\frac{\partial \varphi}{\partial t}\big|_0 = 0$, C = 0 and for paraxial rays, i.e. rays with small value of r, equation (3.10c) can be approximated by

$$\frac{\partial^2 z}{\partial t^2} \approx 0 \qquad (3.11)$$

Equation (3.11) implies that v_z is a constant. Substitution of equation (3.10b) in equation (3.10a) results in

$$m\frac{\partial^2 r}{\partial t^2} = -\frac{e^2}{4m}B_z^2 r \qquad (3.12)$$

The time can be eliminated by writing

$$v_z = \frac{\partial z}{\partial t} \approx v \qquad (3.13)$$

Then equation (3.12) becomes

$$\frac{\partial^2 r}{\partial z^2} = -\frac{e}{8m_o V} r B_z^2(r) \qquad (3.14)$$

where V is the accelerating voltage. This equation is called paraxial equation. Once the field is known, integration of equation (3.14) results in the trajectory of an electron entering the field.

From an examination of equation (3.14), it can be seen that the paraxial equation does not involve the first-order derivatives of z or r. A numerical integration method the devised by Milne (1933) takes advantage of this fact. This method can be used to solve the paraxial equation and the accuracy of the solution has been tested experimentally by Goddard and Klemperer (1944).

Given an initial condition of r = r_o, the numerical calculation proceeds as illustrated in a tabular form as below:

Section	t	r_s''	r'	r
A	t_0 . . . t_s	r_0'' . . . r_s''	r_0' . . . r_s'	r_0 . . . r_s
B	t_{s+1} . . . t_n . . .	r_{s+1}'' . . . r_n'' . . .	r_{s+1}' . . . r_n' . . .	r_{s+1} . . . r_n . . .

Note $\quad r'' = \dfrac{\partial^2 r}{\partial t^2}$, $r' = \dfrac{\partial r}{\partial t}$

Section A provides a set of initial values for section B. Section B is obtained by using the formulae derived by Milne (1933). The formulae are

$$r_{n+1} \approx r_n + r_{n-2} - r_{n-3} + \frac{\omega^2}{4}(5\frac{\partial^2 r_n}{\partial z^2} + 2\frac{\partial^2 r_{n-1}}{\partial z^2} + 5\frac{\partial^2 r_{n-2}}{\partial z^2}) \qquad (3.15)$$

for n = 3 to n = 7. From n = 8 onwards, the formula for integration corresponding to equation (3.15) is

$$r_{n+1} \approx r_n + r_{n-4} - r_{n-5} + \frac{\omega^2}{48}(67\frac{\partial^2 r_n}{\partial z^2} - 8\frac{\partial^2 r_{n-1}}{\partial z^2} + 122\frac{\partial^2 r_{n-2}}{\partial z^2} -$$
$$8\frac{\partial^2 r_{n-3}}{\partial z^2} + 67\frac{\partial^2 r_{n-4}}{\partial z^2}) \qquad (3.16)$$

The trajectories of Auger electrons in the magnetic filed of the pole piece of the Hitachi UHV H-9000 electron microscope were calculated using the integration method described above. Initial values in section A were obtained by assuming that the magnetic

field is locally uniform near the sample position. This can be made as accurate as desired by choosing a sufficiently small z interval. Figure 3.7 shows the trajectory of a 500 eV Auger electron with (a) 10° and (b) 50° emission angles with respect to the optical axis in the pre-specimen magnetic field of the pole piece. In the strong field region, the electron spirals up the optical axis with increasing radius. This is in good agreement with the calculation of the magnetic parallelizing effect. In the nearly field free region where the "adiabatic" approximation breaks down, the electron travels in a straight line with a smaller angle with respect to the optical axis due to the parallelizing effect.

§3.4 AUGER ELECTRON SPECTROMETERS IN COMBINATION WITH STEM

Electron microscope compatible Auger electron spectrometers were first developed for STEM. For comparison, two developments, one at Delft University of Technology (DELFT) and the other at Arizona State University (ASU) will be described. The common method used in both designs is that Auger electrons emitted from the sample are first parallelized by magnetic parallelizers, deflected by electrostatic deflectors to outside of the microscope and then collected by electrostatic energy analyzers.

§3.4.1 The Development at DELFT

At DELFT, an Philip EM 400 was modified in order to accommodate an AES utilizing the parallelizing principle described in Section 3.3.1 (Bleeker 1990a, 1990b). Figure 3.8 shows the schematic of the DELFT design. The sample is situated in the high magnetic field between the pole pieces of the objective lens. Extra coils (PA) were added
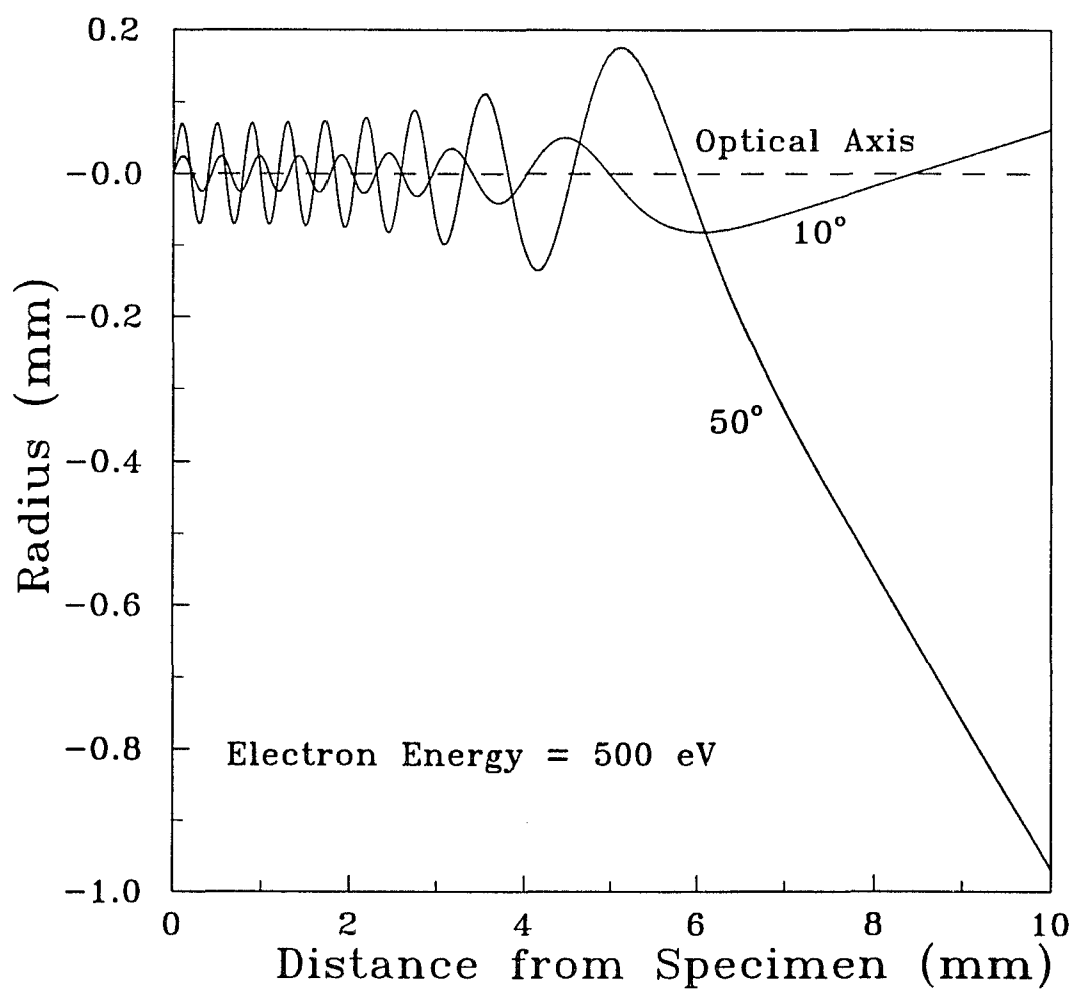
Figure 3.7   Trajectories of a 500 eV Auger electron in the pre-specimen magnetic
field of the magnetic pole piece with emission angles with respect to the
optical axis: a) 10° and b) 50°.

EL

HO

MA

PA

VA

CHA
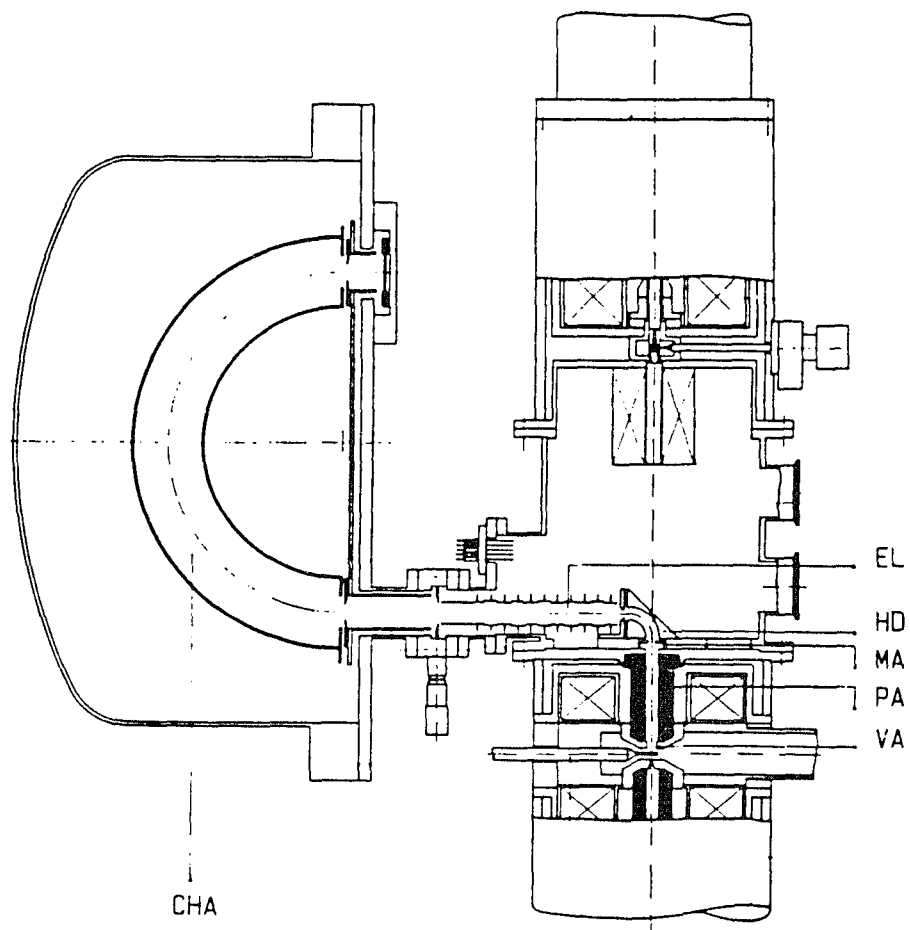
Figure 3.8   Experimental set-up of the AES developed at DELFT (Bleeker 1990a).

to provide the magnetic field for the parallelizer in the field free region. The space between the condenser lenses and the objective lens is enlarged for a vacuum chamber. A 90° hemispherical deflector (HD) and electrostatic lenses (EL) are used to deflect the parallelized electron beam and focus it into the CHA attached to the outside of the microscope. The CHA has a central radius of 140 mm and is built in a commercial μ-metal vessel. Initial experimental results from this system have shown the capability of obtaining a good spectrum of the secondary electrons in the energy range of 0 - 100 eV. Auger spectra of dirty specimens show carbon and some other features that can not be identified. The vacuum in this microscope is on the order of 1×10^{-7} torr, which is not clean enough for serious Auger spectroscopy. In the present, it is used as a demonstrator of the principle.

§3.4.2   The Development at ASU

At ASU, a field emission STEM has been designed to incorporate the magnetic parallelizer principle for AES (Kruit 1988). Figure 3.9 shows the schematic of the experimental set-up. The electron beam travels through the analysis chambers (AC1 and AC2) before and after the sample, which is mounted on the side entry cartridge. The upper and lower pole pieces of the objective lens contain parallelizers PU and PL. PL is incorporated in the objective stigmator, and PU in the post specimen lens alignment and descan coils. The parallelizer field can be energized to $B_f \approx 10^{-2}$ T. Electrons at the exit (W) of the parallelizer (PU) are then deflected and focused into a commercially available CHA (E) by a small gridless CMA (C), which served as an electrostatic electron
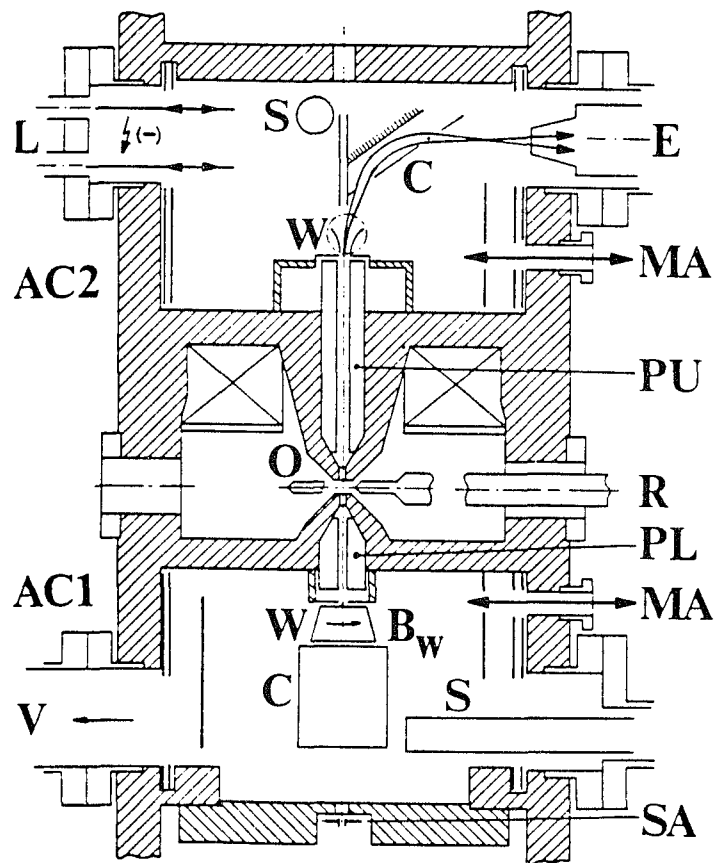
Figure 3.9 Arrangements of the AES developed at ASU (Kruit 1988).

deflector. Recently Auger spectra with 3.0 nm spatial resolution acquired with this AES

have been reported (Hembree 1991).

§3.5 CHARACTERIZATIONS

§3.5.1 Collection Efficiency

By extrapolating the straight line of the calculated trajectories as shown in Figure 3.7

to a distance of 3 cm from the specimen and imposing an aperture, the maximum

emission angle θ_m within which Auger electrons will be collected can be determined, and

the effective collection solid angle and collection efficiency can be obtained. For

example, as shown in Table 3.1 for 500 eV Auger electrons and a 2 mm entrance

aperture, θ_m is 14.2°, the collection solid angle is 0.2 steradian, and the collection

efficiency is 3.2% in the magnetic field. Without the field, the θ_m is 1.9°, the collection

solid angle is 3.5 x10^{-3} steradian and the collection efficiency is 0.03%. Therefore the

collection efficiency is increased by a factor of at least 100 times as a results of the

focusing action of the magnetic field of the pole piece. The final focus length as a

function of energy is shown in Figure 3.10. It is also noted that, the effective collection

efficiency is a function of energy. This introduces an aberration in the spectrum.
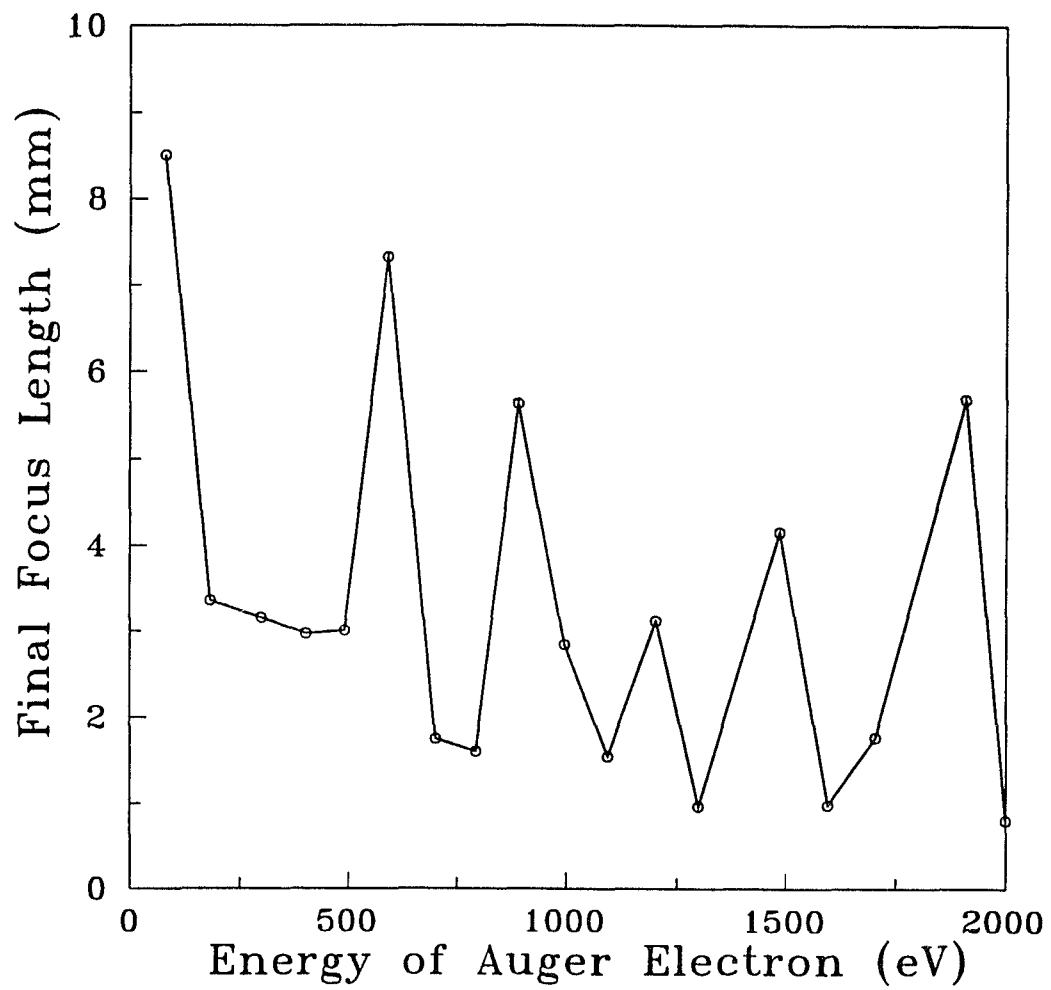
Figure 3.10 The final focus length as a function of energy.

TABLE 3.1   Comparison of the Collection Efficiency of the AES with
and without the Magnetic Field of the Pole Piece.

	With the Field	Without the Field
Θ_m	14.2°	1.9°
Solid Angle (Steradian)	0.2	3.5×10^{-3}
Collection Efficiency	3.2%	0.03%

§3.5.2   Energy Resolution

The energy resolution of a spectrometer is defined as the ratio $\Delta E/E_p$, where ΔE is

the full width half maximum (FWHM) of the energy distribution, and E_p the energy at

which the analyzer is tuned.   The experimental characterization of the resolution of our

Auger electron spectrometer was carried out using elastically diffracted electrons from a

silver foil.   The experiment was performed in a test chamber with a vacuum of 2×10^{-8}

torr.   The AES was operated in the analog mode.   Spectra of the first order derivative

were collected with an AC modulation of 2 V.   Figure 3.11 shows the variation of ΔE as

a function of incident electron beam energy.   A least square fit was applied to this curve.

The resulting equation was $\Delta E = 0.055\ E_p + 4.6$ eV.   The resolution can be determined

from the linear term to be 5.5%, which is in good agreement with the predicted value of

7.0%.   The constant term of 4.6 eV is due to the energy spread in the elastic peak

introduced by the AC modulation.   In general the energy spread is $\Delta E = 2\ V_{AC}$

(Szalkowski 1977).   For the experimental condition used, $\Delta E = 4.0$, which indicates that

the experimental values of 4.6 eV is in good agreement with the theoretical one.
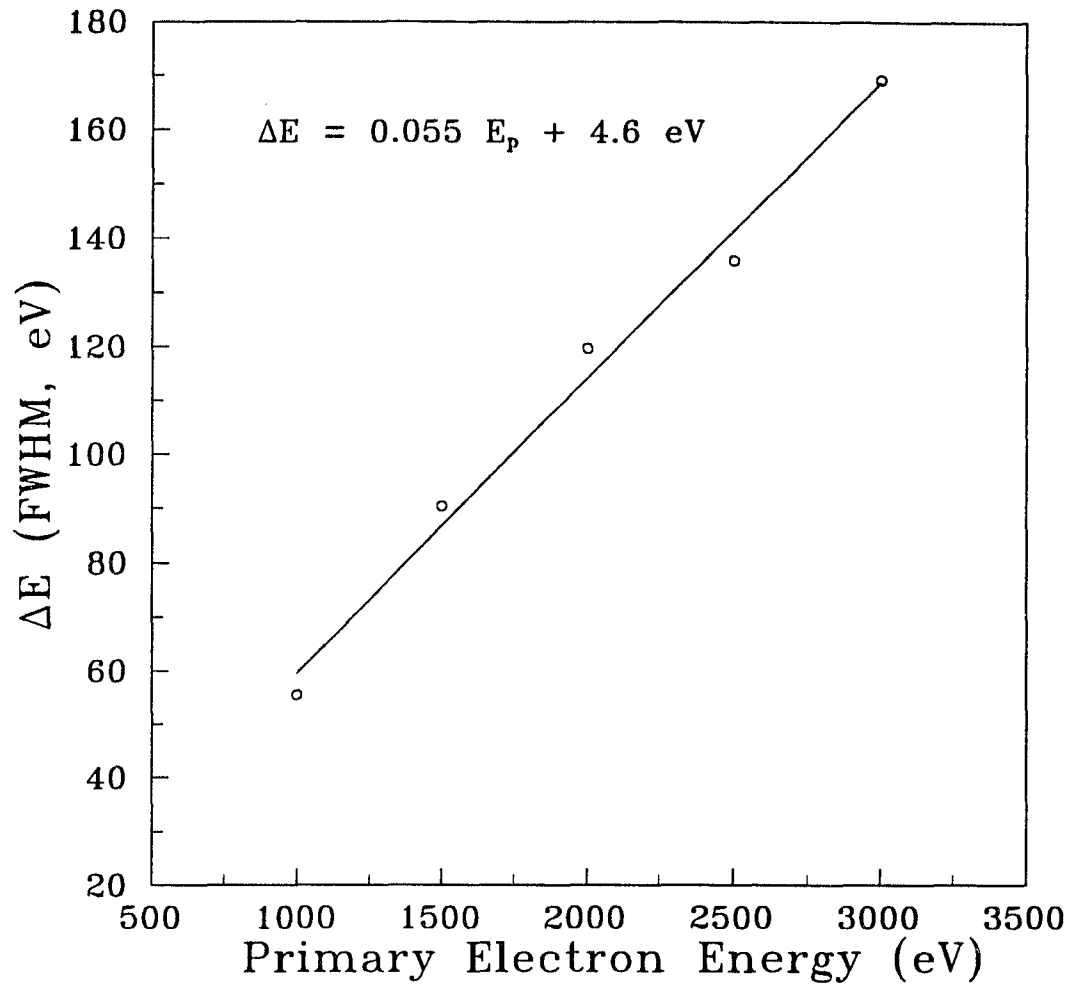
Figure 3.11 The full width half maximum of the elastic peak as a function of primary beam energy.

§3.5.3 Signal-to-Noise Ratio

In collecting Auger electron spectra, one important factor to consider is the time it takes to obtain a certain signal/noise in a spectrum. In our microscope compatible AES, several special considerations need to be addressed.

The first consideration is the high primary electron beam energy (100 - 300 keV) and the low emission current ($<$ 100 nA) used in an electron microscope. The interaction cross-section is inversely proportional to the primary beam energy and the Auger signal yield is directly proportional to the primary beam current, resulting in a small Auger signal. To overcome this difficulty, pulse counting electronics were therefore implemented to provide adequate sensitivity. A long acquisition time was used to obtain Auger spectrum with reasonable signal-to-noise ratio.

The second consideration is the noise generated by x-rays. The background can be generated from two effects. The first is the background produced by x-rays that have a direct line of sight to the microchannel plate. The microchannel plate is equally sensitive to x-rays as to electrons. The second is the background generated by x-ray photoelectrons that are scattered into the microchannel plate. In an electron microscope, x-rays can be generated by two distinctly different processes. The first process is the deceleration of electron beam in the columbic field of the atom core. X-rays generated by this process have a continuous spectrum. The second process is the excitation of inner shell electrons. The excitation process creates a hole in the inner shell. The transition of an electron from the outer shell to fill the vacancy in the inner shell involves an energy change. The energy released can manifest itself either in the form of x-rays or an Auger electron. X-

rays generated by this process have a characteristic energy which is related to the energy difference between the two energy levels involved. The x-ray intensity at a given continuum energy increases as the electron beam energy increases (Goldstein 1984). The effect of x-rays can be demonstrated by the effect of the condenser aperture on the Auger spectrum. Inserting the condenser aperture increased the number of electron counts, but greatly decreased the signal/noise. In an electron microscope, a condenser aperture is used to block the electrons with large convergent angles to increase the convergence of the primary electron beam. The blocked electrons can generate x-rays in the condenser aperture, which has a direct line of sight to the channelplate electron detector. The decrease in the signal/noise can be thus attributed to increase in the background created by the x-rays. One solution for this problem would be to use a thick condenser aperture so that x-rays generated at the top of the aperture will be adsorbed. The ultimate solution would be to construct a shield box with a heavy metal of an appropriate thickness for x-ray shielding. This method has been applied successfully by Shinn (1992).

The third consideration is the secondary electron background. Secondary electrons are produced as a result of energy transfer from primary electrons to conduction electrons in the solid. The energy distribution of secondary electrons shows a peak at about 3-5 eV, and drops off sharply as the energy increases. In thin specimens, the background in an Auger spectra is mostly secondary electrons.

In thick specimens, backscattered electrons and secondary electrons produced by backscattered electrons while existing contribute to the background. This gives rise to the fourth consideration. In fact backscattered electrons can contribute to the Auger signal

and as well as the background. The Auger enhancement ratio R is given by

$$R = 1 + \beta\eta$$

where η is the backscatter coefficient and $\beta \approx$ 2-3. The value of η is remarkably independent of the electron beam energy, while the background increases strongly as the primary electron beam energy increases. Consequently the background is enhanced with increasing primary electron beam energy. At high energy, the increase in the background overcomes the increase in the Auger signal. As a result, the signal/noise decreases significantly.

In general, the signal/noise decreases as the primary electron beam energy increases. This has been observed experimentally. Using a STEM, Chazelas (1986) observed that the signal/noise decreases by 30% for Ag (350 eV) and 15% for Au (2100 eV) for primary electron energy going from 30 to 100 kV. In order to achieve reasonable signal/noise, spectra were usually taken from the thin area of a specimen and long acquisition times were used.

§3.6 RESULTS AND DISCUSSION

The AES was first tested in a test chamber to ensure that it is in a working condition before installation into the microscope. The pressure of the test chamber was 2×10^{-8} torr. Figure 3.12 shows a spectrum taken from a dirty silver sample in the analog mode. The AC modulation voltage used was 2.0 eV. The primary electron energy was 3 keV and the emission current was 100 μA. Two major peaks, C and O from surface contaminants
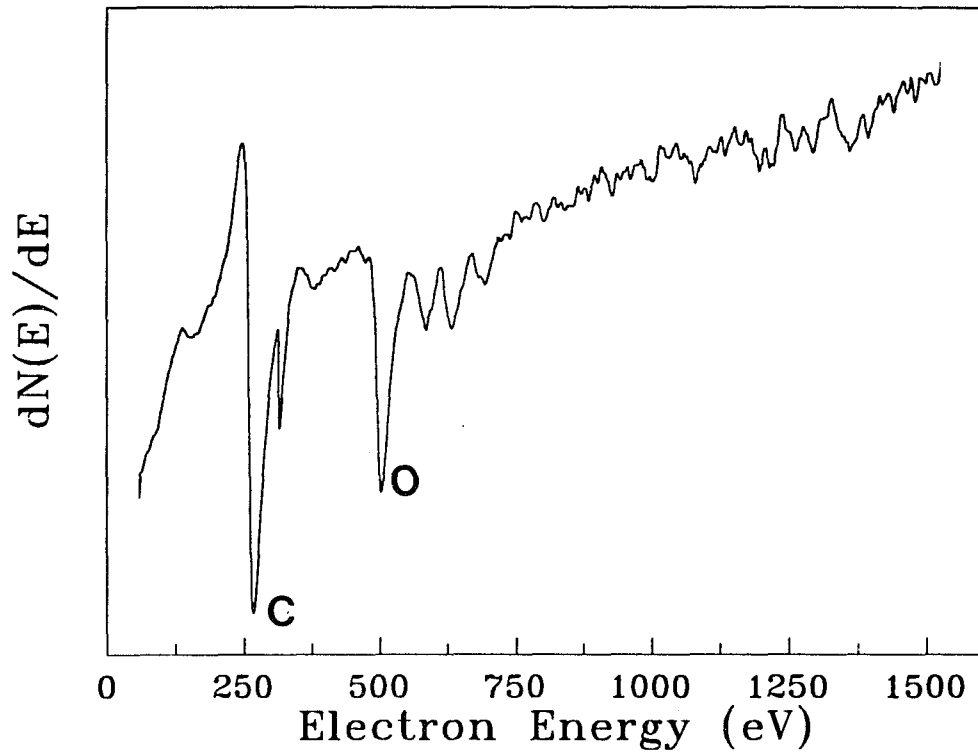
Figure 3.12 AES spectrum taken from a dirty silver sample in the chamber in the
analog mode. The primary electron energy was 3 keV and the AC
modulation was 2.0 V.

were identified.

Primary studies using the AES were first performed on a B-doped Si(111) sample after 4 keV, 25 mA Argon ion sputtering followed by 3 keV, 3 mA electron annealing. Figure 3.13 shows a spectrum taken from the thin area of the sample. The AES was operated in the analog mode with an AC modulation voltage of 2.0 eV and in sector sweeping field mode. While the PEELS spectrum only picked up the bulk Si, in the Auger spectrum three peaks, Si at 97 eV, B at 171 eV and C at 259 eV, were observed. The carbon peak was due to the surface contamination introduced during sample preparation. The boron peak was due to boron segregation from the bulk during electron annealing. This proved the advantage of the AES as a surface sensitive instrument. During the energy sweeping it was noticed that the primary electron beam drifted with the changing pass energy. This could induce the irregular variation in the background of the spectrum shown Figure 3.13 since the sample thickness could vary in the path of electron drift. Figure 3.14 was taken from the thicker area of the same sample under the same experimental condition. Only two major peaks, Si at 87 eV and C at 259 eV were observed. Boron was not detected due to the decrease in signal/noise. The decrease in the signal/noise can be attributed to the increase in the background produced by the x-ray photoelectrons, backscattered electrons and secondary electrons generated by both primary electrons and backscattered electrons.

One last point about the effect of x-rays should be addressed here. In an electron microscope the harsh x-ray environment not only increases the background of the spectrum, resulting in the decrease in the signal/noise, but also causes damage in the
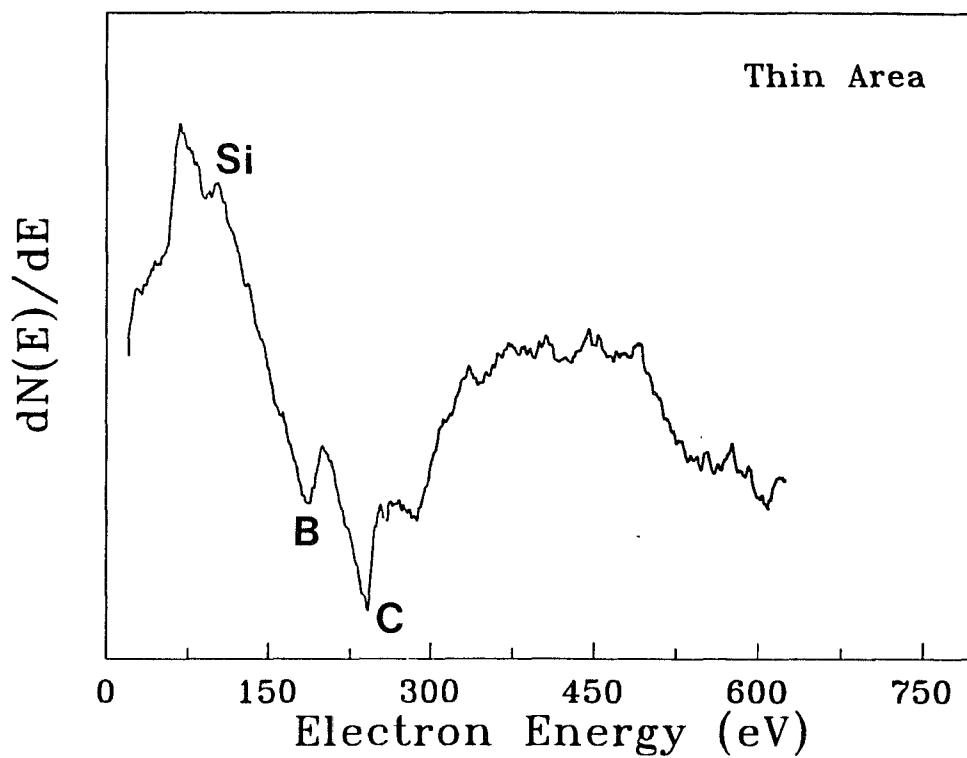
Figure 3.13 AES spectrum taken from the thin area of a B-doped Si(111) sample in
the UHV microscope in the analog mode. The primary electron energy
was 300 keV and the AC modulation was 2.0 V.
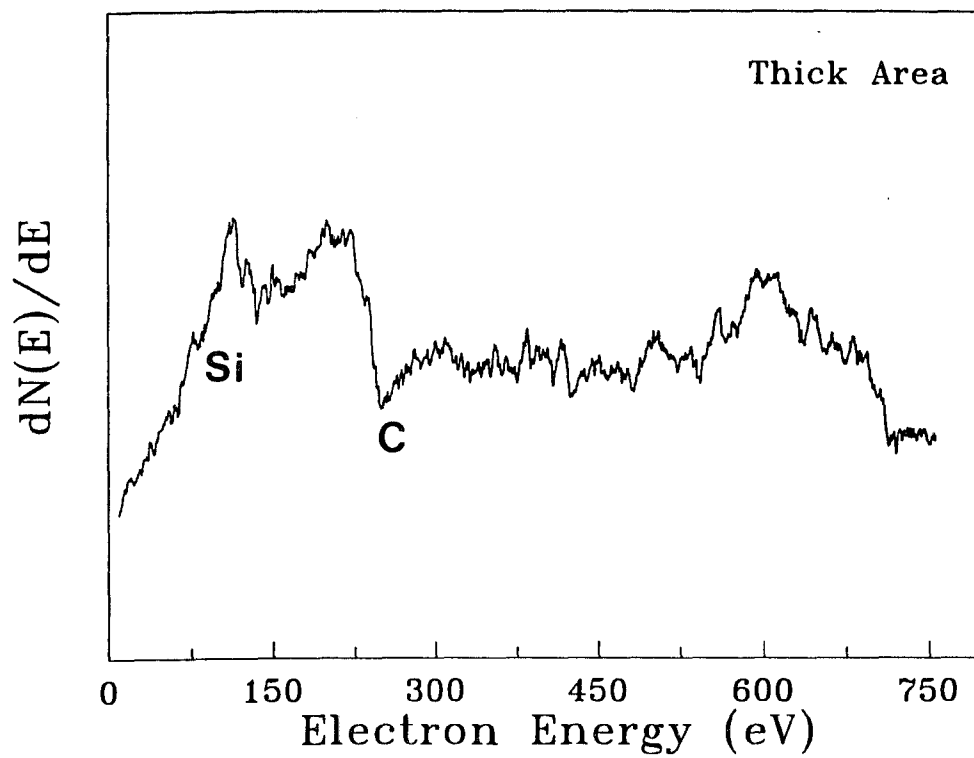
Figure 3.14 AES spectrum taken from the thick area of a B-doped Si(111) sample int
he UHV microscope in the analog mode. The primary electron energy
was 300 keV and the AC modulation was 2.0 V.

microchannel plate, resulting in the drastic decrease of its lifetime. The damage mechanism is probably low energy excitations, very similar to that by electrons. In normal applications the life time of a microchannel plate is usually on the order of few years. However in our application, the life time of the microchannel plate decreases to three months or three days in some cases, depending on the beam current used.

To summarize, a microscope-compatible AES has been designed and set-up. The AES has a energy resolution of 5.5% and can be operated in both analog mode and pulse counting mode. Currently only sector sweeping field mode is available and the constant transmission mode will be implemented. Future improvement and refinement of the AES will be discussed in Chapter 6

CHAPTER 4 ELECTRON-STIMULATED SURFACE RADIATION DAMAGE AND PHASE TRANSFORMATIONS IN V_2O_5

§4.1 INTRODUCTION AND REVIEW OF THE STRUCTURES AND PROPERTIES OF V_2O_5, V_4O_9, V_6O_{13} AND VO

The oxides of vanadium, in particular vanadium pentoxide, have been studied extensively because of their interesting physical properties (Goodenough 1971 and Dziembaj 1977). Vanadium metal oxides to its maximal valence oxide (V_2O_5) through a series of lower vanadium oxides with different crystal structures and homogeneities (See the V-O phase diagram in Figure 4.1). In VO, VO_2, VO_3 and V_2O_5, vanadium has a fixed valence state, while in the Magnéli phases generally expressed as V_nO_{2n-1} (2<n<8) and V_nO_{2n+1} (n=3,4,6), vanadium has mixed valence states. Vanadium oxides have many important technological applications. V_2O_5, for example, is a good developing agent in photographic industry, an ingredient for the manufacture of glasses with exceptional optical properties, and a member of a family of industrial catalysts for the partial oxidation of olefins. Several vanadium oxides exhibit useful metal-insulator (Morin 1959) or semiconductor-metal (Kachi 1963) transitions which are determined by temperature and pressure. In this section, the structures and properties of V_2O_5, V_4O_9, V_6O_{13} and VO will be reviewed.

§4.1.1 Structures and properties of V_2O_5

The structure of V_2O_5 was first determined by Bachman *et al* (1961). It has an
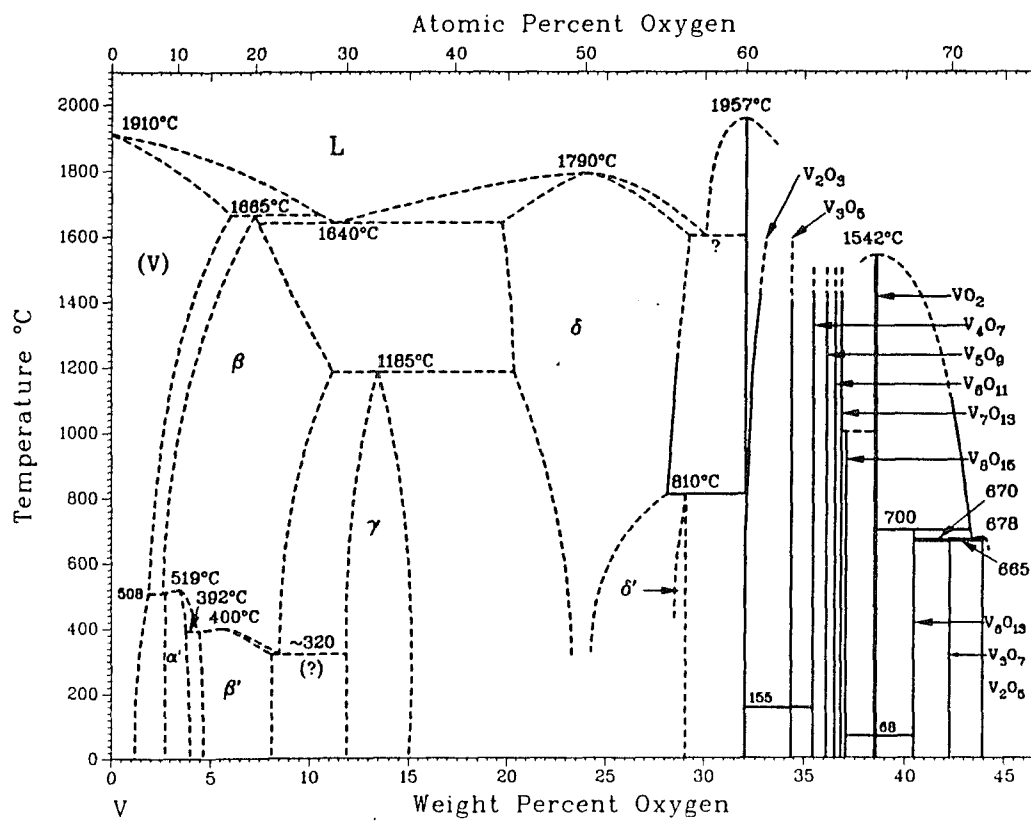
Figure 4.1   The phase diagram of the V-O system (Massalski 1990)

orthorhombic structure with lattice parameters: a = 11.510 Å, b = 3.563 Å, c = 4.269 Å. The unit cell contains four vanadium ions and ten oxygen ions and thus can be written as V_4O_{10}. The space group is Pmmn. Atoms are in the (4f) and (2a) positions:

(2a)   0, 0, x;   ½, ½, -z

(4f)   x, 0, z;   -x, o, z;   ½-x, ½, -z;   ½+x, ½, -z

with x, y, z listed in Table 4.1.

TABLE 4.1. Positions and Parameters of Atoms in V_2O_5

Atom	Position	x	y	z
V	(4f)	0.1487	0.0000	0.1086
O(1)	(4f)	0.1460	0.0000	0.4713
O(2)	(4f)	0.3191	0.0000	-0.0026
O(3)	(2a)	0.0000	0.0000	-0.0031

The building block of V_2O_5 is a deformed octahedron as shown in Figure 4.2. Each vanadium atom is surrounded by six oxygen atoms, forming a distorted octahedron with the vanadium atom at the center. The O_1 atoms form one strong bond (V-O_1 = 1.54 Å) which is commonly referred as the Vanadyl-bond. The O_2 atoms form three bonds (V-O_2 = 1.88 Å and V-O_2' = 2.02 Å) with bond angles of 104° (V-O_2' - V) and 143°. The O_3 atoms form two bonds (V-O_3 = 1.77 Å) with a bond angle of 125°. The O_1' atoms form a weak Vander Waals bond (V-O_1' = 2.785 Å), the longest bond in the octahedron. Consequently, V_2O_5 has a layer structure with the c-plane being the cleavage plane. In the b-direction, octahedra are linked together by corner sharing, giving rise to chains (See
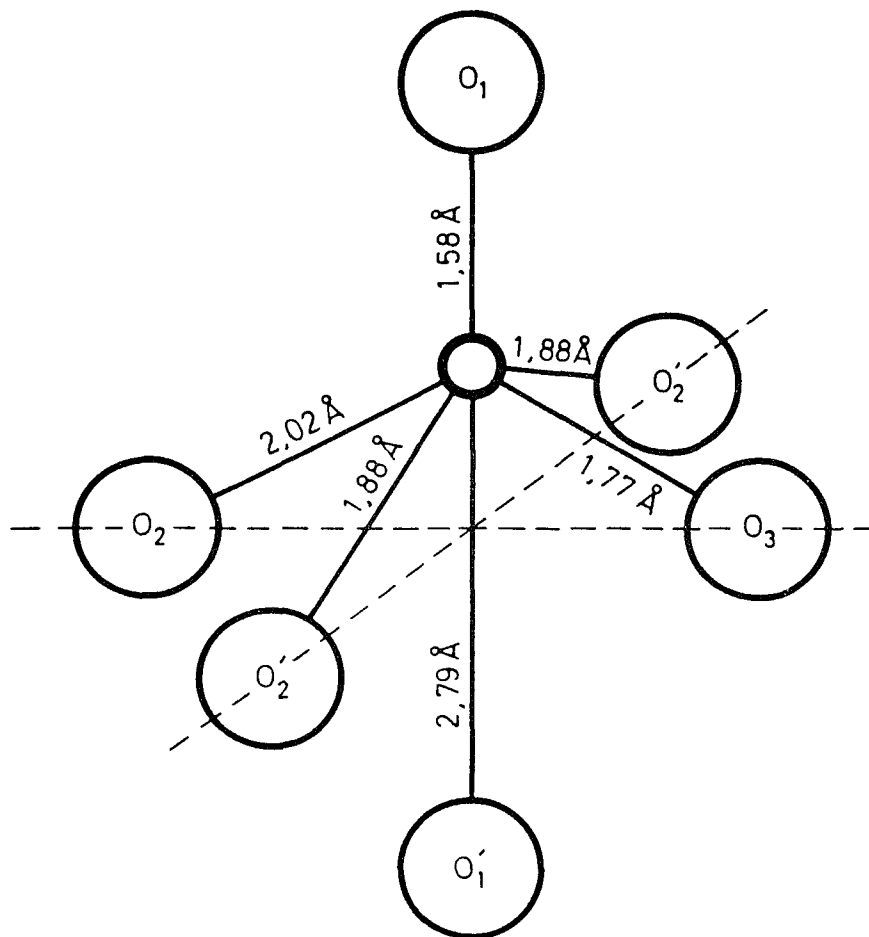
Figure 4.2   Building block of the V_2O_5 structure.   The V-O distances in the deformed octahedra are indicated (Fiermans 1979).

Figure 4.3). In the a-direction, these chains are linked together by the edge and corner

sharing. In the c-direction, the octahedra have common corners (See Figure 4.4). The

short distances between O_2-O_2' (2.39 Å) result in a strong repulsive force between the

O_2 atoms. It is thus expected that the V-O_2 bonds are the more easily broken V-O bonds,

resulting in another easy cleavage along the a-direction.

In pure and stoichiometric V_2O_5, the 3d-derived electronic levels are completely

empty. Assuming purely ionic bonding, V_2O_5 should be a perfect insulator at all

temperatures (Burns 1985). In reality, V_2O_5 is a diamagnetic n-type semiconductor with

a band gap energy of 2.5 eV (Kofstad 1972).

§4.1.2 Structures and Properties of V_4O_9

The structure of V_4O_9 remains a controversial issue in the literature. Over the years,

four different structural models have been proposed. In this section, the previous results

will be presented chronically.

The structure of V_4O_9 was first reported by Théobald et al (1969). The structure

obtained by these authors is tetragonal with lattice parameters: a = b = 8.235 Å and c =

10.32 Å. The density of 3.25 g/cm^3 corresponds to four formula units ($V_{16}O_{36}$) in one

unit cell.

In 1970, Wilhelmi et al (1970) reported another structure of V_4O_9. The structure was

identified to be orthorhombic using x-ray diffraction with lattice parameters: a = 17.926

Å, b = 3.631 Å and c = 10.32 Å. The space group is Pnma and the unit cell contains

four formula units ($V_{16}O_{36}$).
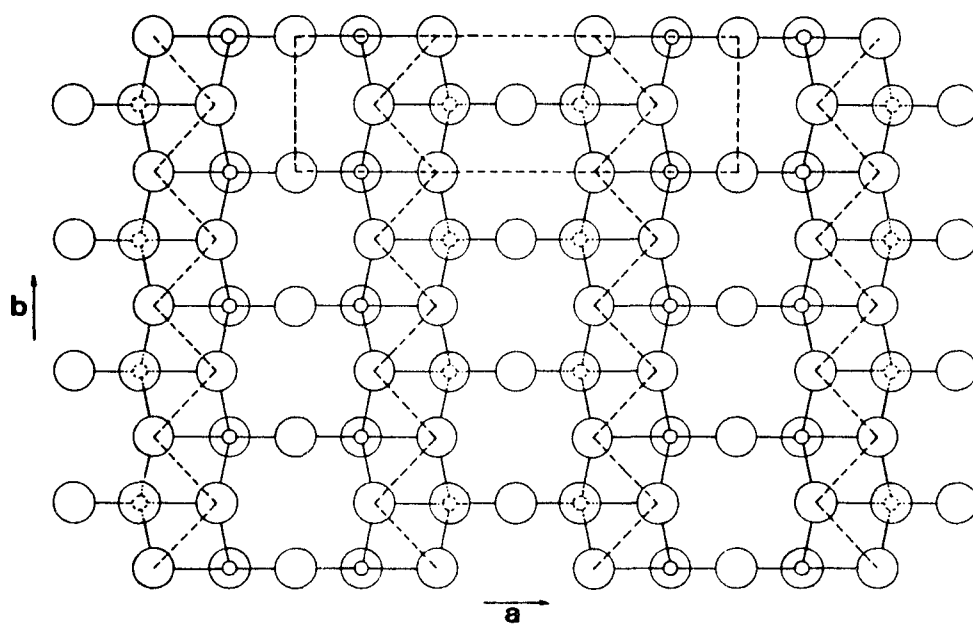
Figure 4.3   Projection of the V_2O_5 structure on the c-plane (Fiermans 1979).
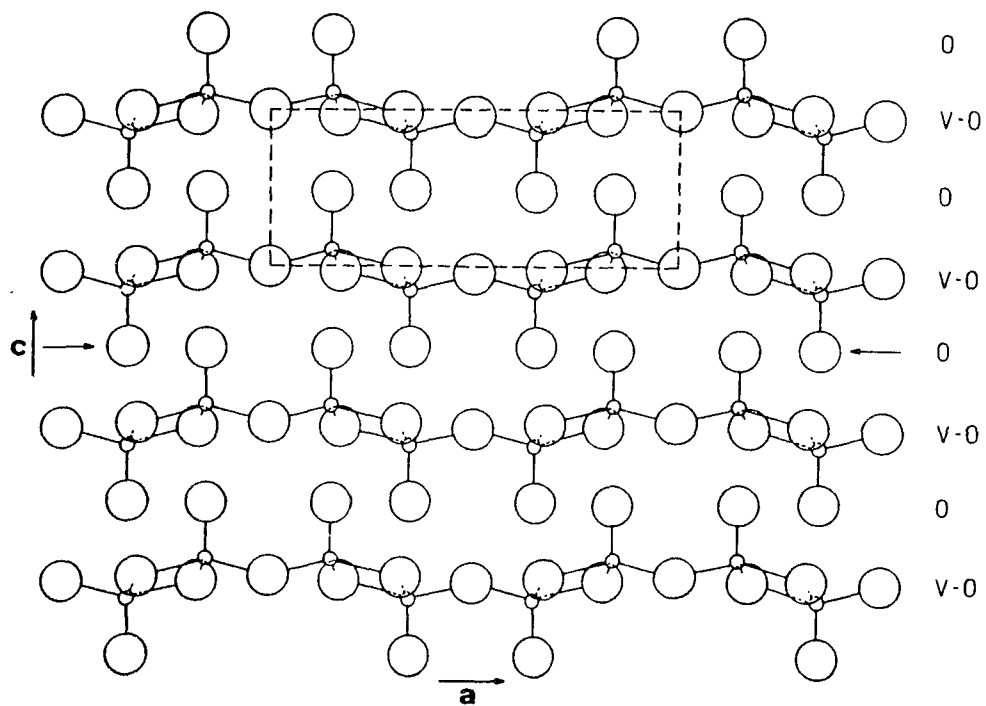
Figure 4.4 Projection of the V_2O_5 structure on the b-plane (Fiermans 1979). The Vander Waals bonds along the c-direction are not drawn to emphasize the easy cleavage parallel to the c-plane.

In the same year, Tilley *et al* (1970) observed a new structure of unknown chemical composition using electron diffraction. The chemical composition of this phase was later identified to be V_4O_9 by Grymonprez *et al* (1977). From the diffraction pattern, the lattice parameters of the new phase in plane were measured to be a = 8.1 Å and b = 10.4 Å. The tilting experiment revealed that this phase has an orthorhombic structure with the third lattice parameter of c = 16.1 Å.

In 1977, Grymonprez *et al* (1977) thermally reduced a V_2O_5 single crystal at 250°C in a sulphur atmosphere and obtained a new phase. This new phase topotaxically grew on the V_2O_5 single crystal and gave the same diffraction as the phase reported by Tilley *et al*. In reciprocal space, the relationship between the primitive unit cell of the new phase and the unit cell of V_2O_5 is shown in Figure 4.5a. In real space, the characteristic of the primitive unit cell of the new phase is listed in column A of Table 4.2 and schematically depicted in Figure 4.5b. From these relationships, a V_4O_9 structural model based on the ordered oxygen vacancies in the slightly distorted V_2O_5 lattice was proposed. In this structural model, one out of every ten oxygen atoms (10%) is removed from the c-plane of the V_2O_5 lattice in the manner as indicated by Figure 4.6. On the a-plane, oxygen vacancies are ordered to give a unit cell as shown in Figure 4.7. The primitive unit cell characteristics of the proposed structural model are listed in column B of Table 4.2.

(a)

(b)
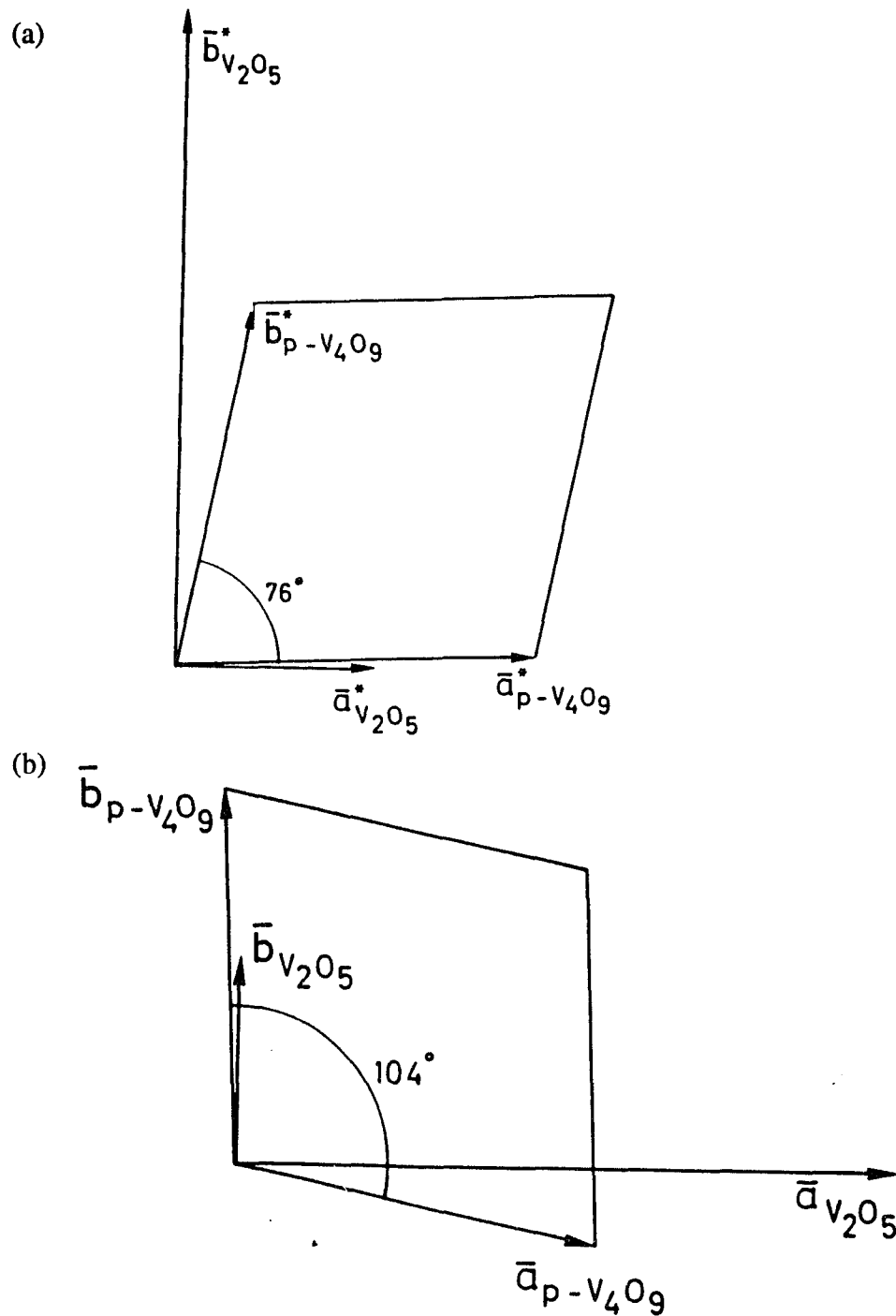
Figure 4.5 Schematic illustration of the orientation relationship between the V_4O_9 structure and the V_2O_5 structure. (a) in reciprocal space; (b) In real space (Fiermans 1979).
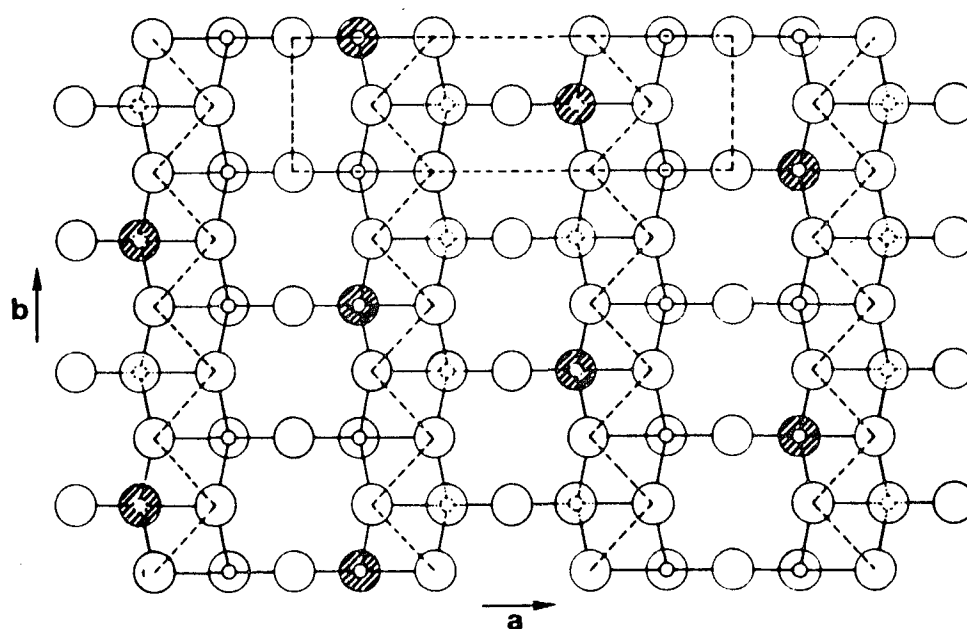
Figure 4.6   Projection of the V_2O_5 structure on the c-plane with removal of one tenth of the oxygen ions giving rise to the proposed V_4O_9 structure (Fiermans 1979). The shaded circles represent the oxygen vacancies.
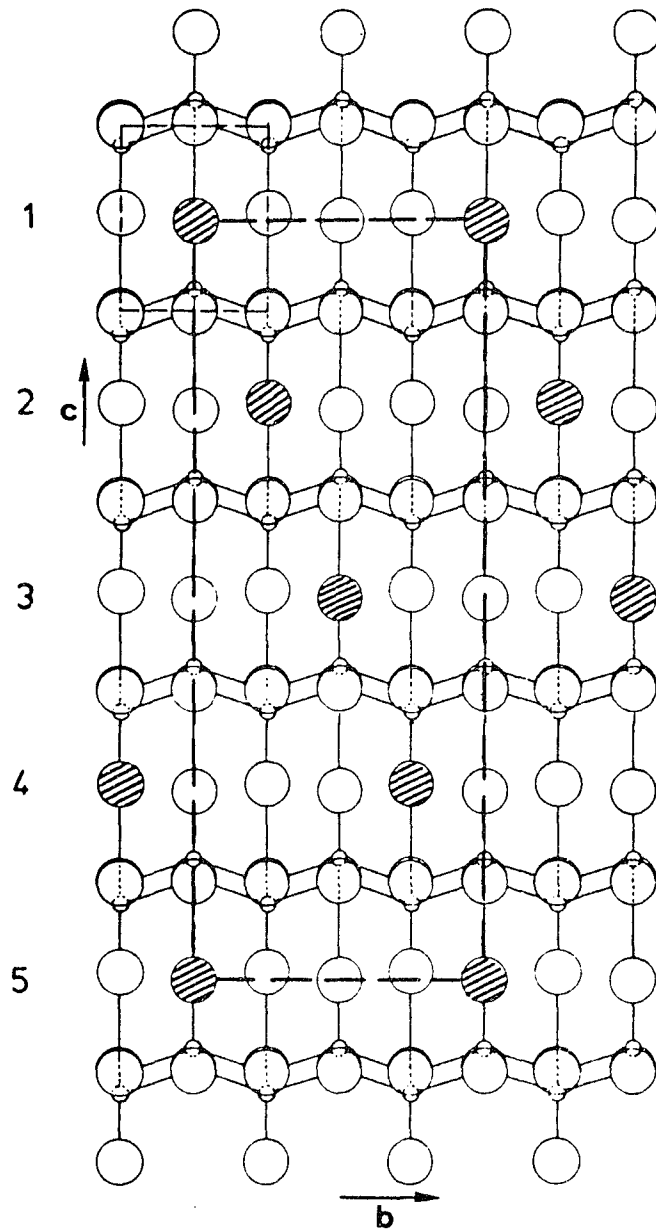
Figure 4.7   Projection of the proposed V_4O_9 structure on the a-plane (Fiermans 1979).
The shaded circles represent the oxygen vacancies.

75

TABLE 4.2 Comparison of the observed and proposed structures

A - Observed	B - Proposed
$\bar{a}_{p\text{-}V_4O_9} = 6.4$ Å	6.024 Å
$b_{p\text{-}V_4O_9} = 6.4$ Å	7.126 Å
$<b_{V_2O_5}\ b_{p\text{-}V_4O_9}> = 2°$	0°
$<b_{p\text{-}V_4O_9}\ \bar{a}_{p\text{-}V_4O_9}> = 104°$	107°
$<\bar{a}_{p\text{-}V_4O_9}\ a_{V_2O_5}> = 12°$	17°
$c_{V_4O_9} = 16.47$ Å	17.48 Å

By comparing the data in column A with those in column B, it is noticed that the proposed structure does not exactly match the experimental observations. The difference was accounted for by a distortion of the V_2O_5 lattice induced by oxygen vacancies.

Very little is known about the properties of the V_4O_9 phase due to the difficulties of obtaining a large single phase V_4O_9 crystal suitable for most property studies.

§4.1.3 Structures and Properties of V_6O_{13}

Two structures with V_6O_{13} composition have been reported in the literature. Both of them can be derived from the V_2O_5 structure by introducing shears along different crystallographic directions.

The structure of $\alpha\text{-}V_6O_{13}$ was first reported by Aebi (1948) and later refined by Wilhelmi et al (1971). $\alpha\text{-}V_6O_{13}$ has a monoclinic structure with lattice parameters: a = 11.922 Å, b = 10.138 Å, c = 3.680 Å and γ = 100.87°. The unit cell contains two formula units ($V_{12}O_{26}$). The space group is C2/m. Atoms are in the (4i) and (2b)

positions.

(4i) x, o, z; -x 0, -z; ½+x, ½, z; ½-x, ½, -z

(4b) ½, 0, 0; 0, ½, 0

Table 4.3 listed all the x, y, z values for atomic coordinations.

TABLE 4.3. Positions and Parameters of Atoms in α-V_6O_{13}

Atom	Position	x	y	z
V(1)	(4i)	0.35180	0.00000	-0.00041
V(2)	(4i)	0.42162	0.00000	0.36310
V(3)	(4i)	0.71332	0.00000	0.36513
O(1)	(4i)	0.17883	0.00000	0.00052
O(2)	(4i)	0.88194	0.00000	0.38776
O(3)	(4i)	0.24898	0.00000	0.40773
O(4)	(2b)	0.50000	0.00000	0.00000
O(5)	(4i)	0.38604	0.00000	0.19688
O(6)	(4i)	0.67817	0.00000	0.20062
O(7)	(4i)	0.56262	0.00000	0.40863

The structure of α-V_6O_{13} consists of distorted octahedra, the same as those in V_2O_5. The projection of this structure on the b-plane is shown in Figure 4.8. In the a-direction, the octahedra alternatively share common edges and corners. In the b-direction, the octahedra are joined together the same way as in V_2O_5. As a results the arrangement of the octahedra in the c-plane of α-V_6O_{13} is identical to the one in V_2O_5. In the c-direction, the octahedra alternately share common corners or edges and there is no alternation of
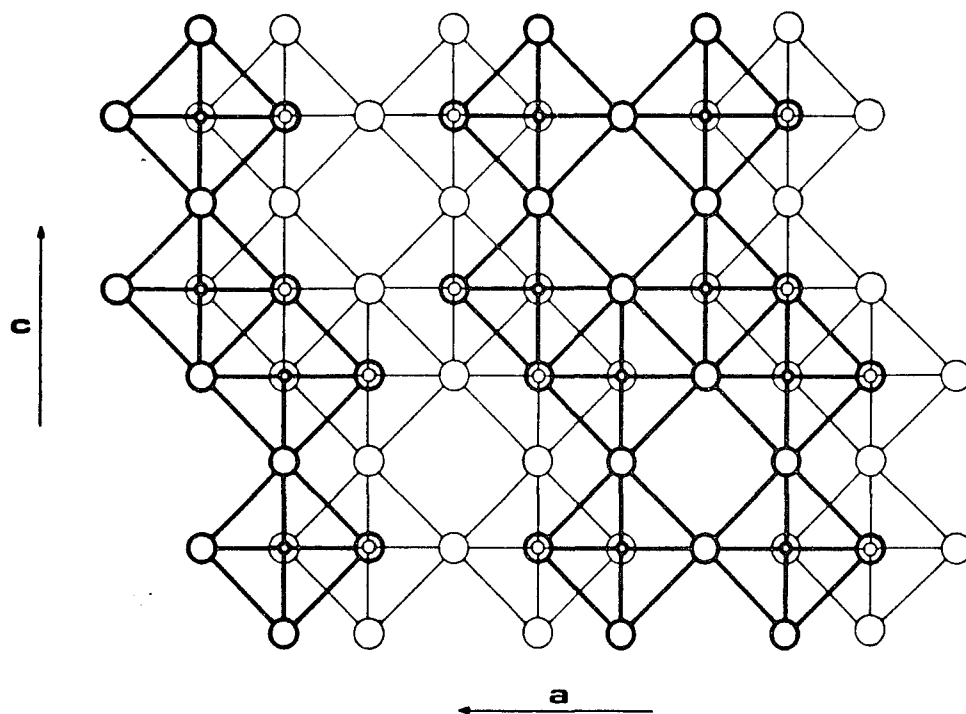
Figure 4.8   Projection of the α-V$_6$O$_{13}$ structure on the b-plane (Fiermans 1979).

vanadyl- and Vander Waals-bonds. Consequently, α-V_6O_{13} does not cleave as easily as V_2O_5.

The α-V_6O_{13} structure can be derived from the V_2O_5 structure by removing all the oxygen atoms in every third (001) oxygen atom plane and then introducing a shear plane with a shear vector of 1/6[1-30]. The shear relationship between α-V_6O_{13} and V_2O_5 is illustrated by Figure 4.9.

The second V_6O_{13} structure proposed by Ohno *et al* (1985) is orthorhombic with lattice parameters: a = 11.922 Å, b = 19.912 Å, c = 3.680 Å. This structure is usually referred to as β-V_6O_{13}. The space group is Cmma. The unit cell contains four formula units ($V_{24}O_{52}$). Atoms occupy the (16o), (8n), (8m) and (4g) positions.

$$(0, 0, 0\ )+ \qquad (\tfrac{1}{2}, \tfrac{1}{2}, 0)+$$

(16o) x, y, z; -x, -y+½, z; -x, y+½, -z; x, -y, -z

-x, -y, -z; x, y+½, -z; x, -y+½, z; -x, y, z

(8n) x, ¼, z; -x, -y, ¼, z; -x, ¾, -z; x, ¼, -z

(8m) 0, y, z; 0, -y+½, z; 0, y+½, -z; 0, -y, -z

(4g) 0, ¼, z; 0, ¾, -z

with x, y, z listed in Table 4.4.
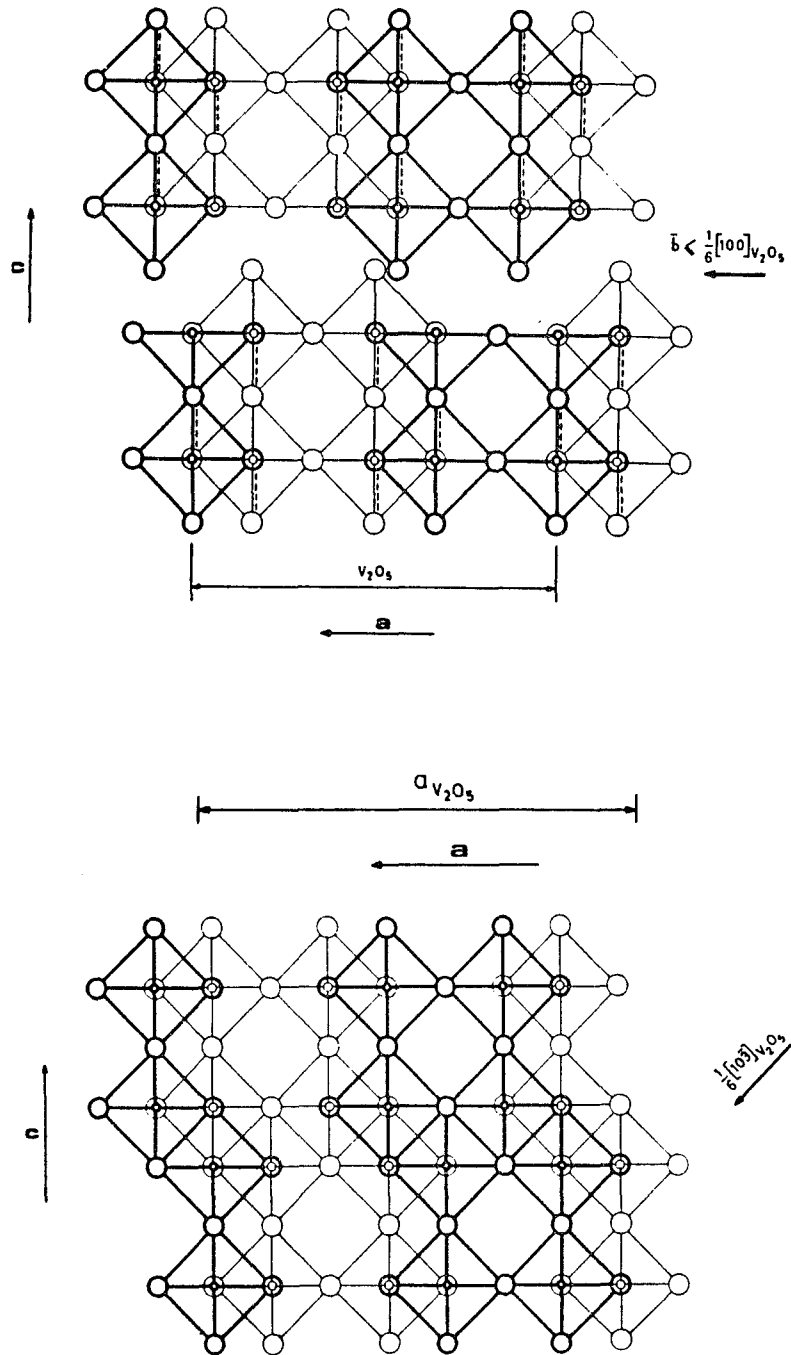
Figure 4.9 Schematic illustration of the shear relationship between the α-V_6O_{13} structure and the V_2O_5 structure (Fiermans 1979).

TABLE 4.4 Positions and Parameters of Atoms in β-V_6O_{13}

Atom	Position	x	y	z
V(1)	(16o)	0.150	0.007	0.750
V(2)	(8n)	0.140	0.000	0.750
O(1)	(16o)	0.180	0.005	0.250
O(2)	(16o)	0.140	0.150	0.750
O(3)	(8n)	0.180	0.000	0.250
O(4)	(8m)	0.005	0.000	0.750
O(5)	(4g)	0.000	0.000	0.750

This structure can be derived from V_2O_5 structure by removing all the oxygen atoms in every third (001) oxygen atom plane and then introducing a shear plane with a shear vector of ½[0-1-1] instead.

§4.1.4 Structure and Properties of VO

VO has a rocksalt structure with a lattice constant of 4.06 Å. The space group is Pm3m. The unit cell contains four formula units (V_4O_4) with atoms in the following positions:

V: (4a)   0, 0, 0;   ½, ½, 0;   ½, 0, ½;   0, ½, ½

O: (4b)   ½, ½, ½;   ½, 0, 0;   0, ½, 0;   0, 0, ½

The lattice is a face-centered cubic, in which each V^{2+} cation is surrounded by six O^{2-} anions in a regular octahedral arrangement. Each O^{2-} anion is also surrounded by six V^{2+} cations.

VO often exhibits nonstoichiometry with composition ranging from $VO_{0.75}$ to $VO_{1.30}$ (Banus 1970). The lattice parameter increases with increasing the O/V ratio. The primary defects in the nonstoichiometric VO are metal and oxygen vacancies. In the stoichiometric composition of VO, 15% of the vanadium and oxygen sites are unoccupied (Banus 1970 and Taylor 1970). At the oxygen rich limit, the anion sublattice is almost complete. But at the vanadium rich end, 13% of the cation sites remain vacant. Several studies have demonstrated the existence of extensive short-range ordering of oxygen vacancies in $VO_{1\pm x}$ (Bell 1971). At higher temperature (about 1000°C), defects in $VO_{1\pm x}$ are found to be completely disordered (Sørensen 1981).

The nonstiochiometry of $VO_{1\pm x}$ is related to its specific electronic structure. Vanadium ions in $VO_{1\pm x}$ have broad and overlapping d orbitals which produce strong metallic bonding between cations. Reports on the electrical properties of $VO_{1\pm x}$ have been conflicted. Kawano (1969) observed semiconducting behavior, while the thermoelectric power studies suggest metallic behavior. This reflects the complex band structure of VO. The electrical conductivity of $VO_{1\pm x}$ decreases with increasing oxygen content (Kofstad 1972). At a fixed composition, the conductivity increases with increasing temperature (Kofstad 1972). At -150°C, Morin (1959) and Austin (1962) observed a semiconducting/metallic phase transition which was not confirmed by other investigators (Sakata 1968, Takei 1968, Lochman 1969 and Kawano 1966).

§4.2 REVIEW OF PREVIOUS STUDIES ON THE REDUCTION OF V_2O_5 TO THE LOWER OXIDES

The reduction of V_2O_5 to lower oxides is known to occur as a result of various treatments such as heating (Tilley 1970, Colpaert 1973 and Grymonprez 1977), participation in a catalytic oxidation reaction (Fiermans 1979, Flood 1947 and Satava 1959), and electron (Curelaru 1980, Fiermans 1967, 1968, 1969, 1971, Suoninien 1981, Tilley 1970 and Tompkins 1985) or ion (Yin 1982, 1983) bombardment. Various experimental techniques such as, LEED, AES, XPS, apparent potential spectroscopy and TEM, have been used to study this phenomena. In this section, review of previous results will be given.

§4.2.1 Thermally-Induced Reduction

Thermally-induced reduction of V_2O_5 was first studied by Tilley (1970) using electron microcopy. V_2O_5 crystals were annealed in air at various temperatures before being loaded into the microscope for structural examination. At 100°C, a 7-fold superstructure was observed. Along the b-axis, the dimension of the unit cell of the superstructure is exactly 7 times of V_2O_5. Along the c-axis, the dimension of the new unit cell is the double of V_2O_5. At 150°C, another phase was obtained. This phase has a crystal structure identical to that of V_4O_9 as described by Théobald (1969). At 400°C, samples were reduced to a mixture of V_6O_{13} and V_3O_7

The effects of thermal treatment in UHV at temperatures up to 550°C were later studied by Colpaert et al (1973). Samples after the following pretreatments were studied.

(a) UHV-cleaved and pretreated at about 550°C;

(b) air-cleaved and pretreated at about 550°C in oxygen (1 atm.);

(c) air-cleaved and pretreated at about 300°C in oxygen (1 atm.);

(d) air-cleaved without further treatment.

All the samples were then heated in UHV at about 550°C after the pretreatments.

After the heat treatment no phase transformation in samples (a) and (b) was detected by x-ray diffraction or by LEED. However, infrared-absorption measurements indicated that a homogeneous oxygen loss had taken place in these samples.

During the thermal treatment sample (c) decomposed into α-V_6O_{13}. X-ray diffraction showed that α-V_6O_{13} was formed topotaxically on V_2O_5 with the b-plane parallel to the b-plane of V_2O_5.

After the heat treatment sample (d) showed a LEED pattern characteristic of V_2O_5. However, x-ray diffraction revealed that the sample partially decomposed into V_4O_9. The V_4O_9 phase formed topotaxically on the V_2O_5 with the a-plane parallel to the c-plane of V_2O_5. Table 4.5 summarizes these results.

TABLE 4.5 Summary of Results of Thermally-Induced Reduction in V_2O_5

Nature of the Surface	Pretreatment	UHV-treatment	Results		
			LEED	X-ray	I.R.
UHV-Cleaved	-	550°C (24 hr)	V_2O_5	V_2O_5	Homog. O_2 loss
Air-Cleaved	550°C, 1 atm O_2 (24 hr)	550°C (24 hr)	N.O.	V_2O_5	Homog. O_2 loss
Air-Cleaved	350°C, 1 atm O_2 (24 hr)	550°C (24 hr)	N.O.	$\alpha\text{-}V_6O_{13}$	-
Air-Cleaved	-	550°C (24 hr)	V_2O_5	V_4O_9	-

N.O. = No Observation; I.R. = Infrared Absorption Spectrum; Homog. = Homogeneous.

§4.2.2 Electron and Ion Induced Reduction

Electron-induced reductions of V_2O_5 were first studied by Fiermans et al (1968, 1969) using LEED. The V_2O_5 (001) surface, cleaved in UHV, exhibited a rectangular LEED pattern, characteristic of the V_2O_5 (001) surface. Under the irradiation of the electron beam (10 - 100 eV), this surface underwent a phase transformation at room temperature indicated by the appearance of a new LEED pattern. This LEED pattern can be identified as the two dimensional pattern from the $\alpha\text{-}V_6O_{13}$ (001) surface. The interpretation was confirmed by the LEED pattern taken from a single crystal $\alpha\text{-}V_6O_{13}$ (001) surface. Furthermore it was reported that the $\alpha\text{-}V_6O_{13}$ phase was remarkably stable under further electron irradiation.

The kinetics of the phase transformation were studied by changing the sample

temperature. At 120°K the transition rate decreases drastically. At higher temperature, the beam did not produce the reduction, i.e. the rectangular LEED pattern, characteristic of the V_2O_5 (001) surface remained. These observations were interpreted in terms of reaction kinetics. At the low temperature where the rate limiting step is bulk diffusion, the reduction occurred. At the higher temperature where the rate limiting step was the surface reaction, i.e. oxygen desorption, homogeneous oxygen loss was observed without any structural modifications.

The electron induced reduction of V_2O_5 was also studied by AES (Tompkins 1985). In their experiment, Auger transitions that involve the 3d-electron level were used as fingerprints to identify the reduction of V_2O_5. The spectrum taken from a V_2O_5 (001) single crystal after 1 min irradiation of a 2 keV electron beam with a beam flux of 1.54×10^3 $\mu A/cm^2$ exhibited an identifiable feature at 470 eV. This feature was absent in an undisturbed V_2O_5 crystal and was caused by the $L_3M_{23}M_{45}$ Auger transition (See the energy level scheme of V_2O_5 in Figure 4.10), which indicated the progressive occupation of the 3d electron level and therefore, the reduction of the V_2O_5 single crystal to its lower oxides. However no quantitative studies on the reduced surface were performed to obtain the chemical composition of the lower oxide.

The ion-induced (Argon ions) reduction of V_2O_5 was studied by Yin *et al* (1982, 1983) using AES and XPS. The results were similar to the results of electron irradiation. Ion bombardment induced reductions in V_2O_5 was observed as indicated by the pronounce enhancement of the $L_3M_{23}M_{45}$ Auger transitions which involve the 3d electrons (See Figure 4.10).

§4.2.3 Reduction in Catalytic Oxidation Reactions

It is well known that V_2O_5 is an important catalyst for the partial oxidation of olefins. In this process, the catalytic properties of V_2O_5 depend strongly on the ability to provide lattice oxygen as a reactant in the oxidations of the hydrocarbons. It is believed that the lower oxides play an important role. These ideas were confirmed by the XPS studies of the oxidation of propene on a V_2O_5 single crystal (Fiermans 1980). The results are summarized below:

1. The freshly cleaved V_2O_5 (001) surface was inactive for this reaction. The XPS spectra of the valence region of the vanadium and oxygen remained unchanged and no macroscopic changes were observed by SEM.

2. Only after a pre-reduction treatment (heating, for example), was a catalytic activity observed. This was accompanied by changes in the XPS spectra. The XPS spectrum of the valence region exhibited a peak at about 2 eV binding energy corresponding to the V^{4+} ions in the V_6O_{13}. In the core excitation region, the oxygen peak decreased drastically.

3. After a prolonged catalytic reaction, the single crystal surface was completely damaged. The new peak at 2 eV binding energy in the XPS spectrum of the valence region became even clearer, indicating the further reduction of the V_2O_5 catalyst during the reaction. At the same time the intensity of the oxygen peak became smaller, suggesting the loss of oxygen in the oxidation reaction. The presence of the lower oxides were confirmed by x-ray diffraction.

E

0

C.B.   VM$_{4,5}$ // 3d4s

- 3.3
- 4.5 — — — — — — — — — — E$_F$
- 5.7
V.B.   O2p
- 10.2

OL$_1$ 2s
- 24.5

VM$_{2,3}$ 3p ½ ³⁄₂
- 46

VM$_1$ 3s
- 73

VL$_3$ 2p ³⁄₂
- 521.5

VL$_2$ 2p ½
- 528.5

OK 1s
- 536.5

VL$_1$ 2s
- 636,7
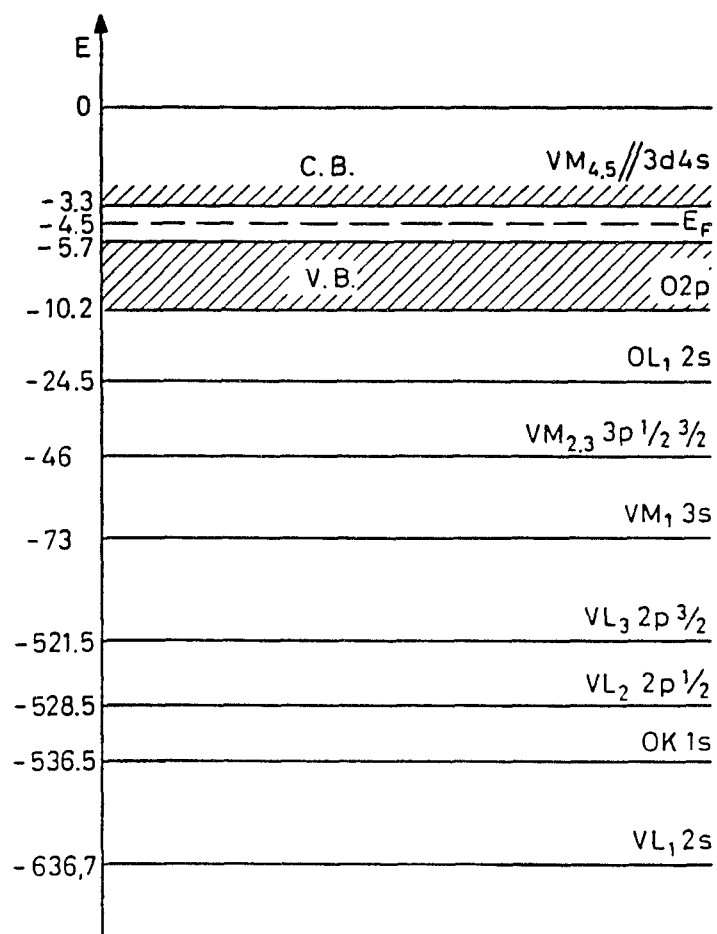
Figure 4.10   The V$_2$O$_5$ energy level scheme (Fiermans 1971).

§4.3 EXPERIMENTAL DETAILS

In this study, specimens for HREM studies were made from high purity V_2O_5 powders (99.999%, AESAR/Johnson Matthey). Table 4.6 shows the impurity elements detected.

TABLE 4.6 Impurity elements detected in V_2O_5 (from Johnson Matthey)

Impurity	Ca	Fe	Mg	Mn	Si	Ti
Concentration (0.001%)	< 1	7	< 1	< 1	2	5

TEM samples were prepared by grinding V_2O_5 powders in an alumina mortar with a pestle while dispersed in methanol or acetone, then depositing on a holey carbon film supported on a copper grid. In order to reduce surface hydrocarbon contaminations, specimens were baked for 5 to 10 min on an 150 watt light bulb just prior being loaded into the microscope. Specimens for UHV-HREM studies were baked in the side chamber for about 24 hours at about 150°C before being transferred into the microscope column.

Microscope observations were made with both the Hitachi H-9000 and UHV H-9000 electron microscopes operated at 300 kV accelerating voltage. The same experiments were repeated with 100 kV accelerating voltage in order to rule out any knock-on effects. The new phases were identified by selected area electron diffraction (SAED), HREM, and multislice image simulation. A standard laser optical bench was used to obtain optical diffraction patterns from a sample area as small as 2000 Å. The lattice parameters of the new phases perpendicular to the beam direction were measured with an accuracy of 5% in the diffraction patter. Lattice parameters in the beam direction were measured by

tilting the specimens or analyzing the second order laue zone.

Samples for ESCA studies were prepared by pressing V_2O_5 powders into pellets and then left in the prechamber for outgassing overnight. A Varian LEED electron gun (0 - 3 keV and 0 - 3 μA) was installed in the SIMS chamber as a radiation source. A VG quadruple mass spectrometer was used to detect the desorbing species during electron irradiation. Before and after irradiation the surface chemistry was studied by XPS.

§4.4 RESULTS AND DISCUSSION

This section presents the results of V_2O_5 irradiated by electrons of different energies and fluxes in non-UHV and UHV environments. This study is a result of the collaborating efforts of Dr. V. A. Volpert, Ms. H.-J Fan and myself. Dr. Volpert's contribution was in the solving of the diffusion equations. The HREM results in the high energy regime and in non-UHV were partly obtained by Ms. H.-J. Fan. The results in the low energy regime and in UHV, the image simulation of V_4O_9, the interpretations, part of the development of the theoretical model and all of the analysis of the numerical simulations were done by myself.

§4.4.1 HREM Studies of High Energy Electron Irradiation

Flux = 0.5 A/cm^2

Figure 4.11 is a time sequence of SAED patterns taken from a V_2O_5 single crystal along [001], showing the evolution of the phase transformation under this flux condition.

The electron energy was 300 keV. Figure 4.11a was taken as soon as the crystal was tilted to the zone axis. Although no structural changes were observed in the diffraction pattern, the high resolution image taken from the same area revealed that the surface of V_2O_5 had already changed (see Figure 4.12). This indicates that the phase transformation was initiated at the surface. In Figure 4.12, a small square network of lattice fringes can be clearly seen. The spacing of the lattice fringes is 2.0 Å, corresponding to the 200 spacing of VO.

At the surface, the oxygen atoms were lost so rapidly that the phase transformation went to VO directly as shown in Figure 4.12. With increasing irradiation time, the intermediate phases, V_4O_9 and V_6O_{13}, can been seen in Figure 4.13. The diffraction pattern taken after about 10 min irradiation shows the same observation. In Figure 4.11b two extra sets of diffraction spots marked by T and T′ appeared due to V_4O_9 and the V_4O_9 twin. The new diffraction pattern in Figure 4.11b had a rectangular unit cell with a = 8.23 Å and b = 10.03 Å. From both SAED and HREM, it can be derived that V_4O_9 has a well defined orientation relationship with the parent phase V_2O_5, shown as the following:

$$(110) \ V_4O_9 \ // \ (100) \ V_2O_5$$

$$(001) \ V_4O_9 \ // \ (001) \ V_2O_5$$
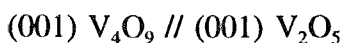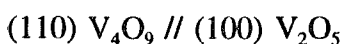
Although it was not observed in the diffraction patten in Figure 4.11b, a thin layer of a third phase, β-V_6O_{13} between V_4O_9 and VO can be seen in the HREM image (See Figure 4.13). With increasing irradiation time, the V_4O_9 phase vanished and was overtaken by the β-V_6O_{13} phase as shown in Figure 4.14 taken after 20 min irradiation,
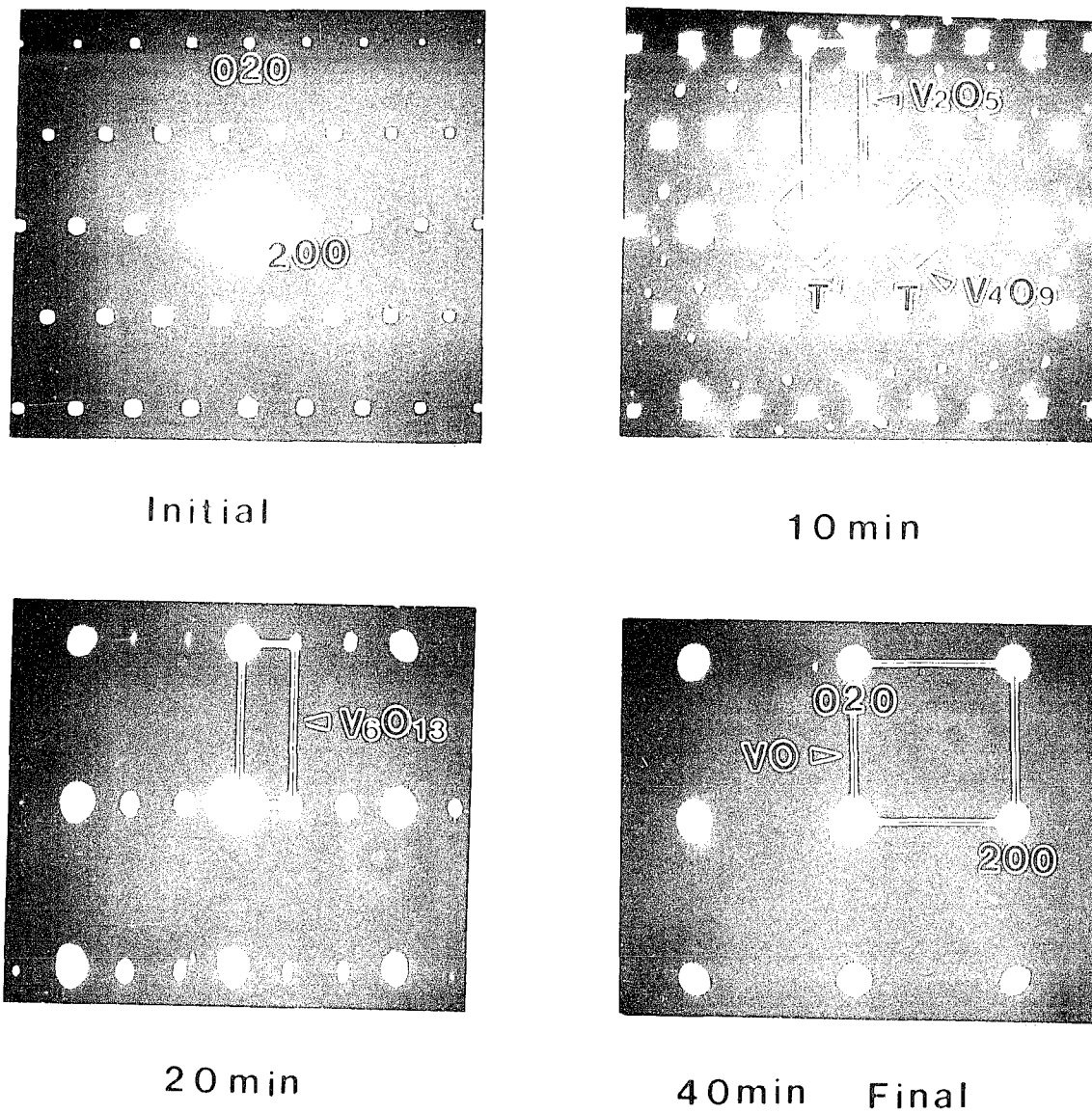
Figure 4.11   Time sequence of SAED patterns of V_2O_5 [001] under electron irradiation with a flux of 0.5 A/cm^2. a) initial; b) 10 min; c) 20 min; d) 60 min (Courtesy of H.-J. Fan).
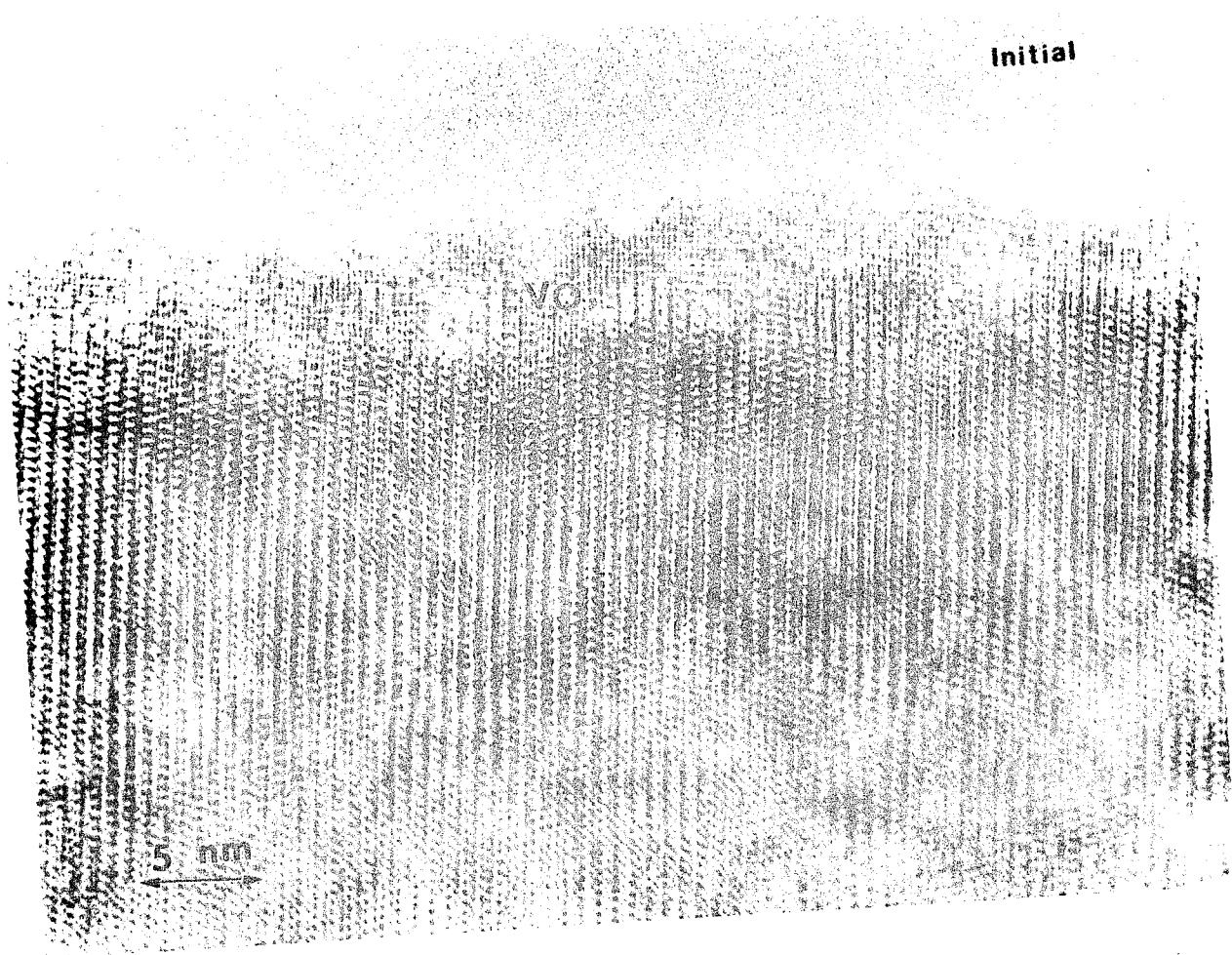
Figure 4.12 HREM image of V_2O_5 [001] taken as soon as a single crystal of V_2O_5 was tilted to the zone axis showing the formation of the VO phase at the surface edge. The flux was 0.5 A/cm^2 (Courtesy of H.-J. Fan).

in which only β-V_6O_{13} and VO were observed. This observation suggests that the growth of β-V_6O_{13} was faster than that of V_4O_9, i.e., the β-V_6O_{13}/V_2O_5 interface had a faster migration velocity than the V_4O_9/V_2O_5 interface. The interplanar spacings measured from β-V_6O_{13} were 5.8 Å and 1.8 Å, corresponding to values of d_{200} and d_{020} of β-V_6O_{13}. These observations were confirmed by the diffraction pattern. As shown in Figure 4.11c taken after 20 min irradiation, diffraction spots of V_4O_9 vanished, and two new sets of diffraction patterns due to β-V_6O_{13} [001] and VO [001] appeared. The epitaxial relationship between V_2O_5 and V_6O_{13} was found to be the following:

$$(001)\ \beta\text{-}V_6O_{13}\ //\ (001)\ V_2O_5$$

$$(100)\ \beta\text{-}V_6O_{13}\ //\ (001)\ V_2O_5$$
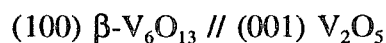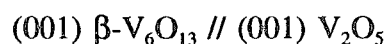
Upon continuing irradiation, β-V_6O_{13} also vanished. Only VO was observed in Figure 4.15, taken after 60 min irradiation. Figure 4.11d shows the corresponding diffraction pattern of VO [001] taken from the same area. The epitaxial relationship of VO to V_2O_5 is:

$$(110)\ VO\ //\ (100)\ V_2O_5$$

$$(001)\ VO\ //\ (001)\ V_2O_5$$
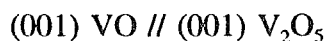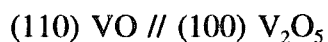
No further changes were observed in VO under continuous electron irradiation, indicating that VO was stable under the beam. This can be attributed to the metallic property of VO, meaning that electrons in the conduction band are delocalized. Therefore the electronic excitations delocalize over the conduction band before they can be transferred to an atom to cause permanent displacement. The same process takes place in metals (Hobbs 1979).
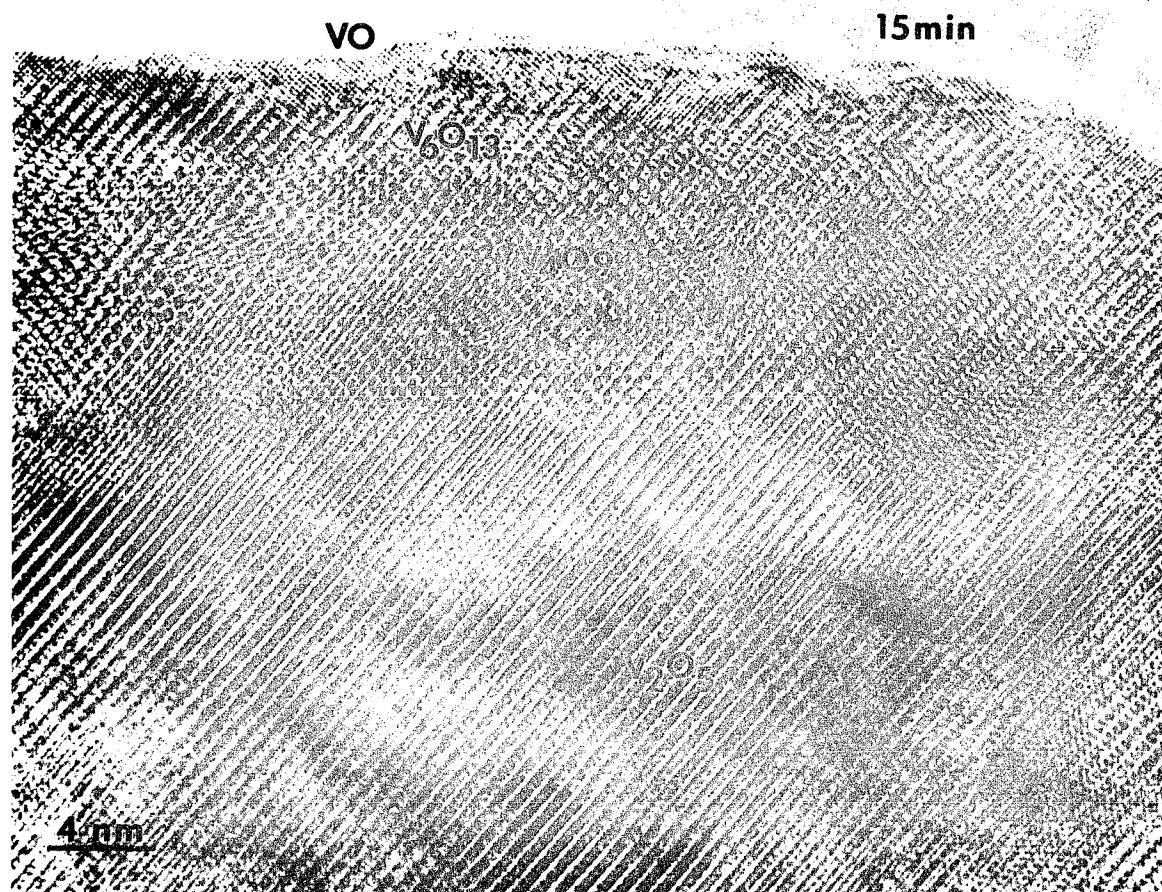
Figure 4.13 HREM image of V_2O_5 [001] taken after 15 min electron irradiation at a flux of 0.5 A/cm^2 shows the formation of intermediated phases of V_4O_9 and V_6O_{13} (Courtesy of H.-J. Fan).

20min

VO

V_6O_{13}

5 nm
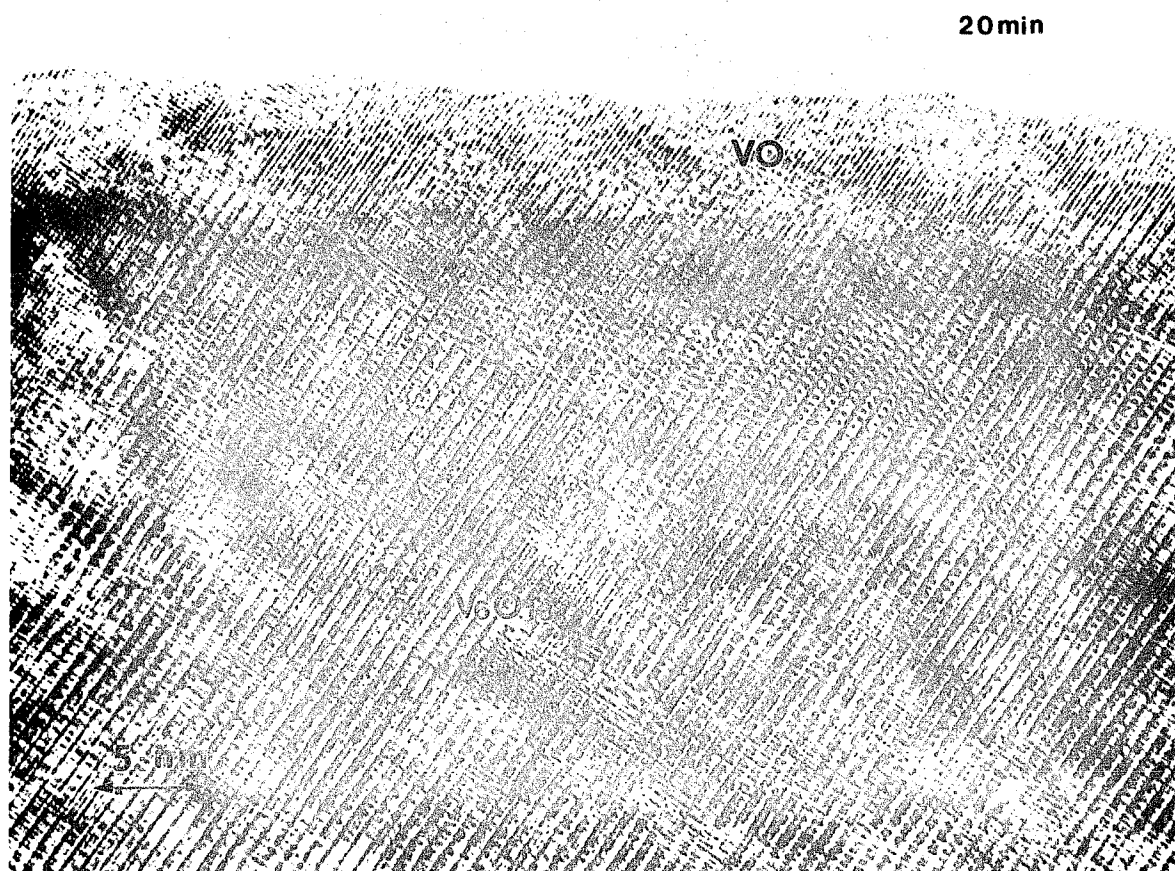
Figure 4.14 HREM image of V_2O_5 [001] taken after about 20 min electron irradiation at a flux of 0.5 A/cm^2 shows that V_4O_9 vanished and was replaced by V_6O_{13} (Courtesy of H.-J. Fan).

Table 4.7 summarized the time evolution of the phase transformation in V_2O_5 under electron beam irradiation with a flux of 0.5 A/cm^2.

TABLE 4.7 Summary of the phase transformation in V_2O_5

Electron Energy = 300 kev, Flux = 0.5 A/cm^2, Vacuum = 3 x 10^{-7} torr

Time (min)	Phases Observed
Initial (5)	V_2O_5 and VO
10	V_2O_5, V_4O_9, V_6O_{13} and VO
20	V_2O_5, V_6O_{13} and VO
Final (60)	VO

Flux = 2.0 A/cm^2

The phase transformation under this flux condition has a different route and was also initiated at the surface. Figure 4.16 shows the HREM image taken after about 15 min of irradiation. In this image, only two phases V_4O_9 and VO were observed. V_6O_{13} was never observed under this flux condition. The end product was also VO. The time evolution for this flux condition is summarized in Table 4.8

TABLE 4.8 Summary of phase transformation in V_2O_5

Electron Energy = 300 keV, Flux = 2.0 A/cm^2, Vacuum = 3 x 10^{-7} torr

Time (min)	Phases Observed
Initial (5)	V_2O_5 and VO
15	V_2O_5, V_4O_9 and VO
Final (60)	VO

Final
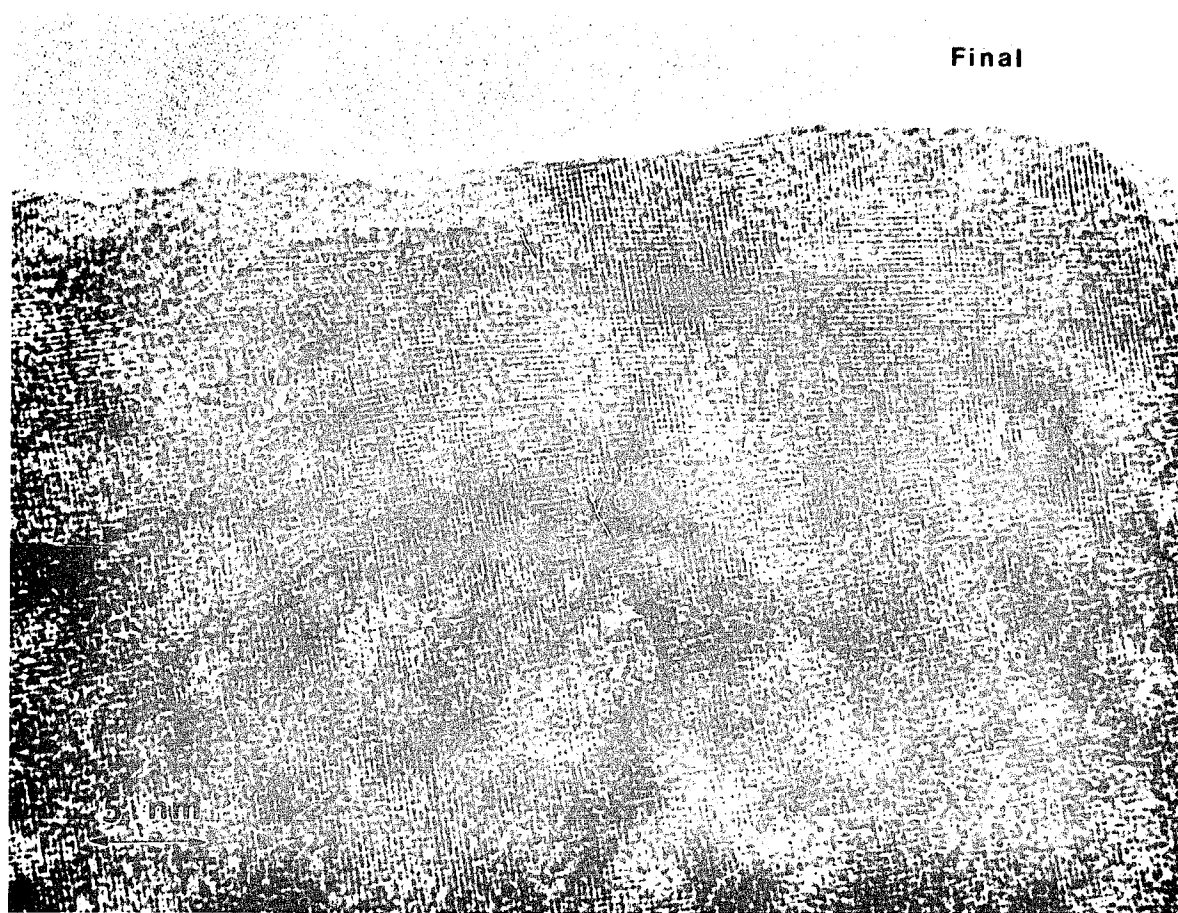
Figure 4.15   HREM image of V_2O_5 [001] taken after 60 min electron irradiation at a flux of 0.5 A/cm^2 shows the end product VO (Courtesy of H.-J. Fan).
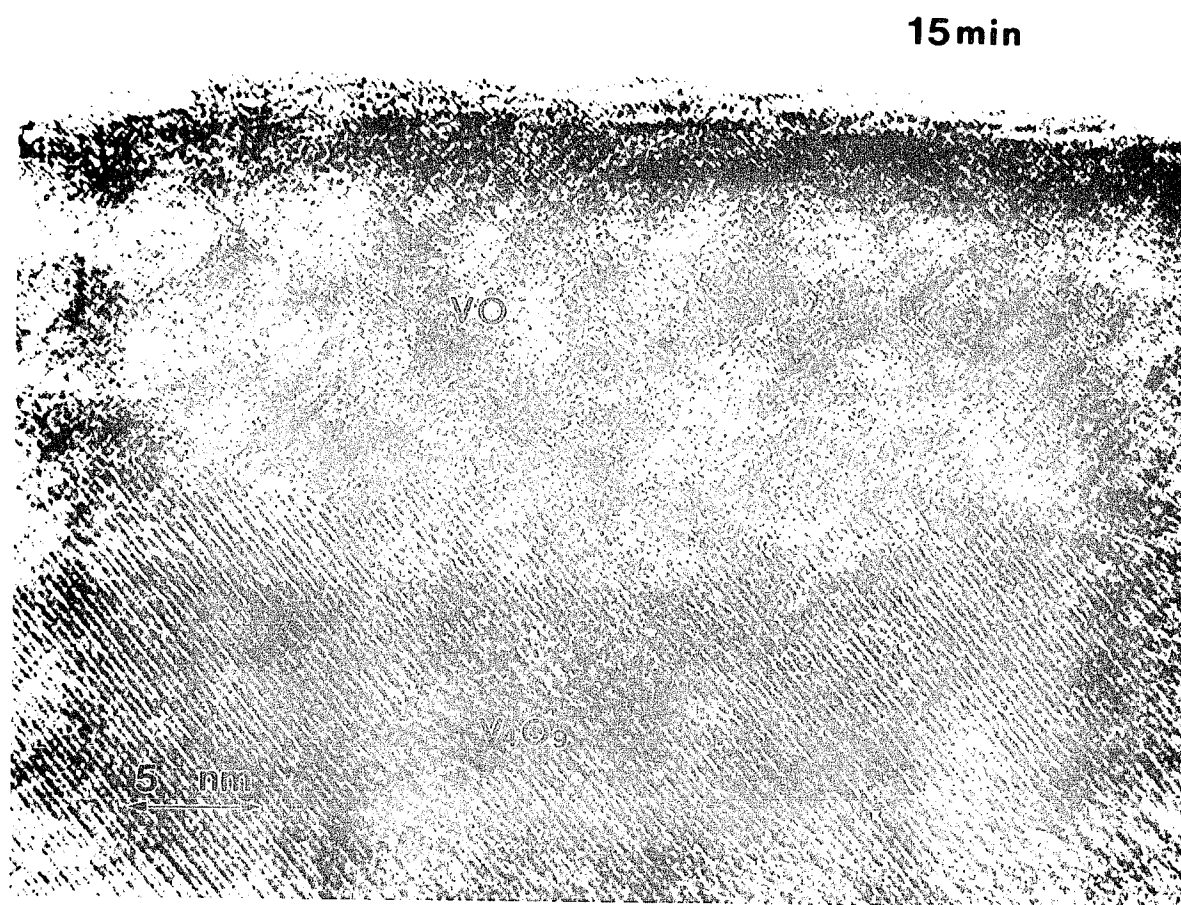
15min

Figure 4.16   HREM image of V_2O_5 [001] taken after about 15 min electron irradiation at a flux of 2.0 A/cm^2 shows the formation of V_4O_9 and VO (Courtesy of H.-J. Fan).

Flux = 5 A/cm²

Figure 4.17 shows the initial image of a V_2O_5 single crystal oriented along [001] after 5 min of irradiation with a 5 A/cm². The phase transformation occurred simultaneously at the surface and in the bulk. Formed at the surface was a thin layer of VO. In the bulk, an inhomogeneous mixture of VO and β-V_6O_{13} were observed This observations can be explained by a supersaturation of oxygen vacancies. At the high flux condition, oxygen vacancies were quickly created in the bulk. While some of the vacancies migrated to the surface and were annihilated, the majority of the vacancies remained in the bulk. In some local regions of the specimen, the concentration of oxygen vacancies supersaturated, resulting in the precipitation of small domains of VO and β-V_6O_{13}. The inhomogeneous mixture of β-V_6O_{13} and VO could be formed via two processes. One is the transformation of V_2O_5 to β-V_6O_{13} followed by the precipitation of VO in the β-V_6O_{13} matrix. The second is that precipitation of β-V_6O_{13} and VO occurred simultaneously. However, the phase transformation took place so quickly that these two processes could not be distinguished experimentally, the domain structure of the VO phase can be seen in the elongation of diffraction spots in the diffraction pattern inset in Figure 4.17, which is inversely proportional to the average size of the VO domains. Under this flux condition as shown in Figure 4.18 taken after 60 min electron irradiation. The domain structure remained. The diffuse scattering in the diffraction pattern inset indicates that the VO phase is nonstoichiometric, probably oxygen deficient and can be presented by VO_{1-x}, where x is a small value. The average domain size of VO was measured from the elongation in the diffraction spots. It was found that the average
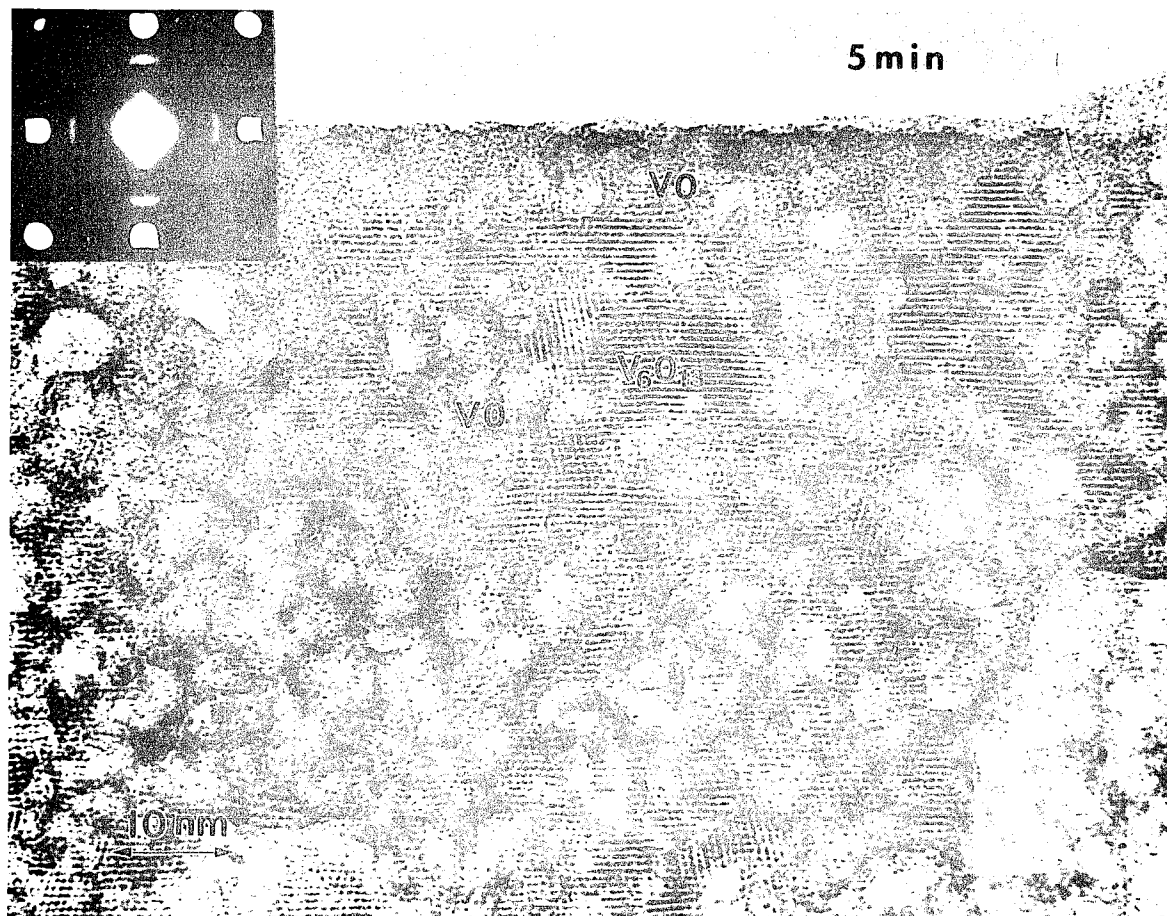
Figure 4.17 HREM image of V_2O_5 [001] taken as soon as a single crystal of V_2O_5 was tilted to the zone axis shows the formation of VO at the surface and an inhomogeneous mixture of V_6O_{13} and VO in the bulk. The flux was 5.0 A/cm^2 (Courtesy of H.-J. Fan).
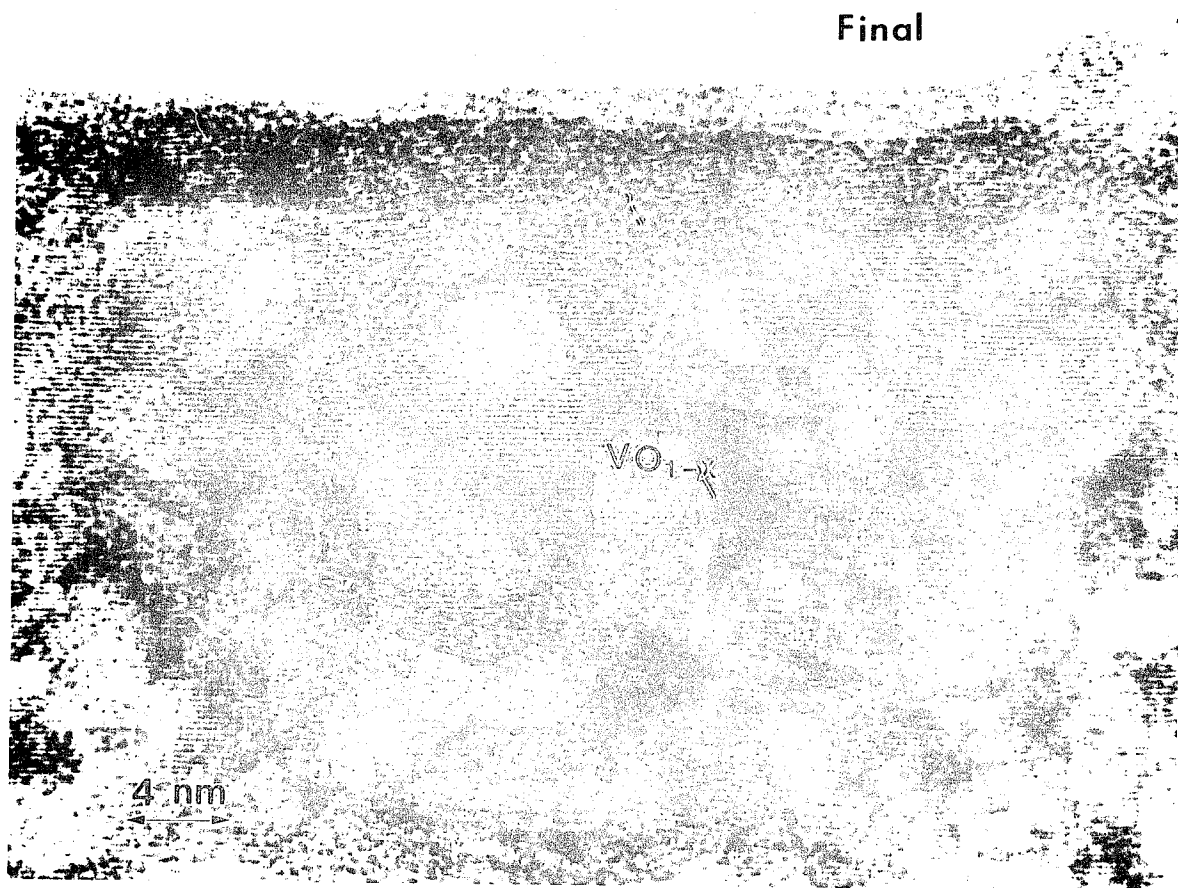
Figure 4.18   HREM image of V_2O_5 [001] taken after 60 min electron irradiation at a flux of 5.0 A/cm^2. The final stable phase is VO (Courtesy of H.- J. Fan).

domain size and the electron flux were closely related. As shown in Figure 4.19, the

average grain size of VO was inversely proportional to the square root of the flux as

$$D = \frac{C}{\sqrt{F}}$$ (4.1)

where D is the average domain size, F is the flux and C is a constant. This equation

suggests that the homogeneous nucleation rate of VO depend on the electron beam flux.

For homogeneous nucleation, the nucleation rate is given by

(4.2)

$$N_{hom} = fC^*$$

where C^* is the concentration of the critical-sized nuclei and f is the rate at which each

nucleus is made supercritical, which depends on the surface area of the nucleus and the

rate at which diffusion can occur. It can be therefore concluded that at the higher flux,

electron irradiation enhanced the diffusion rate, resulting in an increase of f.

Consequently the nucleation rate is enhanced, leading to the smaller domain size at the

higher flux. This observation provides an indirect evidence for electron-assisted diffusion.

Table 4.9 summarizes the time evolution of the phase transformation of V_2O_5 under

electron irradiation at a flux of 5.0 A/cm^2.
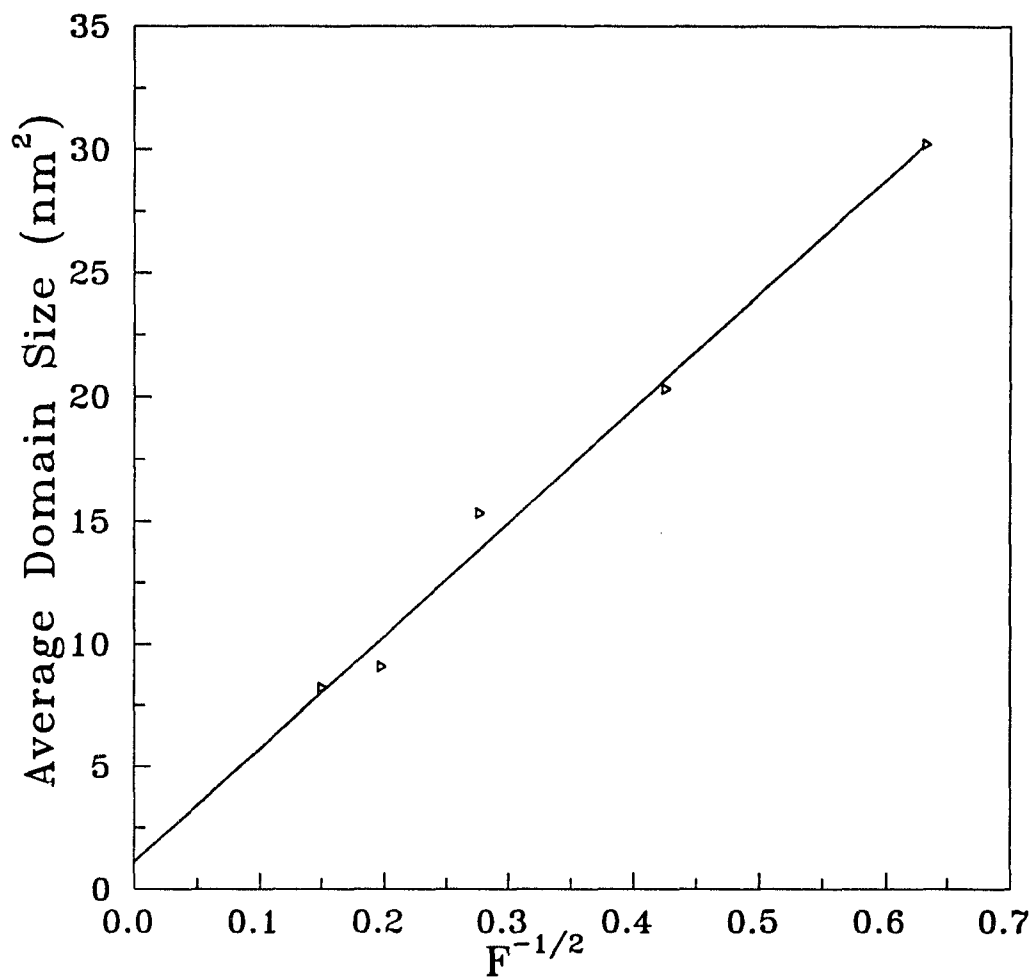
Figure 4.19   Dependence of the average domain size of VO on the electron flux
(Courtesy of H.-J. Fan).
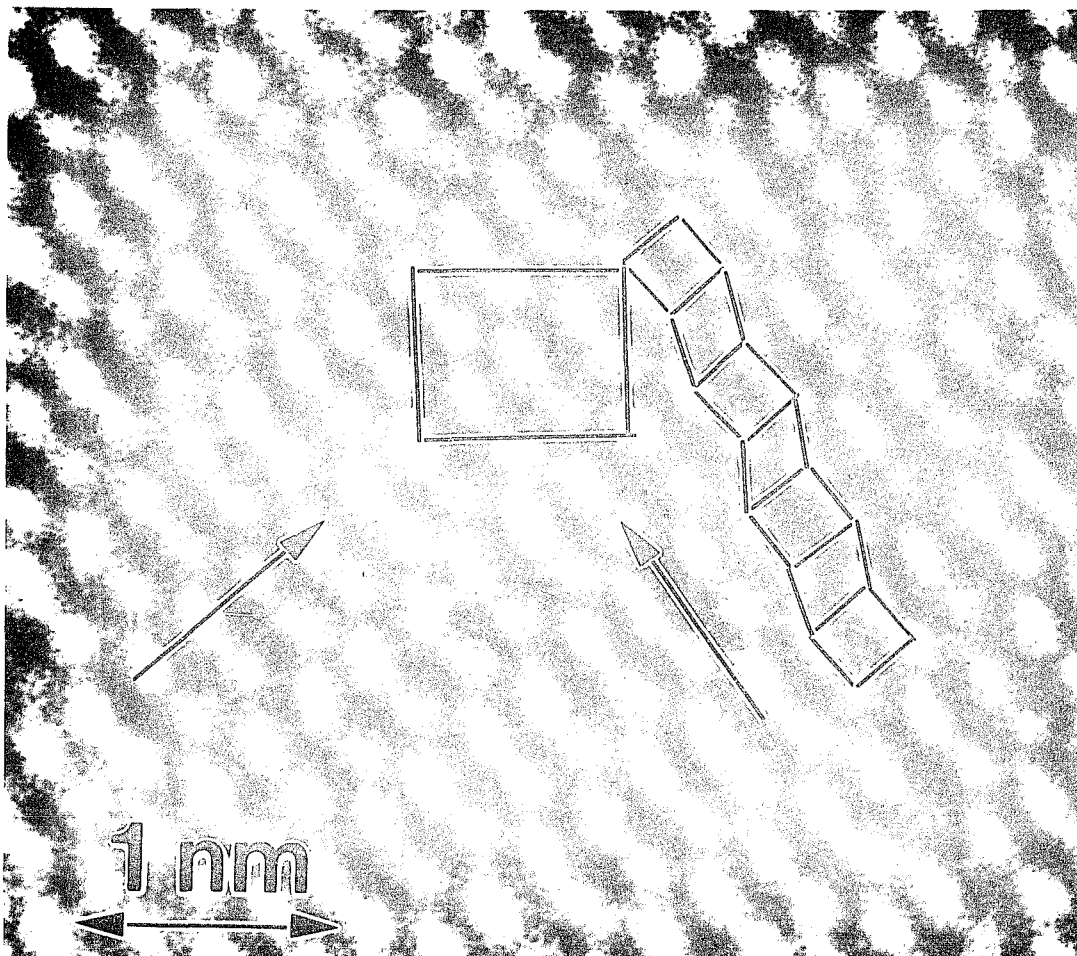
Figure 4.20   HREM image of V_4O_9 with the unit cell marked.

TABLE 4.9 Summary of phase transformation in V_2O_5

Electron Energy = 300 keV, Flux = 5.0 A/cm^2, Vacuum = 3 × 10^{-7} torr

Time	Phases Observed
Initial (5 min)	VO (surface)
	Inhomogeneous mixture of VO and β-V_6O_{13} (bulk)
Final (60 min)	Small domains of VO

HREM Image Simulation of V_4O_9

It is commonly accepted that V_4O_9 has an orthorhombic structure with a = 8.23 Å, b = 10.32 Å and c = 16.47 Å. However, the detailed atomic arrangement of the structure is still unknown. Experimentally, it is difficult to grow a large V_4O_9 single crystal for conventional x-ray diffraction to deduce the atomic coordinations. In this thesis work, HREM images were compared to multislice image simulations for different models of V_4O_9.

Figure 4.20 shows a HREM image of V_4O_9 with the unit cell marked. Two directions of periodicity indicated by arrows are most noticeable with the alternative arrangements of squares and quadrilaterals along [-110]. These features were used as fingerprints in the image simulation.

It has been pointed out in section 4.2.2 that there exists a large discrepancy between the Fiermans' model, the only structural model proposed for V_4O_9, and the experimental observation. Nevertheless the Fiermans' model provides a starting point for the simulation. Based on this model, six structural models for the multislice image simulation

were proposed and summarized in Table 4.10.

TABLE 4.10 Summary of the Structural Models

	Comp.	Stru.	P. Occu.	O. Vac.	Chann.	Match
A	V_2O_5	m-V_4O_9	. No	No	No	No
B	V_4O_9	m-V_4O_9	Yes	No	No	No
C	V_4O_9	V_4O_9	No	Yes	No	No
D	V_2O_5	m-V_4O_9	No	No	Yes	Yes
E	V_4O_9	m-V_4O_9	Yes	No	Yes	Yes
F	V_4O_9	V_4O_9	No	Yes	Yes	Yes

Note: Comp. = composition, Stru. = structure, P. Occu. = partial occupancy
  O. Vac. = Oxygen Vacancy, Chann. = channel.

Shown in Figure 4.21 is the orthorhombic structure projected on the c-plane, extracted from the structure of V_2O_5. Comparing Figure 4.21 with Figure 4.20, it is noted that Figure 4.21 does not have the alternating arrangement of squares and quadrilaterals along [-110]. In light of this consideration, atoms in every other (-110) plane were shifted in the direction indicated by the arrow to give rise to the structural model "A" shown in Figure 4.22. In this structure the lattice parameter along the c-direction is 4.37 Å, the same as V_2O_5, but different from V_4O_9 which has a spacing of 16.47 Å. For the purpose of identification, this structure is called m-V_4O_9. One way to achieve V_4O_9 stoichiometry is to introduce a partial occupancy of oxygen atoms on every other (-110) plane in the structural model "A", resulting in the structural model "B" which has the structure of m-V_4O_9. An alternative way is to remove one out of every ten oxygen atoms
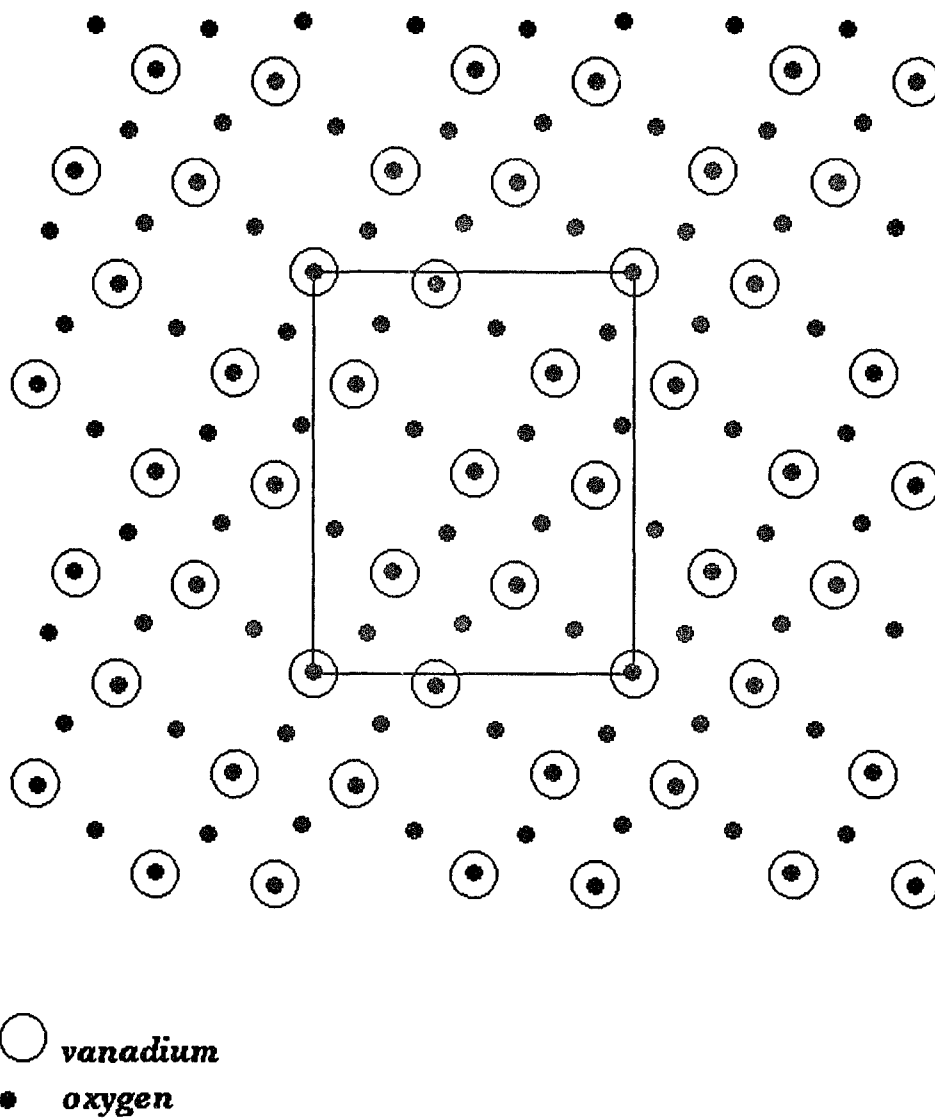
Figure 4.21 Projection of V_4O_9 extracted from V_2O_5 on c-plane.

vanadium

oxygen
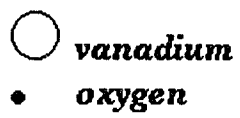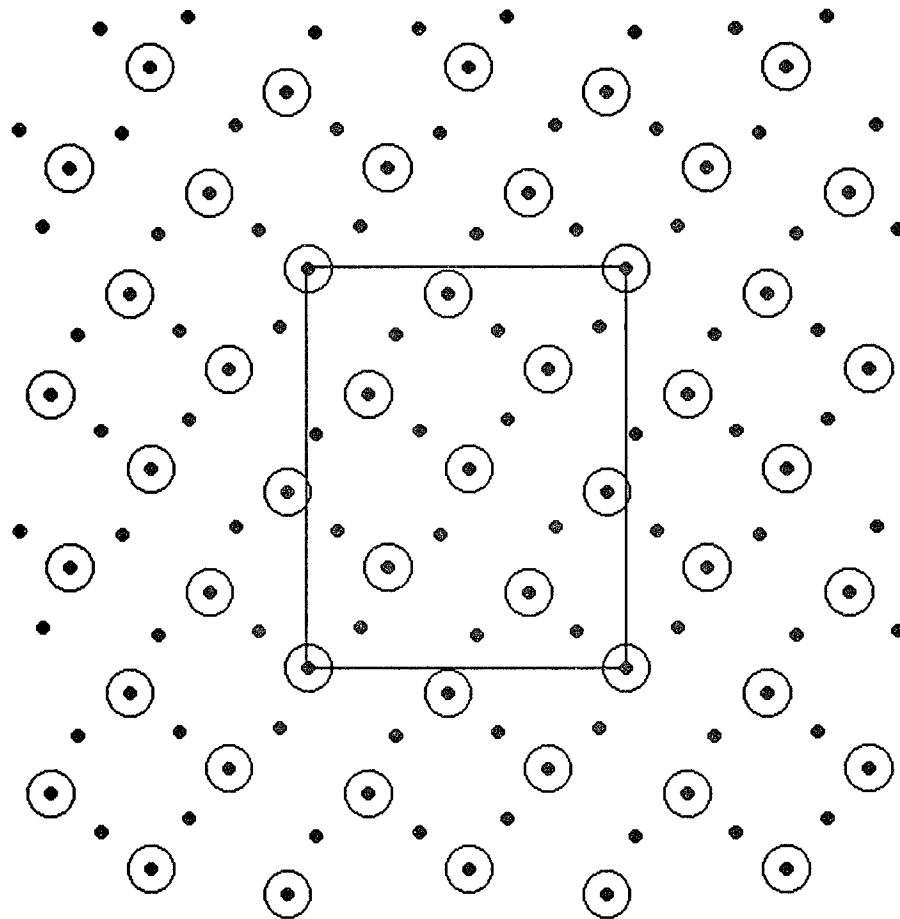
Figure 4.22   Structural model "A".

at the positions proposed by Fiermans (See Figure 4.6 and 4.7), giving rise to the

structural model "C", in which the has the c-lattice parameter of 16.47 Å. Figures 4.23,

4.24 and 4.25 show the image simulations of these three structural models with unit cell

marked. First, it can be noted that the image simulations are not sensitive to the oxygen

vacancies and partial occupancy, especially in the thin area. This is a commonly known

limitation of HREM, i.e. HREM images only provide two dimensional information and

is insensitive to the structural information in the beam direction. The second point is that

these simulations exhibit only one direction of periodicity indicated by arrows, but lack

the periodicity along the other diagonal direction of the unit cell. These simulations did

not match the experimental images.

Another approach to simulating the experimental images involves the previous steps

plus generating periodicity along [-110] in the simulation. Oxygen atoms on every other

(-110) planes were shifted to the corresponding positions indicated by arrows in Figure

4.26, resulting in the structural model "D" which has a channel on every other (-110)

plane. Partial occupancy at these oxygen sites was introduced to obtain the V_4O_9

stoichiometry, yielding the structural model "E". The structural model "F" was obtained

by removing oxygen atoms at the positions proposed by Fiermans. Shown in Figures

4.27, 4.28 and 4.29 are the image simulations of "D", "E" and "F", demonstrating again

the insensitivity of the image simulation to the partial occupancy and oxygen vacancies.

In comparing these two sets of image simulations, it is noted that the second set of the

simulations exhibit periodicities along both diagonal directions: [110] and [-110], which

matches the experimental observations. A through focus match between the second set
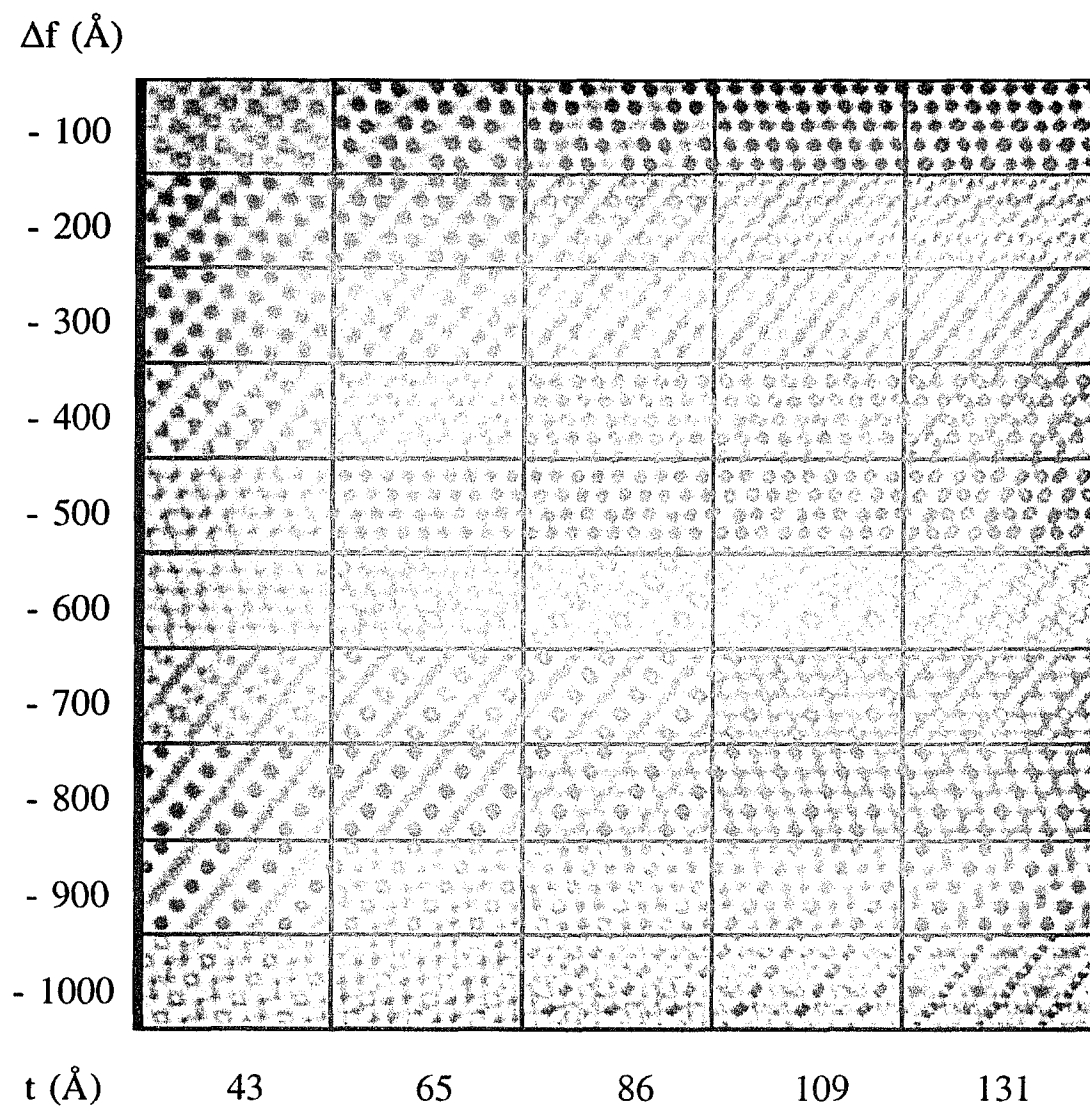
Figure 4.23   HREM image simulation of "A"

Δf (Å)

- 100

- 200

- 300

- 400

- 500

- 600

- 700

- 800

- 900

- 1000

t (Å)   43   65   86   109   131
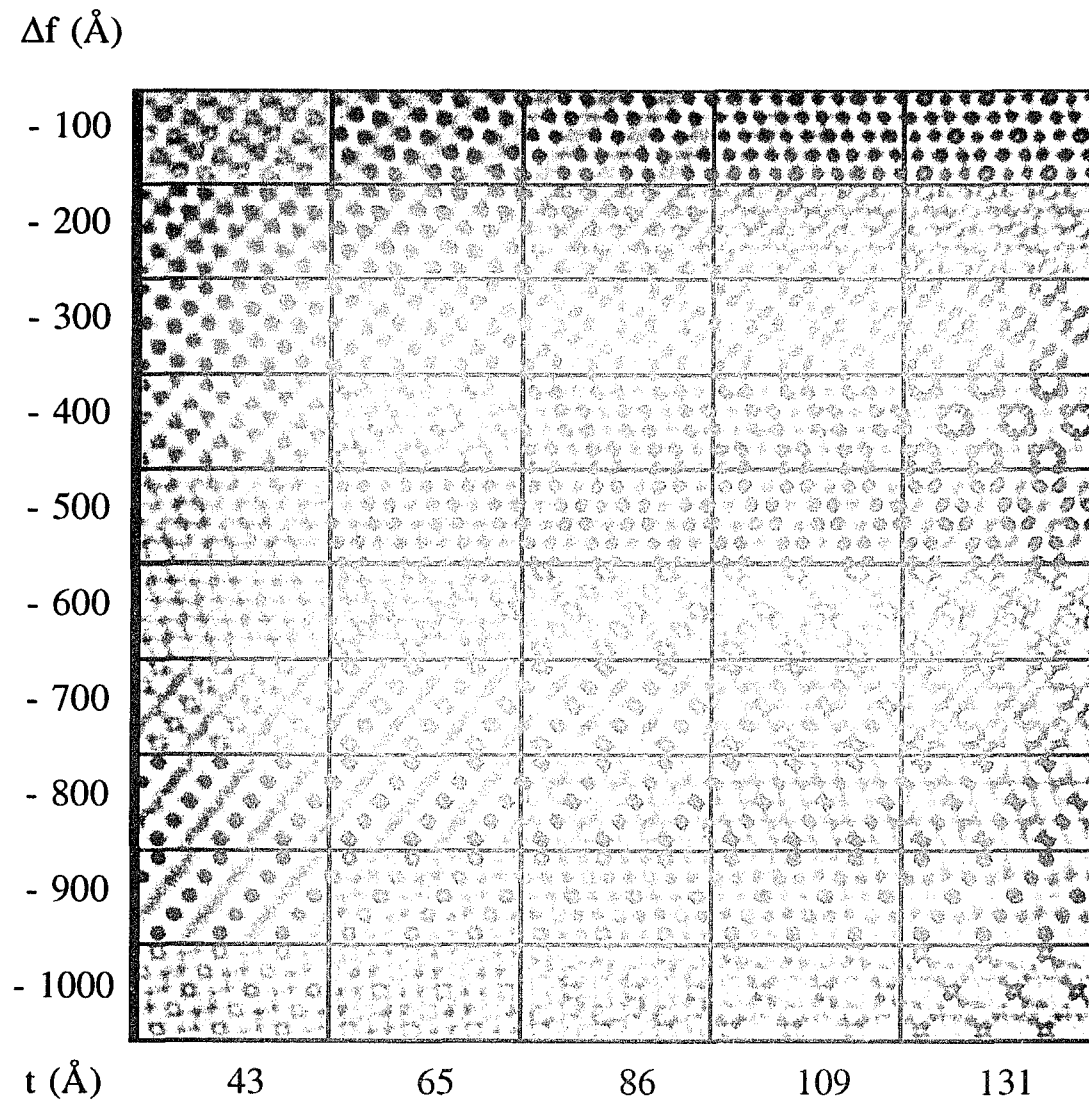
Figure 4.24   HREM image simulation of "B".

Δf (Å)
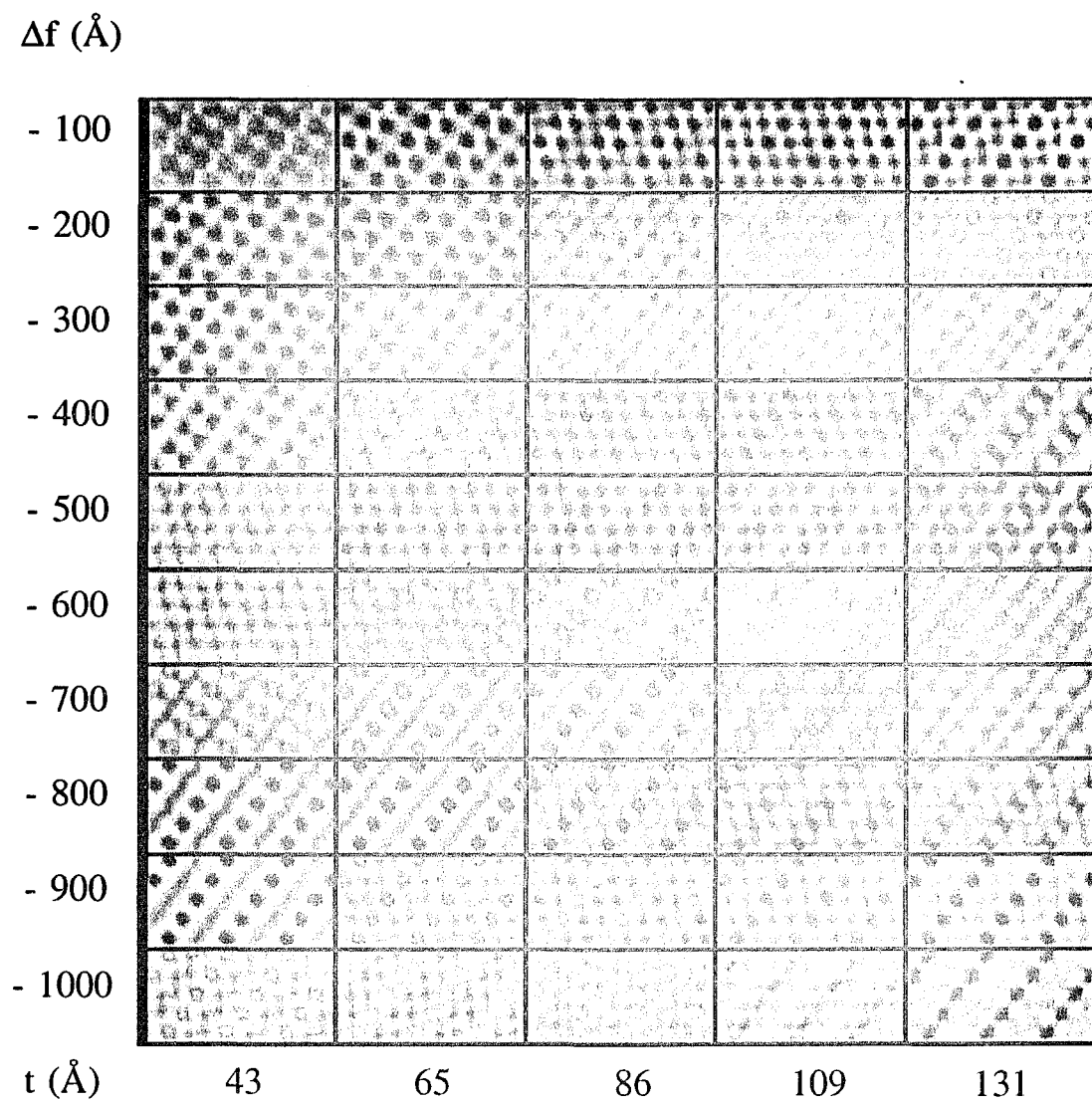
Figure 4.25   HREM image simulation of "C".

○ *vanadium*

● *oxygen*
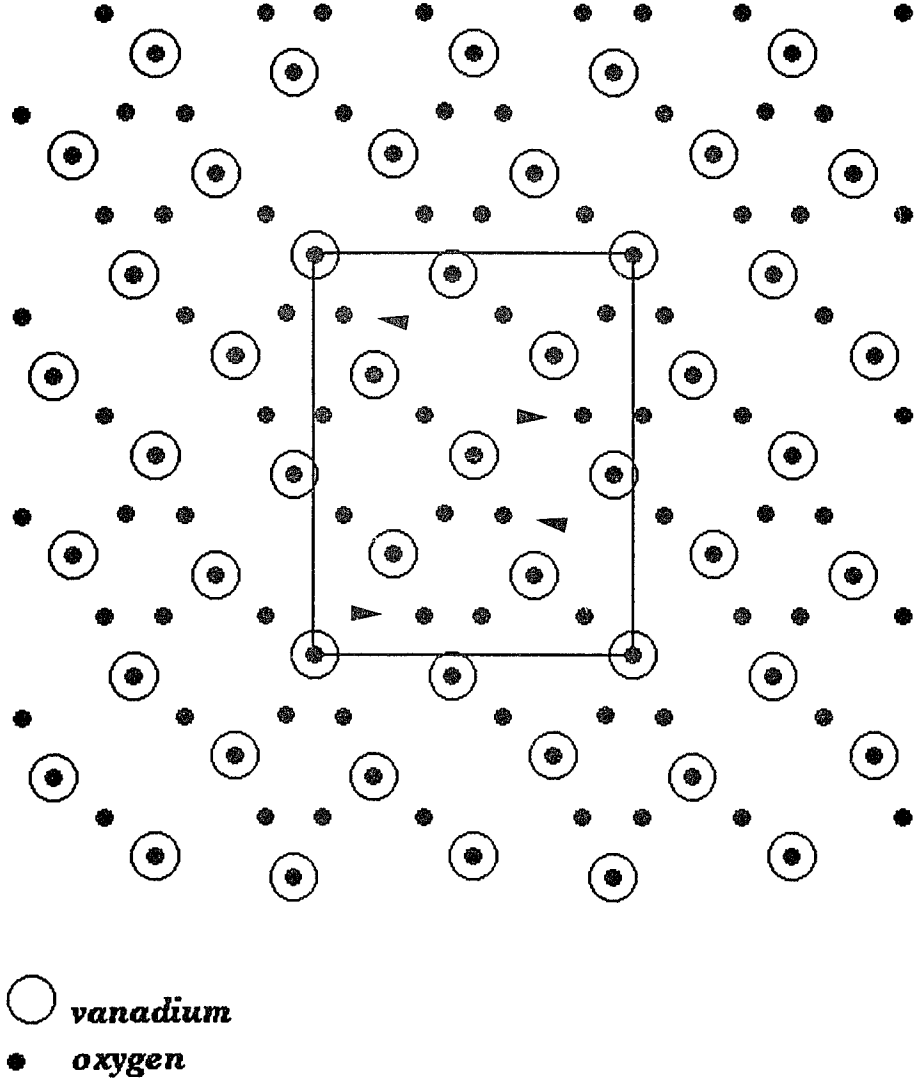
Figure 4.26   Structural model "D" with channels on every other (-110) plane.

$\Delta f\ (\text{Å})$
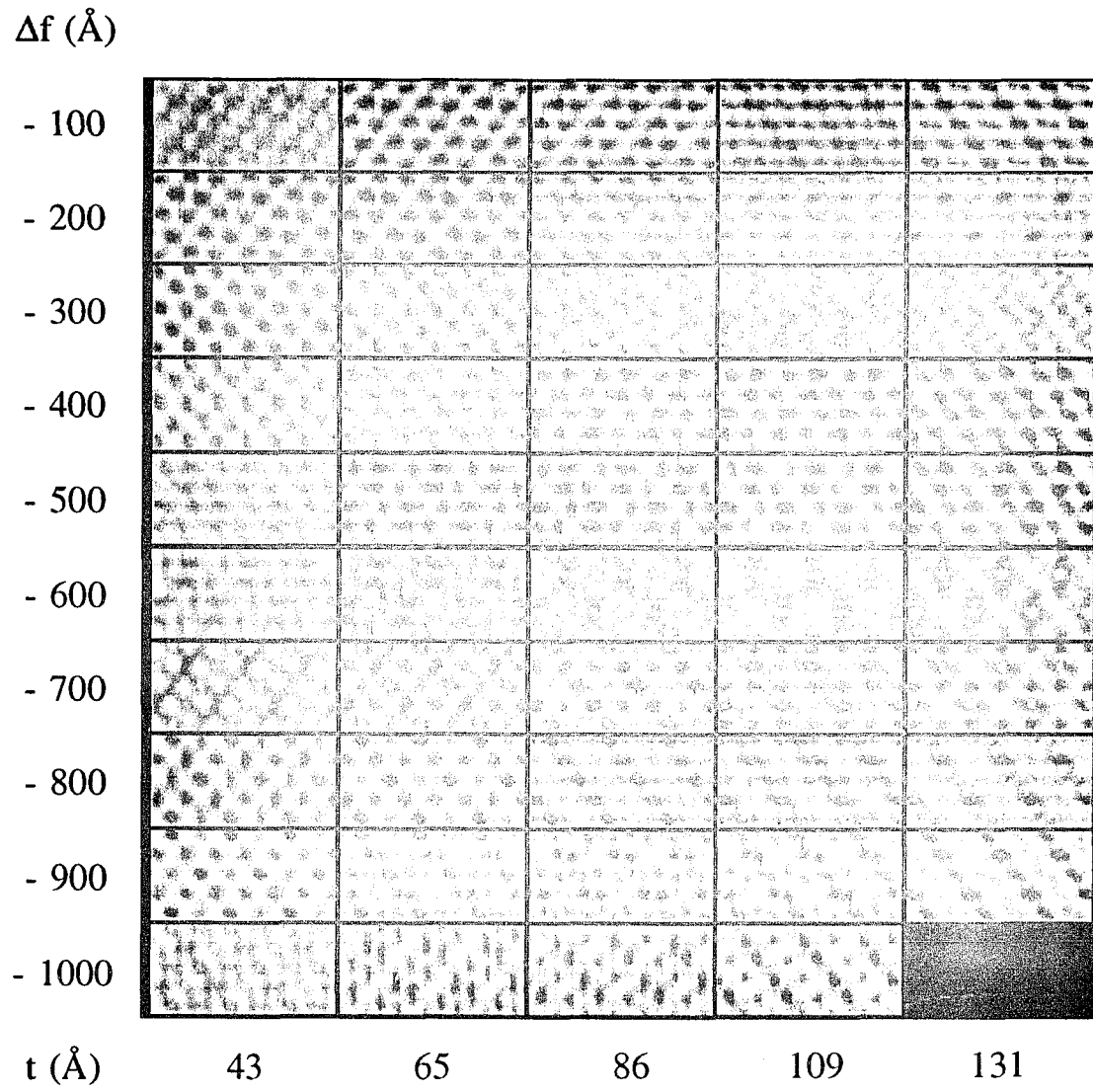
Figure 4.27   HREM image simulation of "D".

Δf (Å)

- 100

- 200

- 300

- 400

- 500

- 600

- 700

- 800

- 900

- 1000

t (Å)   43   65   86   109   131
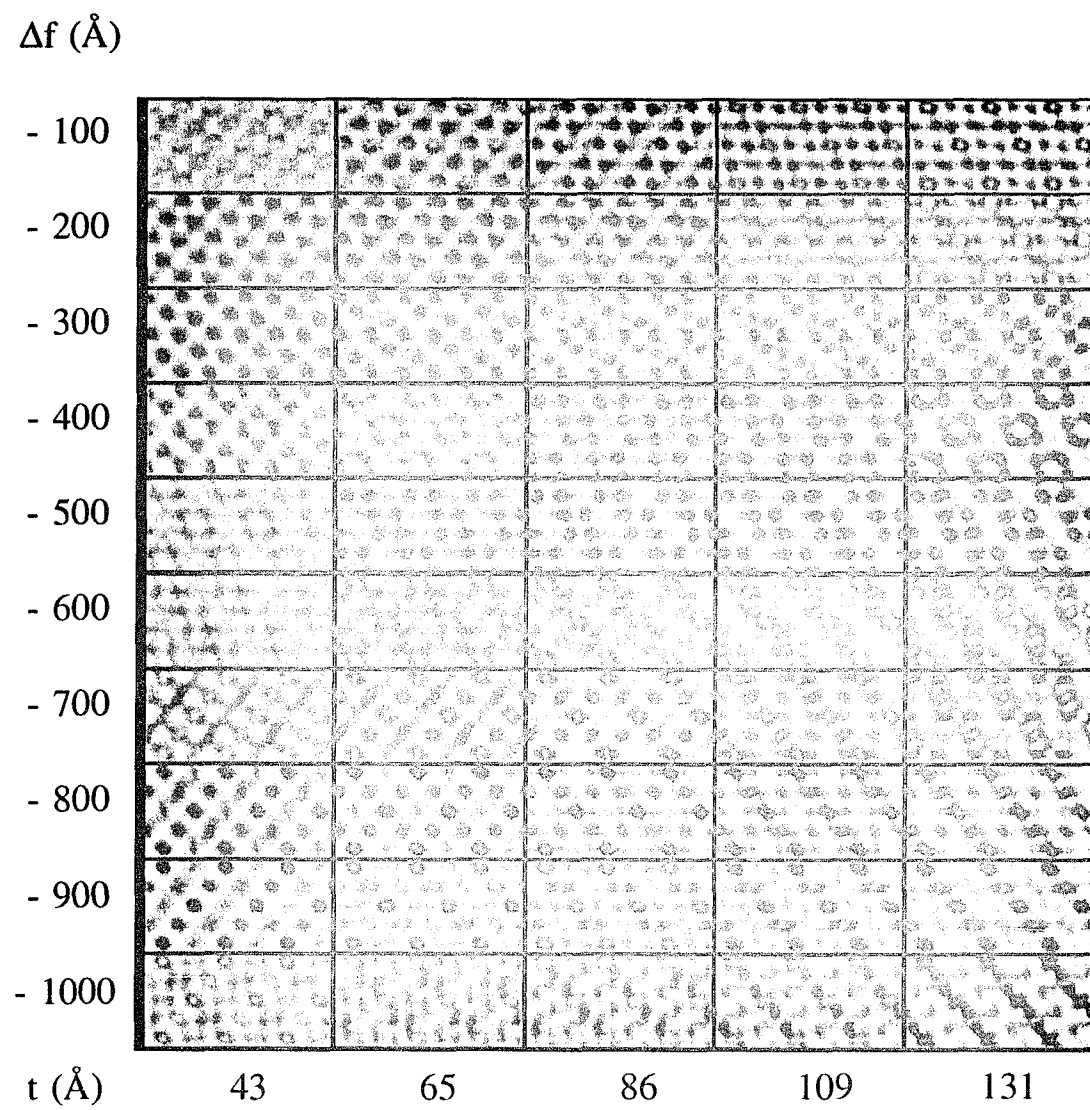
Figure 4.28   HREM image simulation of "E".

Δf (Å)

- 100

- 200

- 300

- 400

- 500

- 600

- 700

- 800

- 900

- 1000

t (Å)   43   65   86   109   131
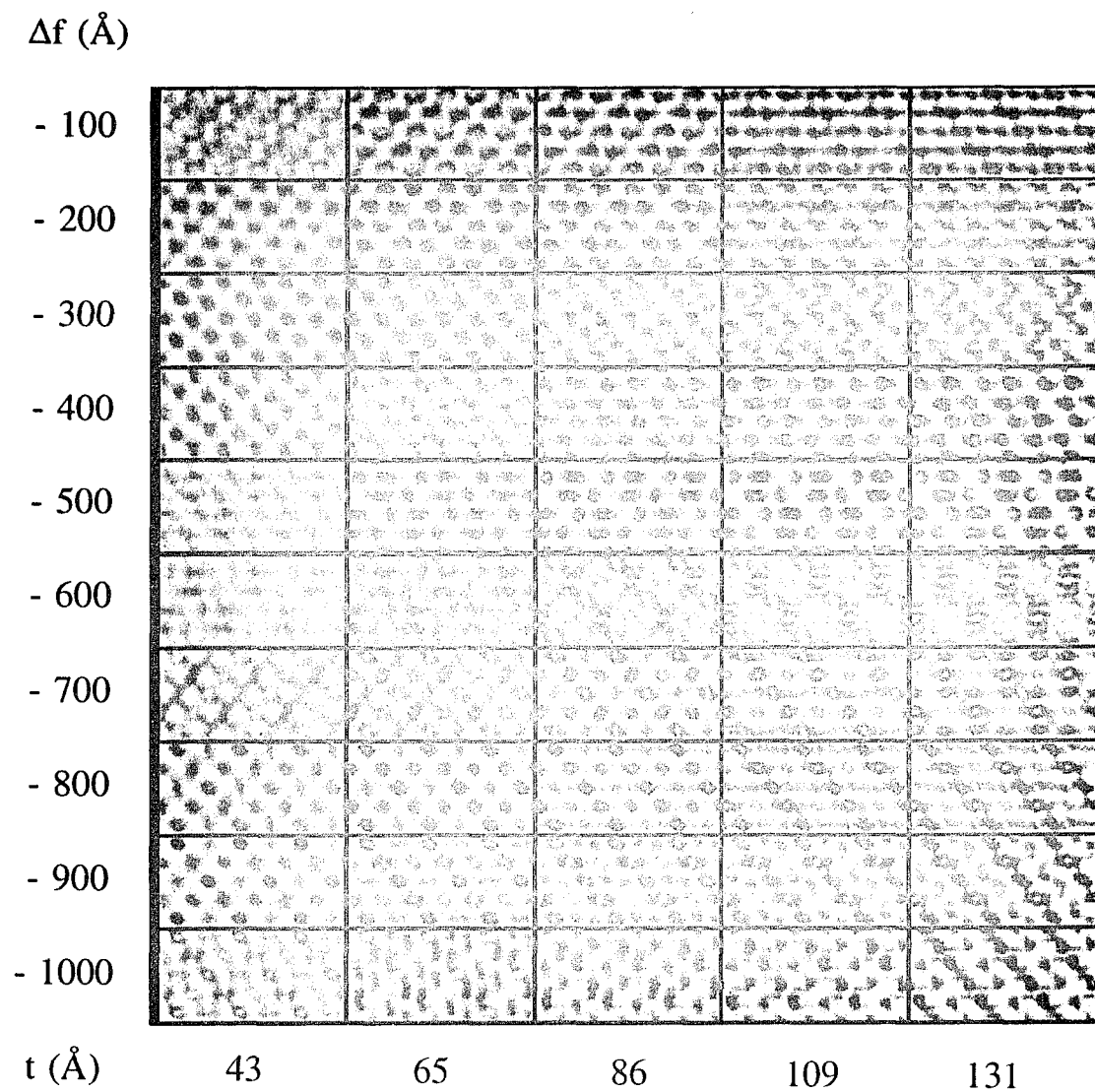
Figure 4.29   HREM image simulation of "F".

of the image simulations with experimental images are shown in Figure 4.30.

The image simulations presented above identify the atomic positions of vanadium atoms and the channels in the structure of V_4O_9. This provides a physical picture for the phase transformation of V_2O_5 to V_4O_9. Electron irradiation preferentially breaks the $V-O_2$ bonds (See Figure 4.2) in V_2O_5. The vanadium lattice then rearranges into a structure shown in Figure 4.27, driven by the repulsive force between the oxygen vacancies or between the oxygen vacancies and vanadium atoms. This interpretation is supported by the structural analysis present in section 4.1.1. The $V-O_2$ bond is the weak bond in the V_2O_5 structure, resulting from the strong repulsive force between the O^2 atoms. It is thus expected that these bonds could be preferentially broken by electron irradiation. This conclusion does not agree with the Fierman's model, in which the $O-V_1$ bonds (See Figure 4.2) are broken. It should be noted, however, the image simulation is not sensitive enough in this case to unambiguously differentiate structural models "D", "E" and "F" in order to identify the atomic positions of all the oxygen atoms.

[101]

The orientational dependence of the damage effect is commonly observed in transition metal oxides such as TiO_2 (Strane 1989), NiO (Buckett 1990) and is believed to be related to the anisotropy of the crystal structure. Studies along other orientations suggest that the phase transformation in V_2O_5 was orientation dependent. Shown in Figure 4.31 is a HREM image taken from a crystalline particle along [101] after about 15 min of electron irradiation at a flux of 2.0 A/cm^2. A short range disorder structure

Δf (Å)

- 160

- 440

- 750
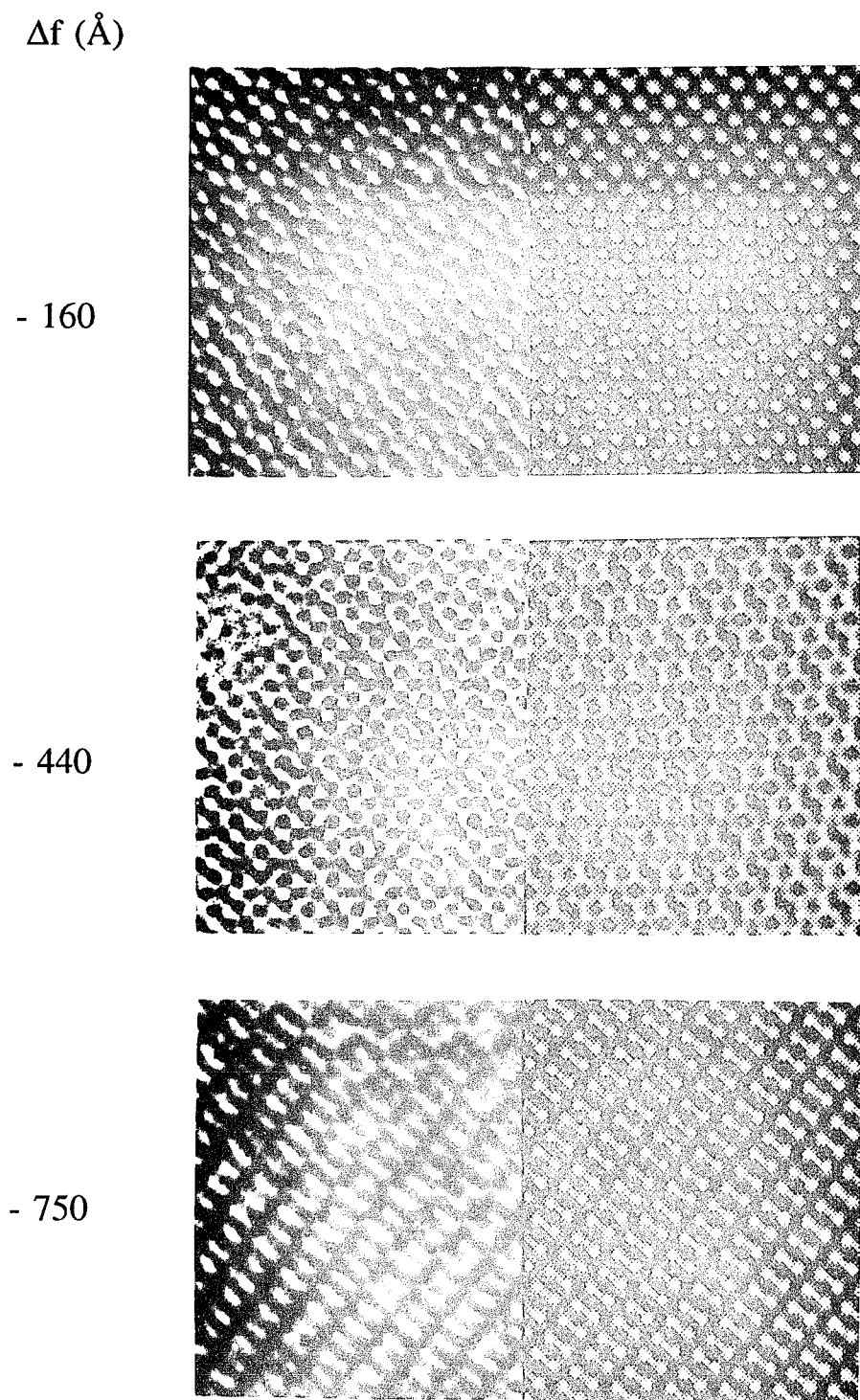
Figure 4.30 HREM images of V_4O_9 with the best fit calculated images.
Thickness = 43 Å.

10min
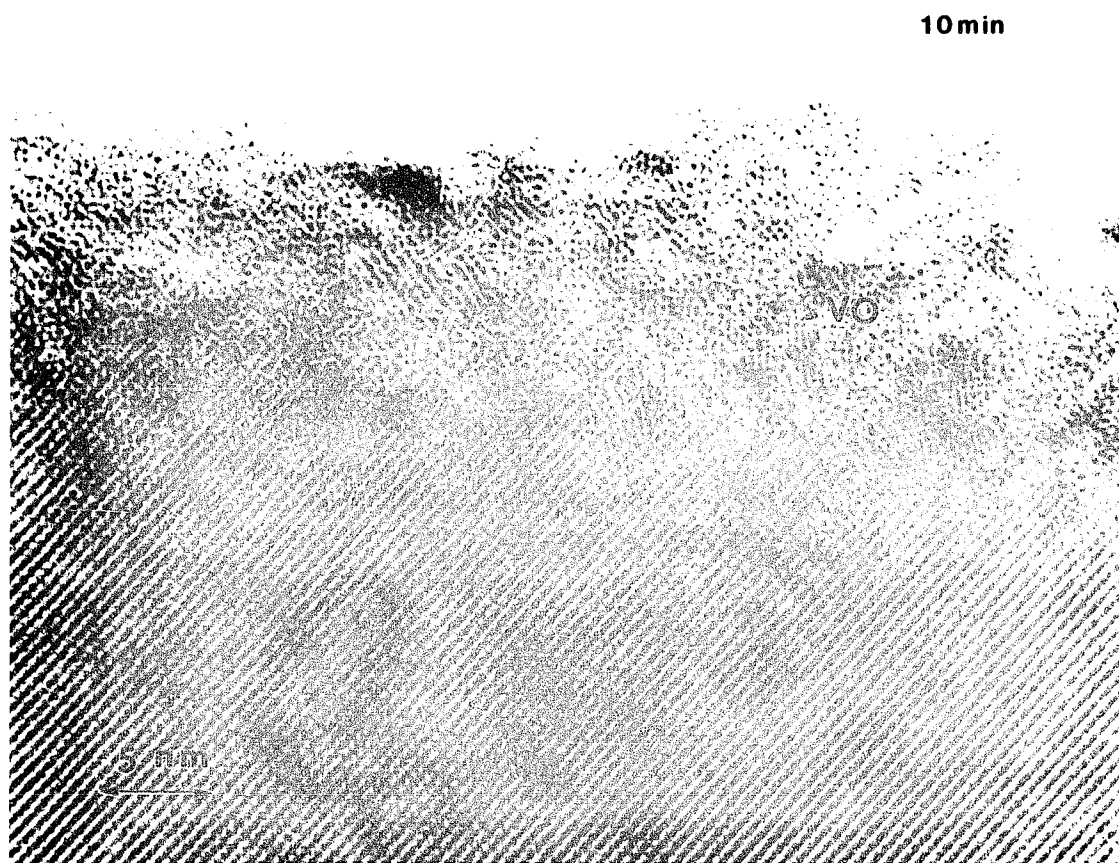
Figure 4.31   HREM image of V_2O_5 [101], showing VO crystallites and short range order structures formed at the surface (Courtesy of H.-J. Fan)

inbed with small crystallites of VO [101] was found at the surface. The size of the VO

crystallite was about 200 Å^2 indicated by arrows. V_6O_{13} and V_4O_9, were not observed

under any flux conditions along this orientation. This reason for this observation is not

clear. It could be that the orientation relationships of V_4O_9 and V_6O_{13} to V_2O_5 could not

be satisfied along this orientation.

UHV

To evaluate the effect of the ambient pressure to the damage behavior, similar

experiments were repeated in the UHV environment of the Hitachi UHV H-9000 electron

microscope. Samples were baked in the specimen preparation chamber at about 150°C

for twenty four hours before being loading into the microscope. By visual examination,

these samples were found to have a cleaner surface. In UHV the same phase

transformation was observed under the same flux condition. Figure 4.32 showed a

typical HREM image taken in UHV after about 10 min electron irradiation at a flux of

about 1.0 A/cm^2. In this image, the three new phases, V_4O_9, V_6O_{13} and VO, can be

clearly seen. This observation ruled out the possibility of surface reaction of V_2O_5 with

gaseous species in the vacuum.

Knock-On Effect

In many cases, the knock-on effect may be operative and have significant

contribution to the damage process under high energy electron irradiation (Buckett 1991).

One method to differentiate knock-on from electronic excitation is to lower the
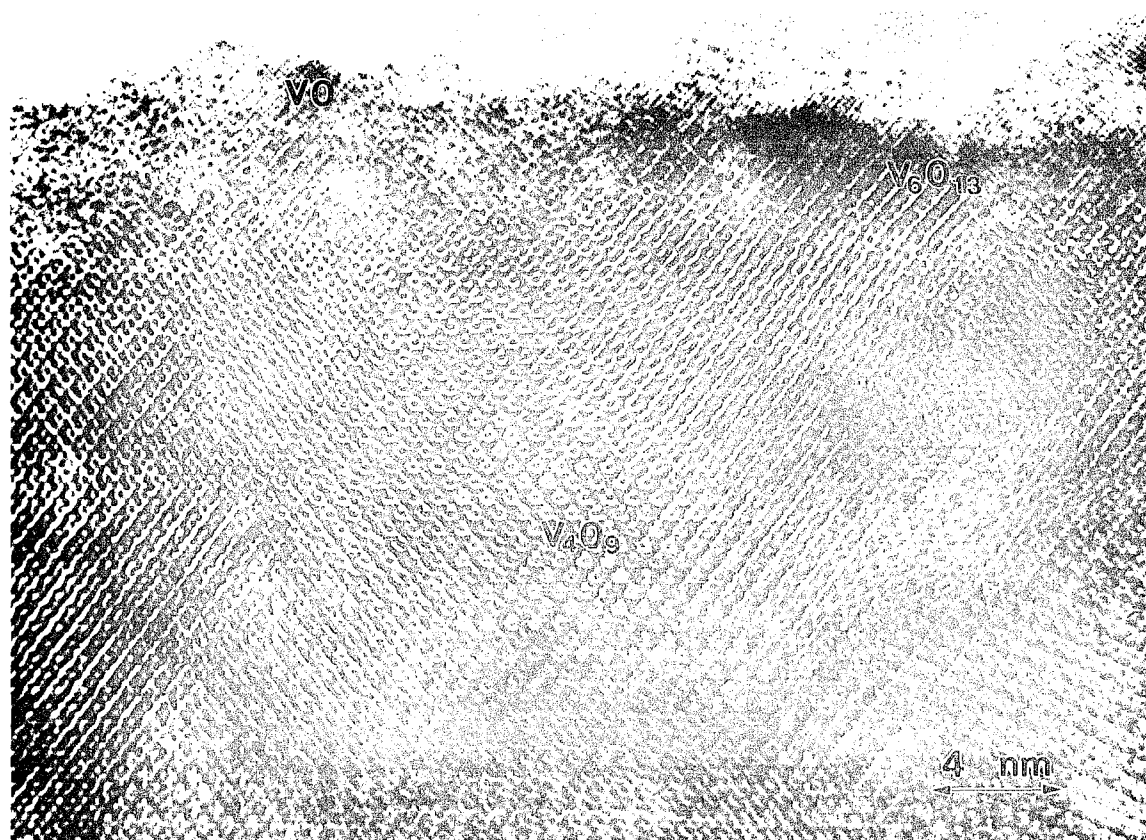
Figure 4.32 HREM image taken in UHV after 10 min electron irradiation at a flux of
1.0 A/cm^2 shows the same phase transformation occurred in non-UHV.
Three new phases, V_4O_9, β-V_6O_{13} and VO, can be clearly identified.

accelerating voltage below the knock-on threshold energy. The knock-on thresholdenergies for oxides are materials dependent and usually on the order of a few hundred keV for highly ionic solids. For most oxides, the knock-on threshold energies have not been measured experimentally. However, methods of estimation were proposed (Hobbs 1979). Using the method proposed by Hobbs, Buckett (1991) estimated that the maximum threshold energy for displacement of a surface V^{5+} is about 2609 keV and 1288 keV for a surface O^{2-} in V_2O_5. According to this estimation, the knock-on damage should not operative under 300 keV electron irradiation. This was confirmed experimentally: no evidence of knock-on damage such as mass loss, erosion and sputtering were observed. It is therefore concluded that electronic excitation alone accounts for the phase transformations observed.

§4.4.2 Kinetics of the Phase Transformation

Experimental Observation

The kinetics of the phase transformation of V_2O_5 in the electron microscope were evaluated at various electron beam fluxes. The width of each phase was measured as a function of time. Measurements were repeated for different particles with different profile edges and thicknesses. The kinetics were found to be independent of the particle shape and thickness. Three flux regimes were investigated: low flux regime: flux < 1.5 A/cm^2; intermediated flux regime: $1.5 <$ flux < 1.9 A/cm^2 and high flux regime, flux > 1.9 A/cm^2.

The phase transformation routes were found to be flux dependent as presented in section 4.4.1. Three types of phase transformation were generally observed:

1) Low flux regime. In this regime, the route was V_2O_5 -> V_4O_9 -> β-V_6O_{13} -> VO (See Figure 4.13). The phase transformation was initiated at the surface and extended into the bulk. Both V_4O_9 and β-V_6O_{13} were metastable. They were present initially, but vanished with increasing radiation time.

2) Intermediate flux regime. In this regime, β-V_6O_{13} was not observed and the phase transformation route was V_2O_5 ->V_4O_9 -> VO (See Figure 4.16). The phase transformation was also surface initiated and extended into the bulk with a clear reaction front. Similar to the behavior in the low flux regime, V_4O_9 vanished with increasing radiation time.

3) High flux regime. In this flux regime, the phase transformation occurred concurrently both at the surface and in the bulk. At the surface, the phase transformation route was V_2O_5 -> VO (See Figure 4.17). In the bulk, V_2O_5 transformed into an inhomogeneous mixture of VO and β-V_6O_{13}.

Table 4.11 summarizes the flux dependent results.

TABLE 4.11 Summary of the flux dependent results

	Flux (A/cm^2)	Phase Transformation
Low Flux	< 1.5	V_2O_5 -> V_4O_9 -> β-V_6O_{13} -> VO
Intermediate Flux	1.5 - 1.9	V_2O_5 -> V_4O_9 -> VO
High Flux	> 1.9	V_2O_5 -> VO (Surface) mixture of VO and β-V_6O_{13} (Bulk)

To show the data on the kinetics of the phase transformation, we have chosen to plot

the widths of the different phases as a function of time. Five sets of data were shown in Figure 4.33 with the flux condition indicated. These plots show that the phase transformation is a very complex process. The data could not be simply fitted by either linear (interface controlled) or parabolic (diffusion controlled) functions. However some general points can be noted. In the low flux regime (See Figure 4.33a-b), the dominant initial phase was V_4O_9 with only small regions of β-V_6O_{13} and VO at the surface. With increasing irradiation time, V_4O_9 vanished rapidly, being consumed by β-V_6O_{13} and VO combined. The growth rates of β-V_6O_{13} and VO were initially slow, however increased rapidly as soon as V_4O_9 vanished, indicated by the increases in the widths of these two phases at the onset of the disappearance of the V_4O_9 phase. This effect can be more clearly seen in the plot of the growth rate of VO as a function of electron flux shown in Figure 4.34. The growth rate of VO was obtained by linearly fitting the kinetics curve of VO. The growth rates of VO in the low and intermediate flux regimes are very similar However there is a clear break between the low/intermediate flux regime and the high flux regime. Here it should be emphasized that in the low/intermediate flux regime of the growth rate of VO was obtained while V_4O_9 was present, whereas in the high flux regime, V_4O_9 was not. This implies that the growth rate of VO was limited by the presence of V_4O_9 and increases drastically as soon as V_4O_9 vanished.

Theoretical Modeling

To explain the kinetics data, a theoretical model for the phase transformation process as one dimensional diffusion problem with oxygen loss from the surface is proposed.
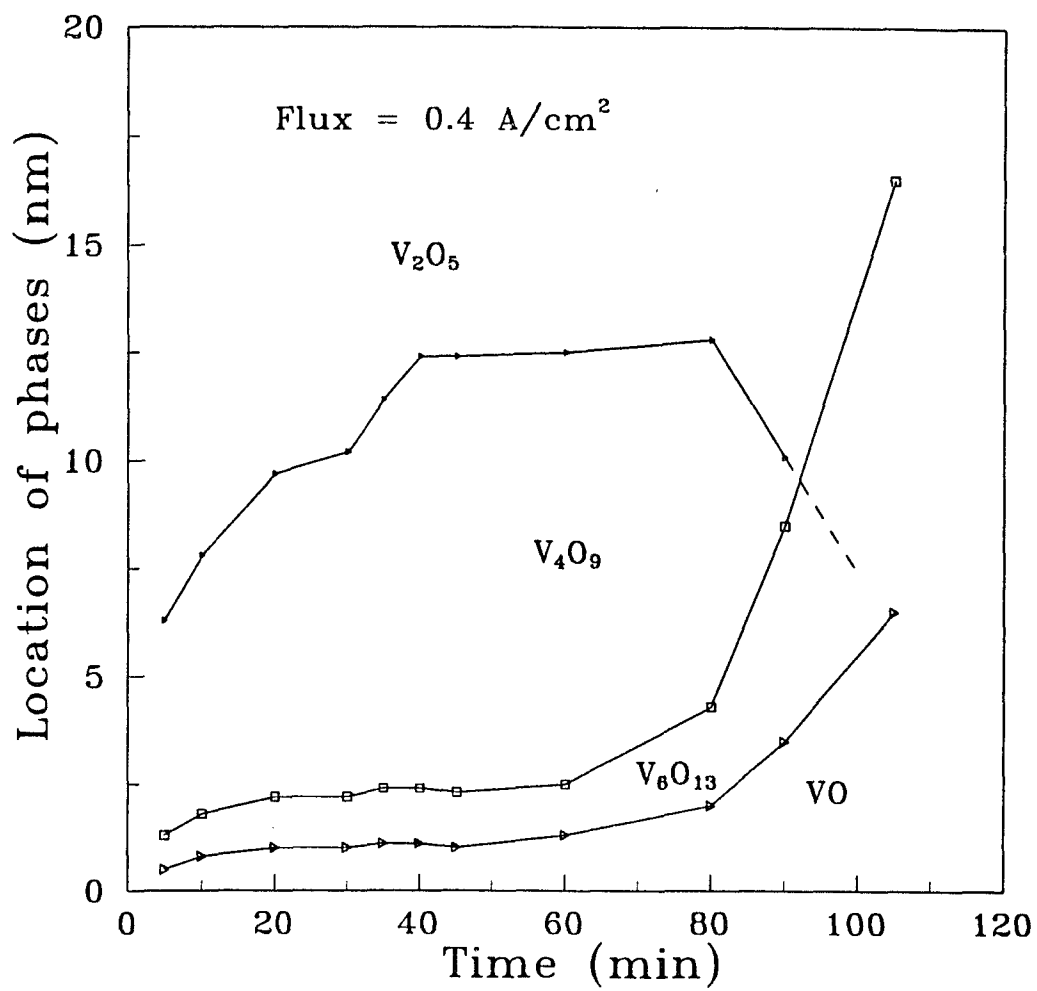
Figure 4.33   Kinetics of electron-induced phase transformation in V_2O_5.   (a) 0.4 A/cm²;   (b) 0.7 A/cm²;   (c) 1.8 A/cm²;   (d) 2.0 A/cm²;   (e) 5.0 A/cm² (Courtesy of H.-J. Fan).
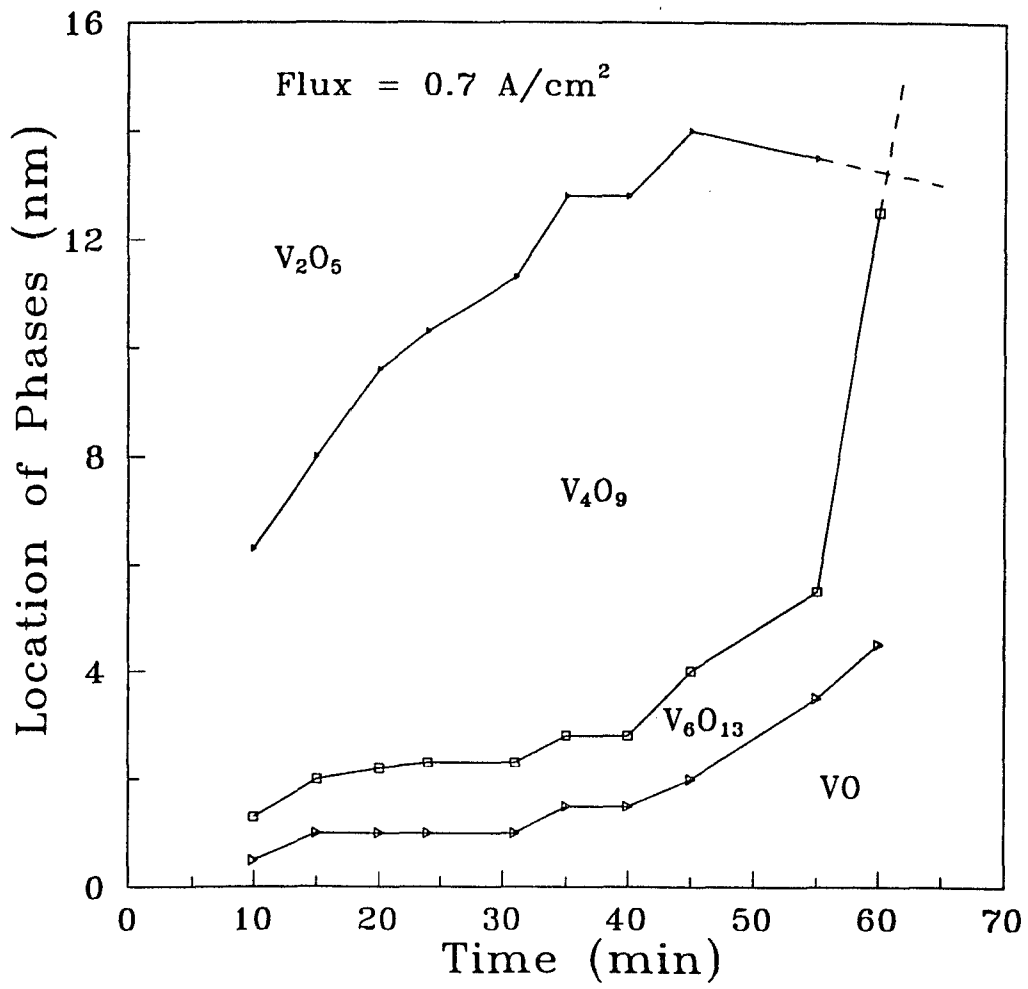
Figure 4.33 - Cont.
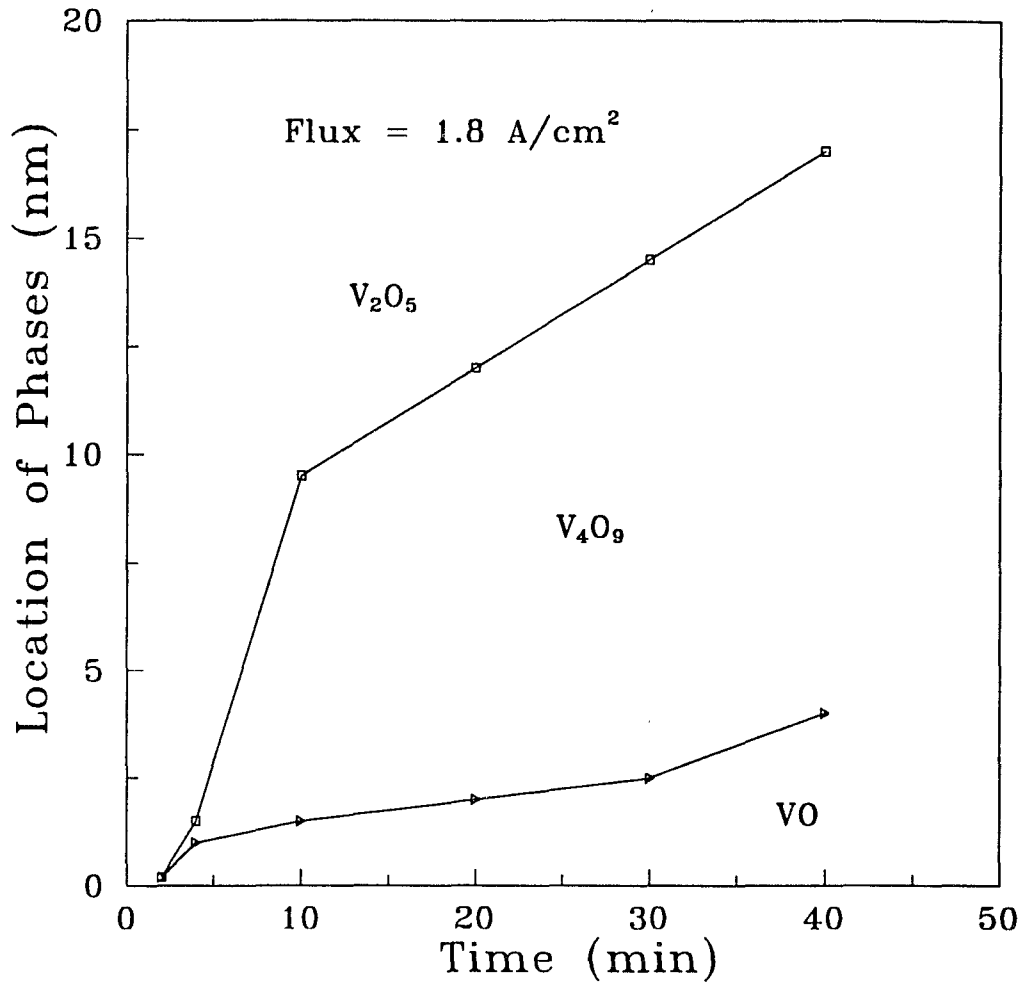
Figure 4.33 - Cont.
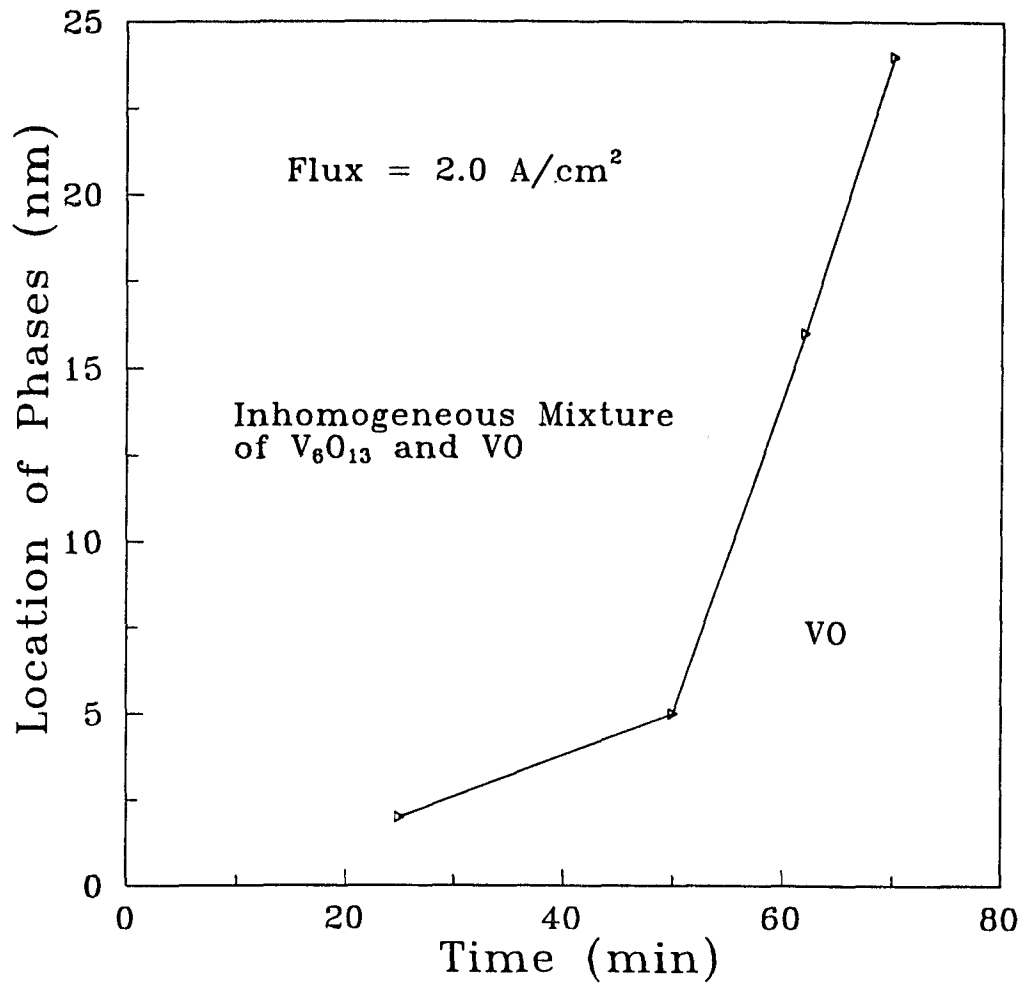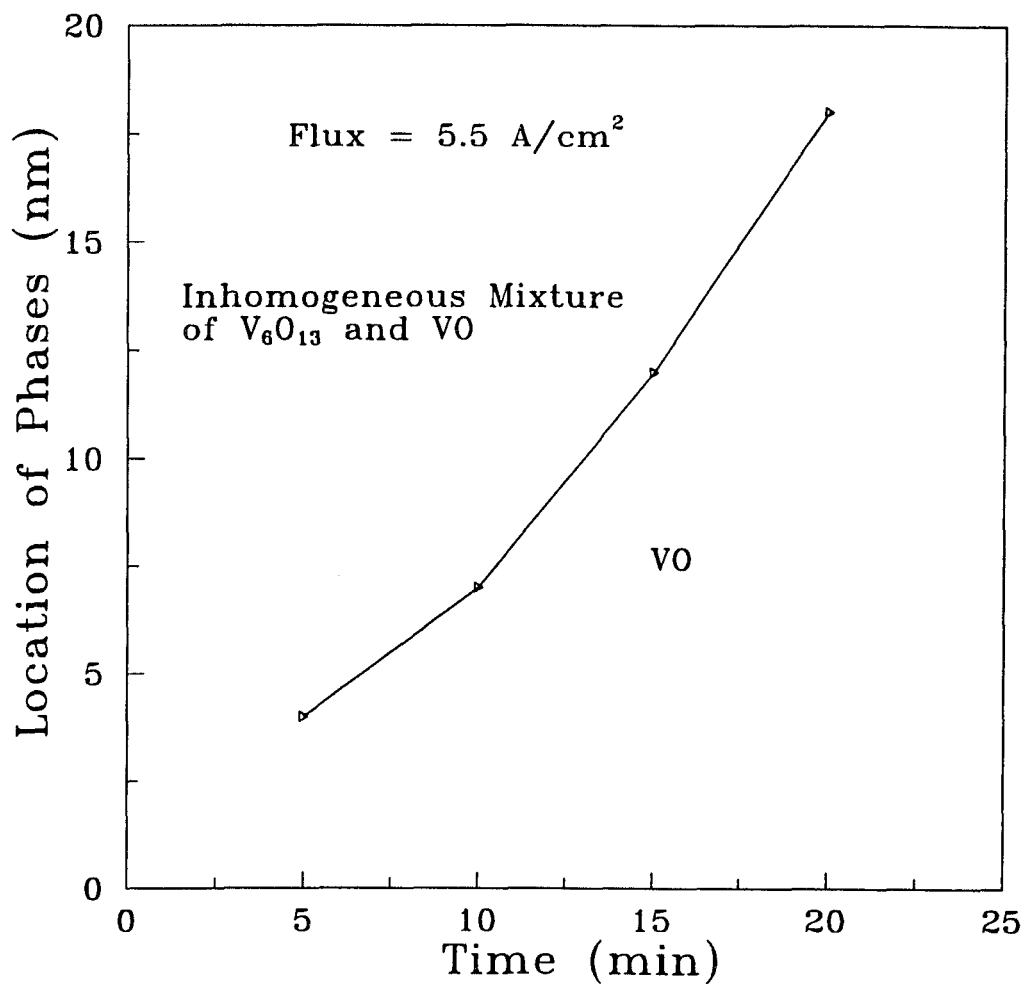
Figure 4.33 - Cont.

Figure 4.33 - Cont.
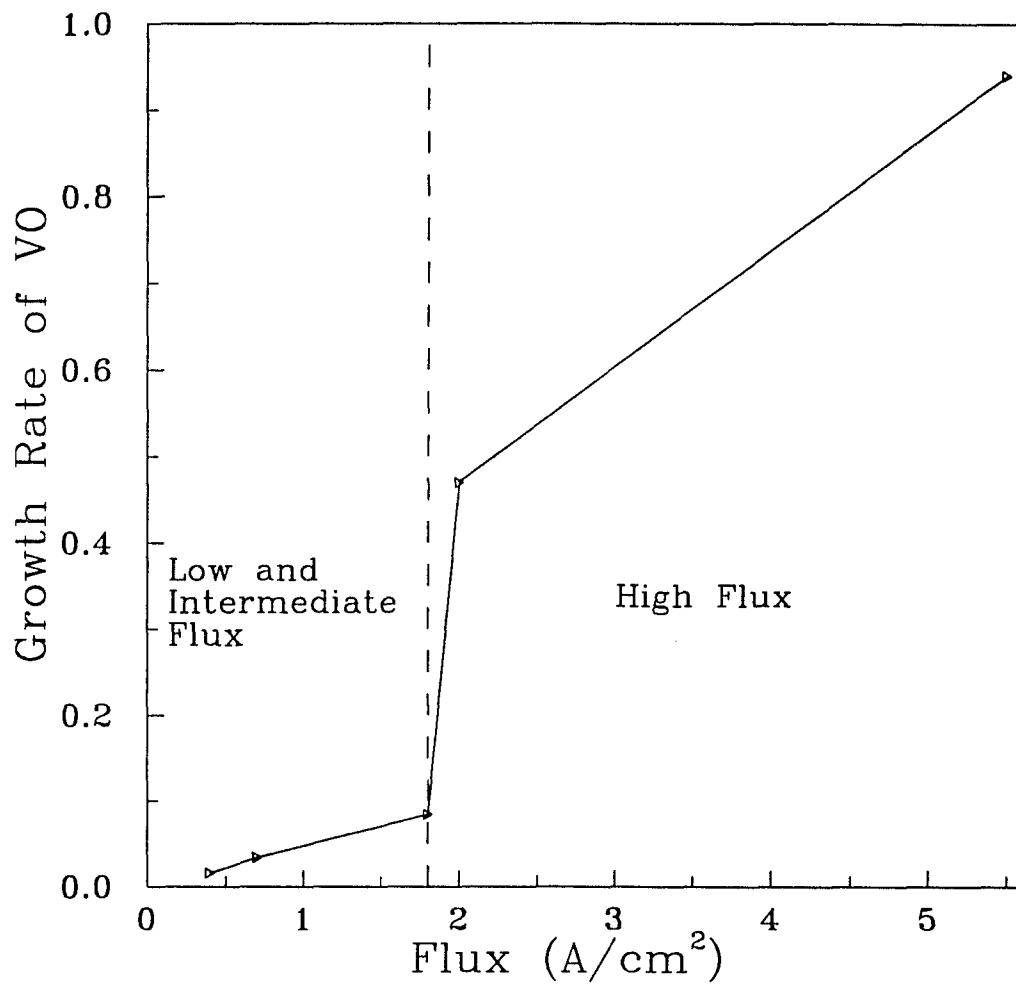
Figure 4.34   The growth rate of VO as a function of electron beam flux.

Before going into the detail description of the theoretical model, it is appropriate to point out some of the errors and complications in the interpretation of the experimental results. First, we have approximated the data in terms of straight fronts, whereas in reality the phase boundaries are not always flat, for example, see Figure 4.13. Second, the zeros of the time axis were slightly uncertain, since there was damage while tilting the specimen to the zone axis. Third, it should also be noted that the specimen is wedge shaped with the thickness slowly increasing away from the edge resulting in a two or three dimensional problem.

Figure 4.35 shows a schematic diagram of the physical process that takes place during electron irradiation. Electron irradiation in the direction perpendicular to the profile edge of the sample leads to a loss of oxygen from the sample. The loss of oxygen creates oxygen vacancies at the surface which diffuse into the bulk. At some level of oxygen deficiency, a phase transformation to a lower oxide takes place, and an interface appears and propagates into the bulk. This first phase transition can be followed by others.

Following this phase transformation, oxygen vacancies/interstitials can diffuse in both the parent and the new phases. The actual diffusion process itself may be purely thermal, or may be electron assisted.

A complete model including oxygen vacancies, interstitials, recombination and different diffusion constants along both different crystallographic directions and in different phases would be exceedingly complicated. The following assumptions are made to simplify the model.
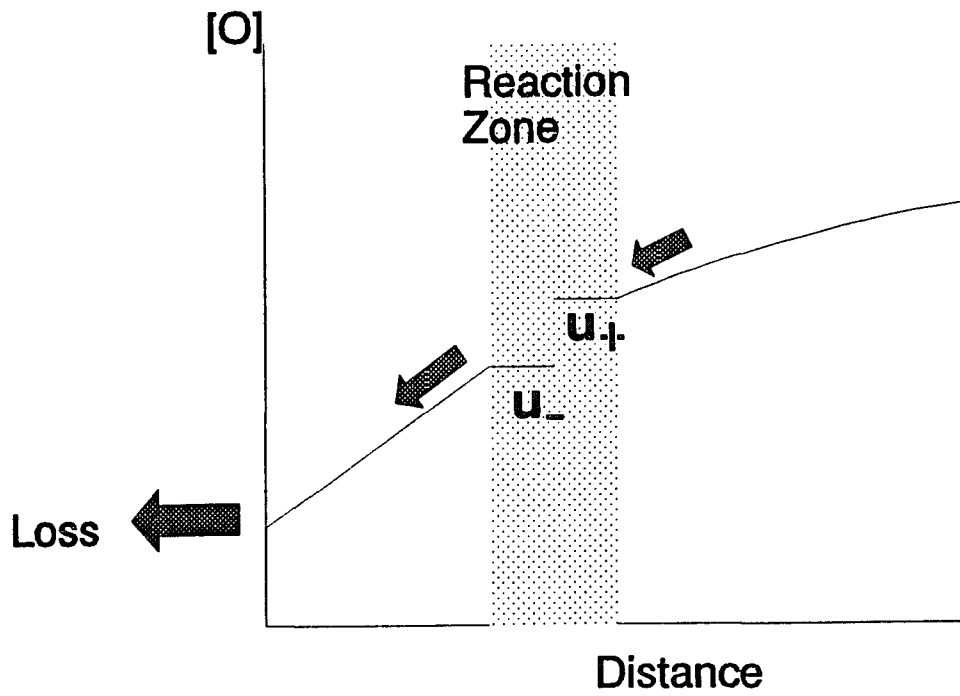
Figure 4.35   Schematic description of the physical process which take place during the experiment.

a)   All the oxygen atoms are considered to be equivalent and diffuse by the same mechanism.

b)   Variations in the diffusion constants with respect to the different crystallographic directions are ignored. In reality this may be true because different results have been observed in different crystal orientation.

c)   The diffusion constant in different phases is assumed to be the same.

d)   Oxygen loss is assumed to occur from the profile edge. Experimentally, if new phases formed at the top and bottom surfaces, this would have been readily visible. The exact reason why loss occurs primarily from the side surface is still unclear.

To describe the transformation process, a simplified model that includes diffusion of oxygen in the bulk and the movement of the interfaces is proposed. Consider a phase transformation which occurs at time t, and a corresponding interface which appeared at a distance of y(t) away from the profile surface, the oxygen concentrations in the original and new phases are determined by the diffusion equation.

$$\frac{\partial u}{\partial t} = D\frac{\partial^2 u}{\partial x^2}, \quad 0 < x < y(t), \quad x > y(t) \tag{4.2}$$

with a radiative boundary condition which describes the oxygen loss at the surface.

$$\frac{\partial u}{\partial x} = hu, \quad x = 0 \tag{4.3}$$

and

$$u = u_0, \quad t = 0 \tag{4.4}$$

where   u = concentration of oxygen.

D = diffusion coefficient.

x = distance from the surface.

y(t) = location of the interface.

u_+ = concentration of oxygen at the right of the interface (See figure 4.35).

u_- = concentration of oxygen at the left of the interface (See figure 4.35).

u_0 = initial concentration of oxygen at the surface.

h = a constant that characterizes the loss of oxygen.

In the case of diffusion controlled growth, the interface moves slowly and u_+ and u_- are equal to the equilibrium values. The interface velocity can be derived from the balance of mass (Christian 1981 and Hillert 1975) and is given by

$$D \left[\frac{\partial u}{\partial x} \Big|_{y-0} - \frac{\partial u}{\partial x} \Big|_{y+0} \right] + y' (u_+ - u_-) = 0 \tag{4.5}$$

In the case of interface controlled growth, the equilibrium concentration can not be reached and there is no concentration step at the interface, i.e., $u_+ = u_-$. The velocity of the interface can derived from the driving force for the growth (Christian 1981 and Hillert 1975) and is given by

$$y'(t) = k (u_e - u_+) \tag{4.6}$$

where u_e is the equilibrium concentration.

For the process under consideration, the limiting cases of interface- and diffusion-controlled can not be applied. This means that the concentration step on the interface is equal to zero at the moment that the interface appears, and then increases. This implies that u_- and u_+ are not given constants, but functions of time. To derive the velocity of the interface, both the balance of mass and the kinetics equation should be considered.

A similar model has been proposed by Aziz *et al* (1988) for the solidification of a two-component melt. In the case of the phase transformation in V_2O_5 under electron beam irradiation, the velocity of the interface is given by (Volpert 1992).

$$y' = k \; [u_e - (s \; u_e^- + (1-s) \; u_-)] \qquad (4.7)$$

where: u_e^+ = equilibrium concentration of the original phase

u_e^- = equilibrium concentration of the new phase

$$\sigma_1 = - \frac{\partial \sigma(u_e^+, \; u_e^-)}{\partial u_+}$$

$$\sigma_2 = - \frac{\partial \sigma(u_e^+, \; u_e^-)}{\partial u_-}$$

$$s = \frac{\sigma_1}{\sigma_1 + \sigma_2}$$

$$\sigma(u_+ + u_-) = - \frac{\Delta \mu}{RT}$$

R = gas constant

T = temperature

$\Delta\mu$ = the free energy difference responsible for the interface motion

The condition for the appearance of an interface is when the size of the nuclei exceeds the critical nucleus size y_0. Suppose that an interface appears at time t_1 and let

$$u|_{x=y_o} = u_{e_1} \qquad (4.8)$$

then we have

$$y(t_1) = y_o \qquad (4.9)$$

$$u_\pm(t_1) = u_{e_1} \tag{4.10}$$

The conditions for the appearance of the second interface are similar. The condition for the disappearance of an interface is when the width of the phase is less than the critical width, i.e.

$$z(t) - y(t) < y_o \tag{4.11}$$

where z(t) is the location of the second interface.

A finite-different method using the Thomas algorithm was used for the numerical computation of equations (4.2) and (4.7), yielding the distribution of the oxygen concentration and the location of the interface. The detailed calculation has been presented by Volpert *et al* (1992).

Figure 4.36 shows the evolution of u_- and u_+ with time for the case of one interface. The numerical parameters used in this simulation are: $u_o = 50/nm^3$; $u_e = 25/nm^3$, $y_o = 4$ nm; $l = 2nm$ and $s = 0.5$. In the simulation, values of k, h and D were varied until the best fit to the experimental data (Flux = 0.5 A/cm^2) was obtained. A best fit was achieved when k $= 0.0015$ nm^4/s, h $= 0.004$/nm and D $= 5.9$ x 10^{-18} m^2/s. These numbers appear to be quiet reasonable, especially the value of diffusion coefficient which is of the same order of magnitude as the experimental values for oxides. For example, the diffusion coefficient of oxygen in Al_2O_3 at room temperature is 4.4 x10^{-18} m^2/s (Samsonov 1973). This provides some confidence in the model. By substituting s = 0.5, Equation 4.7 can be rewritten as the following:
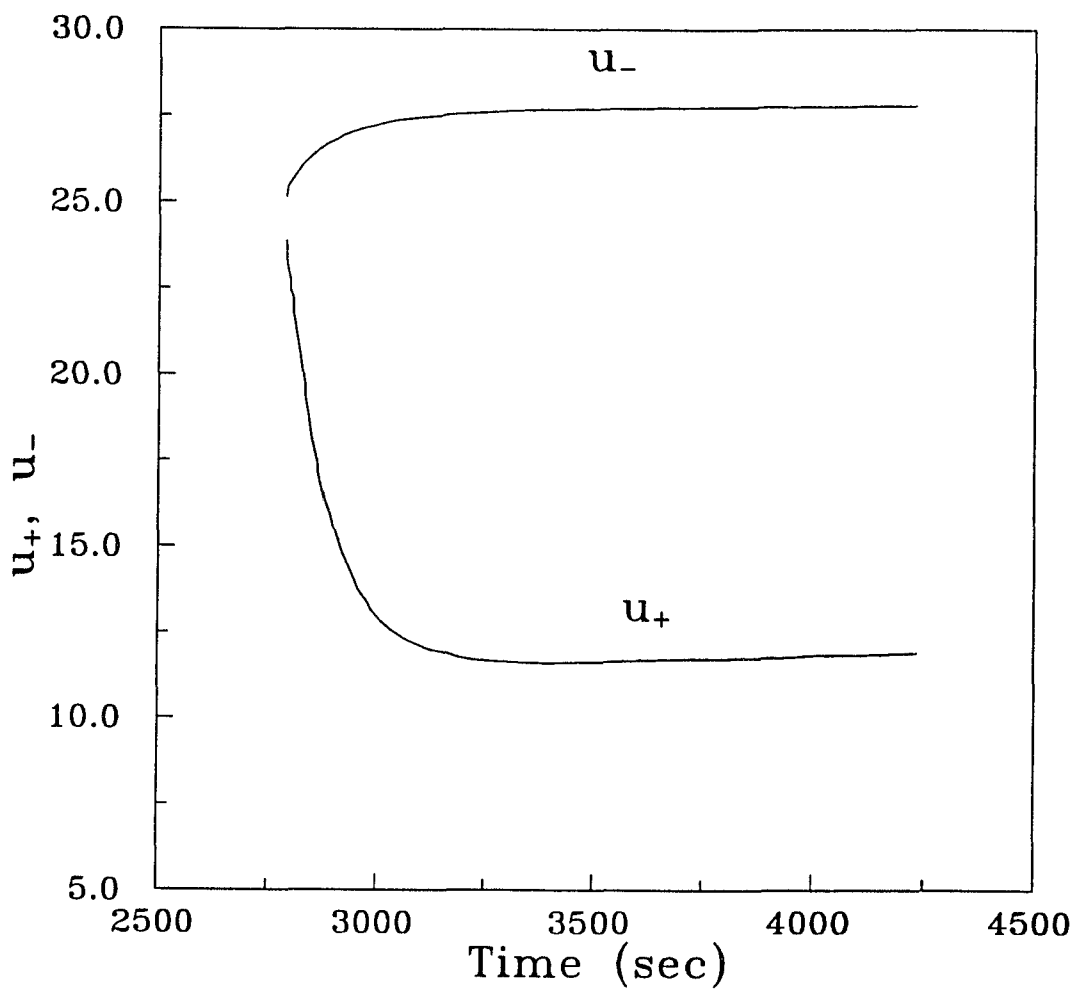
Figure 4.36 Time evolution of u. and u+ (Courtesy of V. A. Volpert).

$$y' = k \left[u_e - \frac{1}{2} (u_+ + u_-) \right]$$
(4.12)

Figure 4.37 shows the distribution of oxygen concentration at consecutive moments of time after the appearance of the first interface. At the moment t_o when the interface appears, $u_+ = u_- = u_e$ and the interface velocity equals zero from Equation 4.8. u_+ increases while u_- decreases to some constant, resulting in an increase of the interface velocity, $y'(t)$. This behavior of $y'(t)$ agrees with the experimental observations. It was observed experimentally that the interface velocity of VO, represented by the slope of the kinetics curve, was initially slow, then increased to a constant.

For the case when two interfaces propagate into the bulk, the best fit was obtained for the following parameters: $D = 5.9 \times 10^{-18}$ m/sec, $h = 0.0036$ /nm, $u_{1e} = 25$ /nm^3 and $y_o = z_o = 1$ nm. The value of h corresponds to the value of the electron flux of 1.8 A/cm^2 for which the propagation of two interfaces, V_4O_9/V_2O_5 and VO/V_4O_9, was experimentally observed. As shown in Figure 4.37, as soon as the first interface appears and propagates into the bulk, the oxygen concentration on the left of the interface (new phase) decreases drastically. As a result, the condition for the appearance of the second interface is satisfied in a shorter time period, meaning that the first phase transformation accelerates the appearance of the second one.

Figure 4.38 shows the oxygen concentration profile at consecutive moments in time. The concentration is linear with respect to time in interval of $0 \le x \le z(t)$ and close to constant over $x \ge y(t)$. The oxygen concentration in the interval of $z(t) \le x \le y(t)$ does not
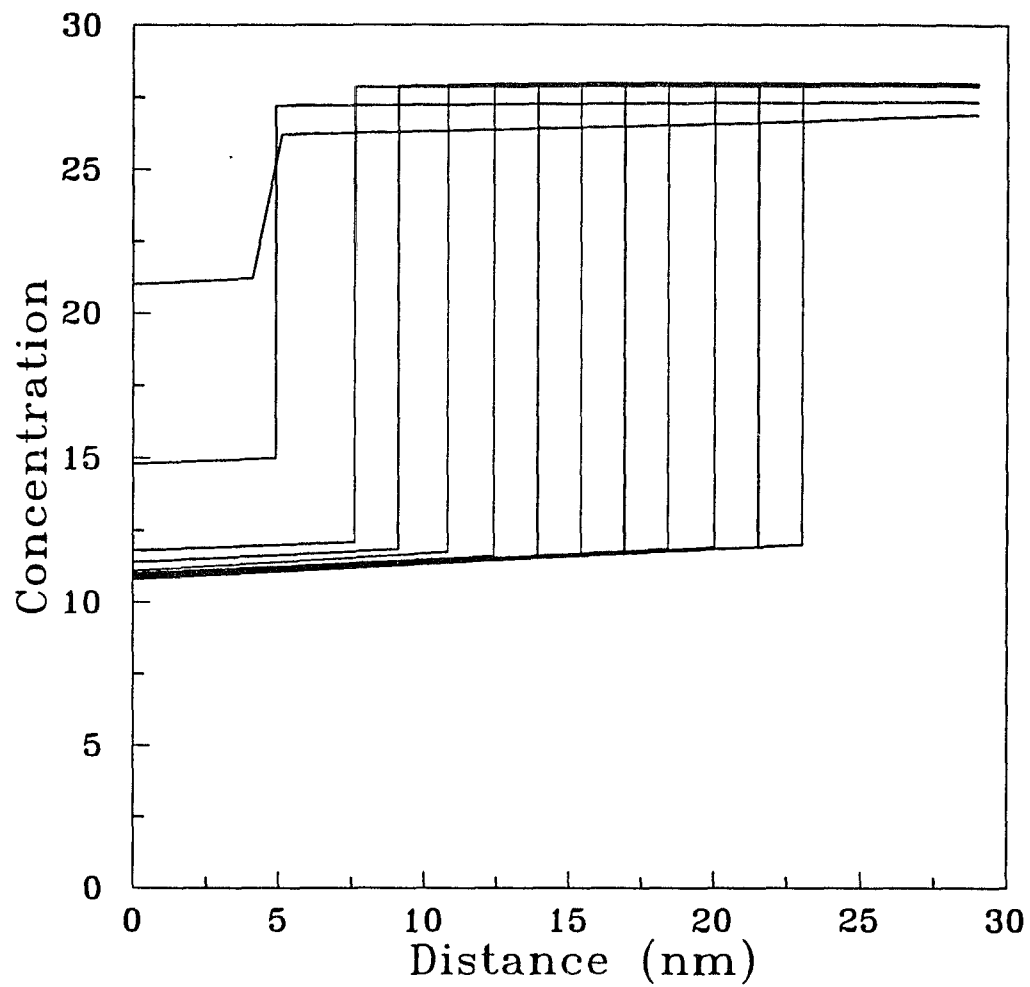
Figure 4.37   Time evolution of the oxygen concentration of the original and new phase at the interface (Courtesy of V. A. Volpert).
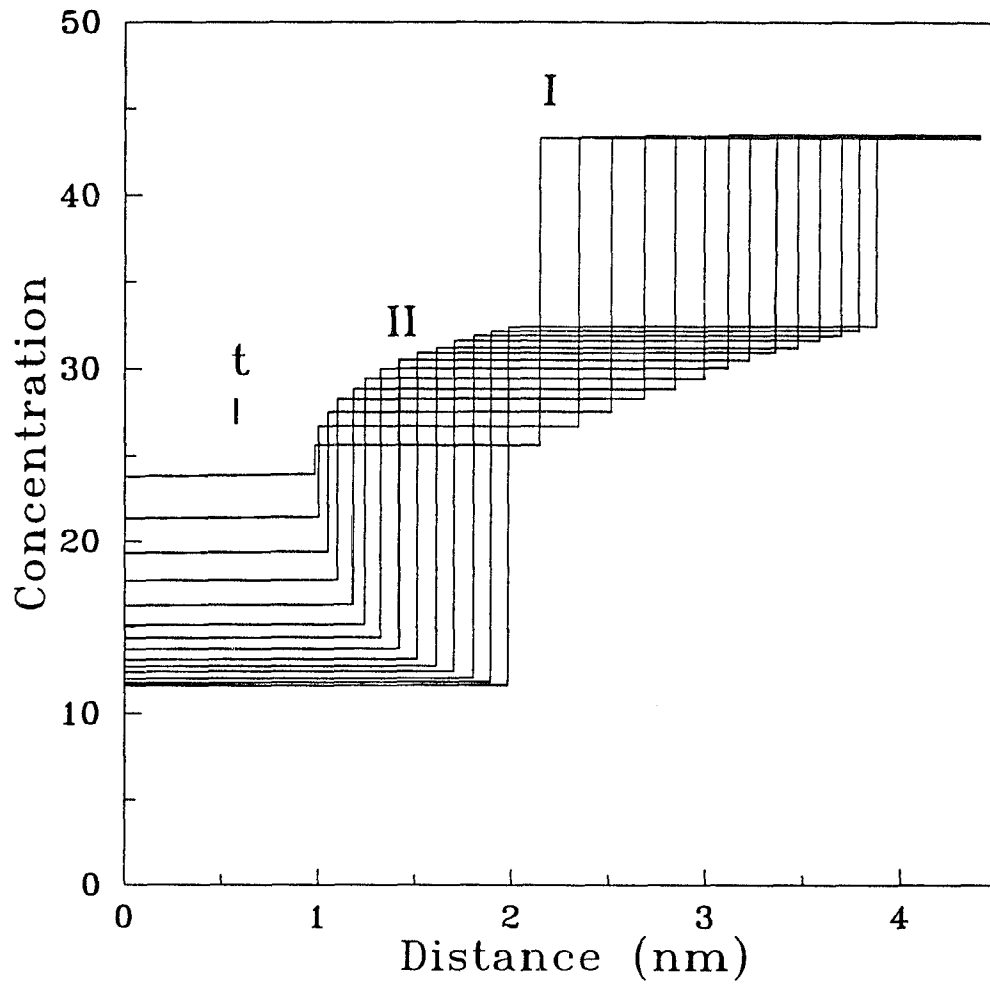
Figure 4.38   Time evolution of the oxygen concentration in the case of two interfaces (Courtesy of V. A. Volpert).

depend on x, but increases as a function of time. This leads to an increase in $(u_+^1 + u_-^1)$, and therefore a decrease in the velocity of the first interface (See Equation 4.12), implying that the formation of the second interface slows down the velocity of the first one. For the second interface, the increase in the oxygen concentration on the right of the interface is compensated by the decrease of the concentration on the left due to the diffusion to and the mass loss at the surface. Thus the velocity of the second interface decreases slowly.

In the simulation, if the value of h is increased from 0.0036/nm to 0.004/nm, then only one interface occurs. What happens at the higher flux regime is that in the simulation the critical concentration for the formation of the second interface was satisfied before the condition of critical width. The formation of the stable second phase is consequently prohibited.

A comparison of the numerical simulation with the experimental observation shows that they correlate very well. The formation of the second interface slows down the velocity of the first, they merge, and the first interface disappears. This further confirms that the electron induced phase transformation process in V_2O_5 is not purely diffusion controlled. Indeed, if this is purely diffusion controlled, the interface can not merge. In this case, when the second interface comes near to the first one, the concentration gradient on the left of the first interface increases, i.e. $\frac{\partial u^1}{\partial x}\big|_{y-0}$ increases while $\frac{\partial u^1}{\partial x}\big|_{y+0}$ remains the same, consequently the velocity of the first interface would increase as indicated by equation 4.5. Using the same argument, the velocity of the second interface

decreases. Hence, the two interface can never merge.

§4.4.3 Effects of Low Energy Electron Irradiation

Historically, ESD studies are divided into two categories: the direct detection of desorbed species and the characterization of the surface changes. Studies of the second approach are sub-divided into the analysis of changes of surface chemistry by the standard surface science techniques such as AES, XPS and EELS; and the analysis of surface structural changes by LEED (DIET I 1983, DIET II 1965, DIET III and DIET IV) and HREM (Hobbs 1979, Marks 1986, Smith 1987 and Buckett 1989). However no comparison between studies using these different techniques has been made due to the instrumentation limitations. For example, studies using conventional surface science techniques usually give information about the effect of low energy electron irradiation, whereas HREM studies have been generally focused on the damage behavior in the higher energy regime, typically > 100 keV. The bridge to combine these two approaches would be an electron microscope attached with a fully equipped surface science chamber. In this thesis work, effects of low energy electron irradiation (100 - 3000 eV) were studied by XPS and mass spectrometry in the VG ESCA chamber, and by HREM in the UHV H-9000. The results were compared and correlated.

HREM Studies

In the UHV specimen transfer chamber, effects of low energy electron irradiation were investigated and the phase transformations were examined by HREM. A Varian

LEED electron gun (0 - 3 keV with a maximum emission current up to 3 μA) was used as a radiation source. Samples were V_2O_5 powders samples supported on holey carbon or silica films. Samples were first irradiated by low energy electrons in the side chamber and then transferred into the microscope for structural examinations. During microscopy, the electron beam flux was minimized to avoid any further irradiation. Figure 4.39 shows the high resolution images taken from three different crystals after 15 min irradiation of 100 eV electrons at a flux of 25 μA/cm^2. An amorphous layer about 4 nm thick was formed on the surface. With increasing irradiation time, the thickness of these amorphous layers remained approximately the same.

The end product after 15 min, 3 keV electron irradiation at a flux of 0.7 mA/cm^2 was a polycrystalline β-V_6O_{13} phase shown in Figure 4.40. The average grain size was about 6.0 nm in diameter. The layer of the β-V_6O_{13} phase extended into the bulk at a distant of more than 100 nm from the surface. Table 4.12 summarizes the results obtained at various energies.

TABLE 4.12 Summary of HREM Results of Different Energies

Energy (eV)	Flux (A/cm^2)	Phase Transformation
100	2.5 x 10^{-5}	Amorphous layer of 4 nm thick
3000	7.0 x 10^{-4}	β-V_6O_{13} of 6.0 nm in diameter
300 k	1.0	V_2O_5 ->V_4O_9 -> β-V_6O_{13} -> VO

A correlation between these observations can be made using a simple diffusion-limited solid state reaction. Let an oxygen atom and an oxygen vacancy be represented
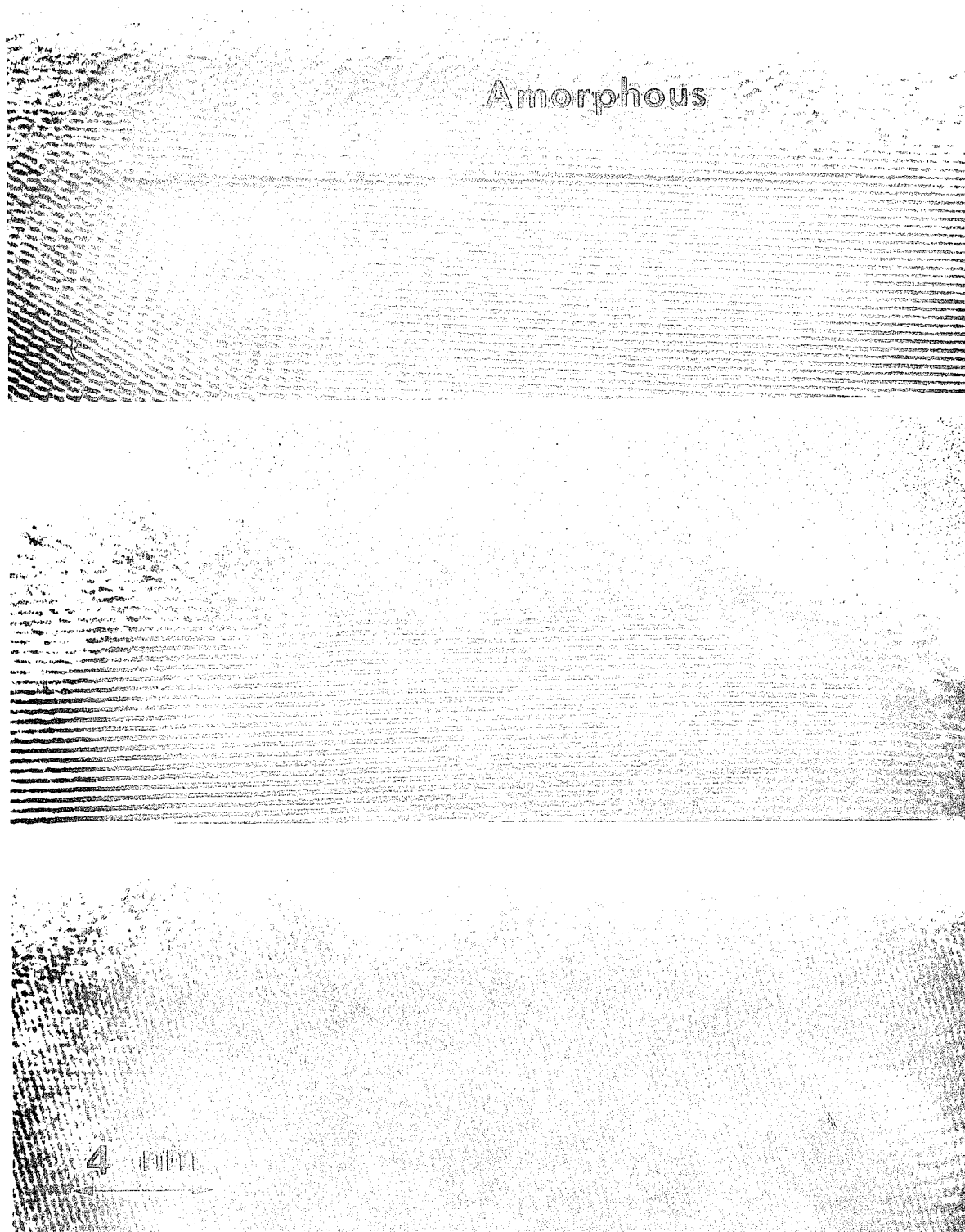
Figure 4.39   High resolution image taken from three different crystals after 15 min,
100 eV electron irradiation at a flux of 25 μA/cm².
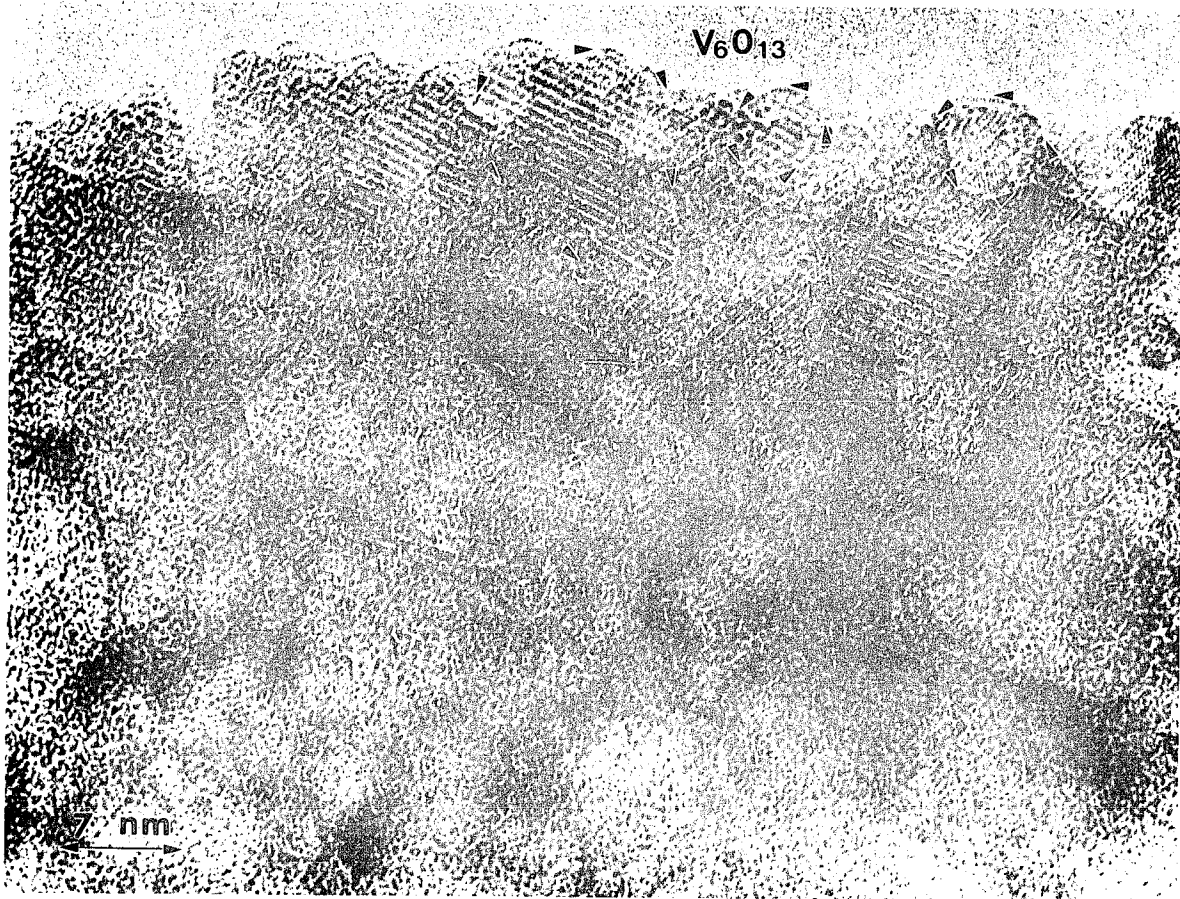
Figure 4.40   High resolution image taken after 15 min, 3 keV electron irradiation at a flux of 0.7 A/cm².

by O and V_O respectively, the surface desorption of O_+ can then be written by a solid state reaction:

$$O^{2-} \rightarrow O^+(g) + V_O(s) + 3e^- \tag{4.13}$$
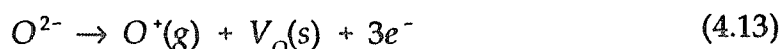
where s denotes the solid phase, g the gas phase and e^- an electron. The reaction is followed by the diffusion of oxygen vacancies from the surface into the bulk. If the reaction is rate-limited, homogeneous oxygen loss occurs without any structural modification as long as the overall V/O ratio does not exceed the critical value. On the other hand, if the reaction proceeds much faster than the bulk diffusion, lower oxides may be formed. According to the DIET theory, the rate-limited reaction is in fact unlikely and the formation of the lower oxide is expected since the process of oxygen desorption occurs at a time scale of 10^{-10} sec (DIET I 1983), which is substantially faster than the rate of bulk diffusion. For example, assuming that the diffusion constant is on the order of 10^{-18} m^2/sec, the time for an oxygen atoms to diffuse through a distance of 100 nm would be about 10^4 sec. Our experimental observations also suggest that the reaction is kinetic-limited by diffusion and the surface structure left behind after the oxygen desorption totally depends on the rate of oxygen diffusion from the bulk. Under 100 eV electron irradiation, while the rate of surface desorption is fast due to the large interaction cross-section, the rate of thermal diffusion is slow. In this case, the irradiation-assisted diffusion is limited to a surface layer of a thickness determined by electron penetration depth which is on the order of a few nm. Therefore the contribution of electron-assisted diffusion is insignificant to the bulk diffusion of oxygen toward the surface. The surface

desorption consequently resulted in the formation of highly defective surface layer which collapsed to an amorphous region upon further irradiation. Moreover it was noted that the damage was limited to a surface layer of a thickness of 4 nm, which is on the same order of magnitude as the electron penetration depth at this energy. This further confirmed that at this energy bulk diffusion of oxygen did not contribute to the damage process.

The formation of β-V_6O_{13} at 3 keV is readily explained by the rapid diffusion of oxygen from the bulk, which is greatly enhanced by the electron irradiation. The domain structure suggests that the desorption took place at preferential sites. Indeed from a structural point of view, the shear transformation from V_2O_5 to β-V_6O_{13} requires that the V-O_1 bonds to be broken preferentially.

ESCA Studies

In addition to surface structural studies using HREM, XPS was used to study changes in surface chemistry during low energy electron irradiation. Figure 4.41 shows the vanadium $2p_{2/3}$ characteristic peak collected under two conditions: before and after 60 min, 500 eV electron irradiation at a flux of 0.2 mA/cm^2. The chamber pressure was in the low 10^{-10} torr range. The vanadium peak taken after the electron irradiation shifted toward lower binding energy, suggesting that the vanadium was reduced to its lower oxidation states.

Desorbed species during electron irradiation were detected by a quadruple mass spectrometer in the SIMS chamber. Figure 4.42 shows a mass survey spectrum of
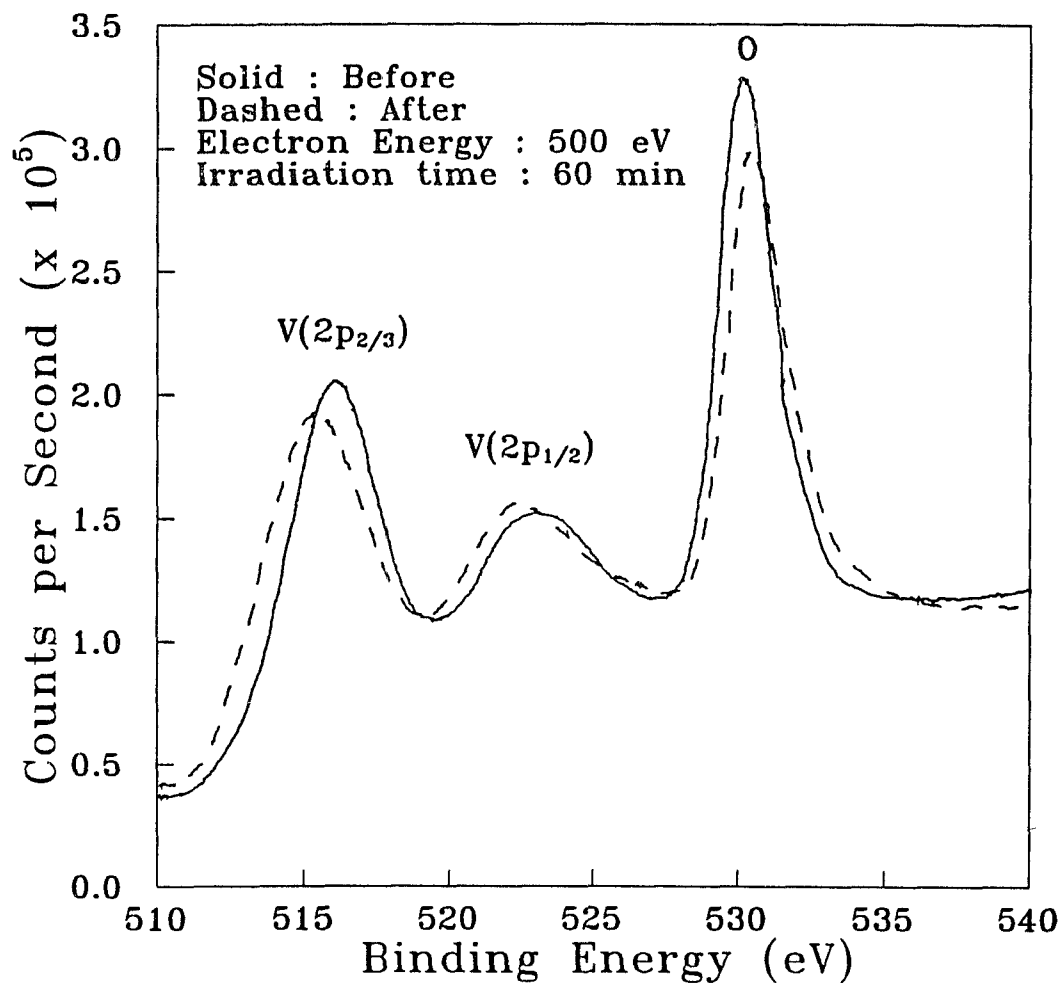
Figure 4.41   XPS spectrum of vanadium $2p_{2/3}$ characteristic peak taken before and after 30 min, 500 eV electron irradiation at a flux of 0.2 mA/cm^2.
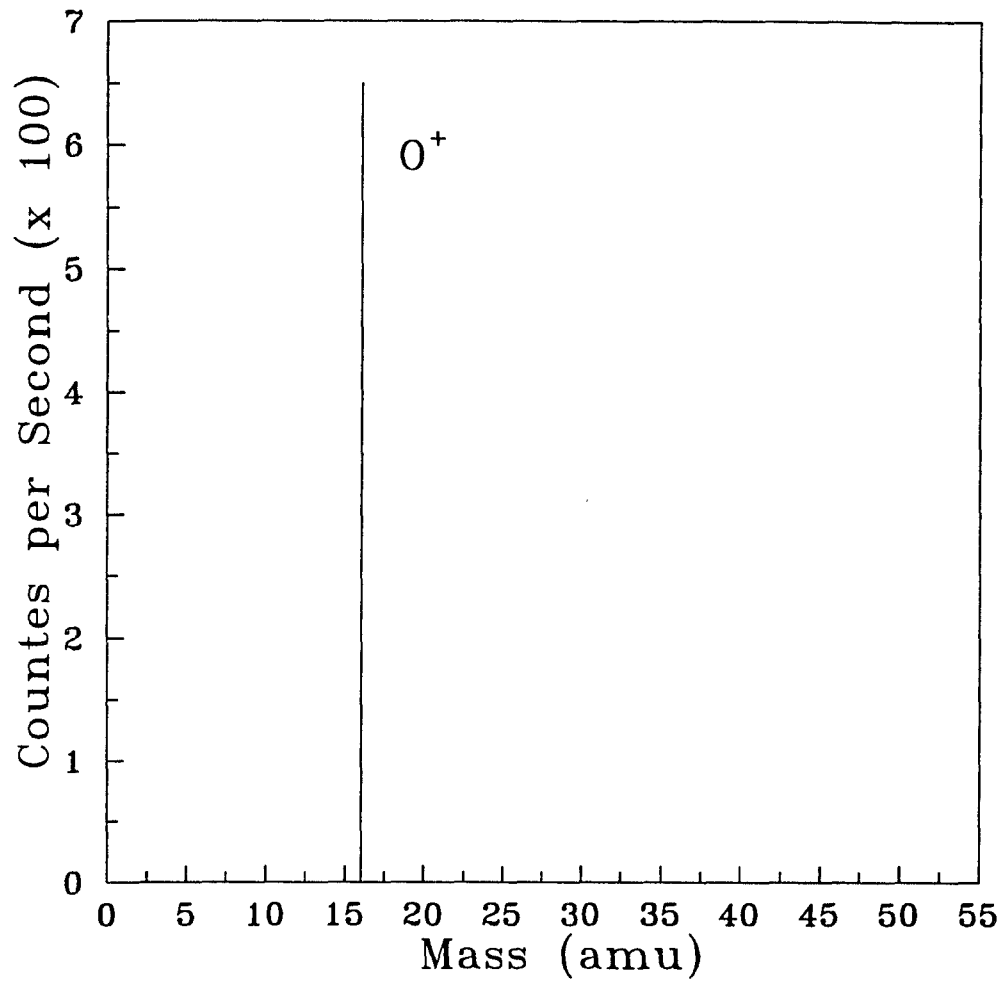
Figure 4.42   Mass survey of positive ions taken during 500 eV electron irradiation at a flux of 0.2 mA/cm^2.

positive ions taken during 500 eV electron irradiation at a flux of 0.2 mA/cm^2. In the spectrum, only the positive oxygen ions were detected. In order to confirm that these positive oxygen ions were desorbed from the V_2O_5 target, rather from fragmentation from the oxygen containing species in the gas background in the electron beam, an oxygen isotope experiment was performed (Jacoby 1990). In this experiment, the V_2O_5 target was annealed with ^{18}O at 500°C. XPS spectrum of the treated surface indicated that the surface ^{16}O was partially exchanged with ^{18}O. The same ESD experiment was then repeated, showing the desorption of $^{18}O^+$. The detection of the positive oxygen ions is consistent with the theoretical prediction of the ESD mechanism and agrees with the results by Feibelman (1978). Furthermore, careful mass survey showed that no negative ions, either oxygen or vanadium, were detected.

DIET theory predicts that neutral oxygen atoms desorb at a ratio of 10^6 with respect to the O^+ yield. However, in the literature no direct detection of atomic oxygen was reported. The difficulties of detecting atomic oxygen are caused by its high chemical reactivity and instrumentation limitations (Outlaw 1987). For example, there are several problems associated with the detection of atomic oxygen with a mass spectrometer. The first is the presence of CH_4 in the UHV chamber since both ^{16}O and CH_4 have a mass of 16 amu. The second is O^+ signal from the fragmentation of the oxygen containing species in the electron beam. So far, no direct experimental evidence has been obtained to support the theoretical prediction of the desorption of atomic oxygen during ESD. Furthermore the results obtained by Jacoby (1991) indicate the O^+ yield collected by mass spectrometer accounts for the decrease of the surface oxygen on V_2O_5.

The kinetics of the desorption process were studied by monitoring the yield of the positive oxygen ions as a function of time under different substrate temperatures. Figure 4.43 shows two plots of the O^+ yield as a function of time measured during 700 eV electron irradiation at a flux of 0.3 mA/cm^2 and the substrate temperatures of 380°C and 550°C. The general trends of the kinetics of the O^+ desorption under these two temperatures were similar: a fast decrease in the first 10 min followed by a slow decrease. The O^+ yield leveled off after prolonged electron irradiation. At both of these temperatures, the O^+ yield was inversely proportional to $t^{1/2}$.

§4.5 Summary and Conclusion

In this study electron-induced surface radiation damage in V_2O_5 have been systematically studied as a function of controlled experimental parameters such as electron beam flux and energy, crystal orientation and surface environment. The effects of electron irradiation were investigation by two approaches. One was to detect the desorbing particles by mass spectrometry. The other was to characterize the surface left behind. Electron microscopy was used to study the structural changes and the XPS for the chemical changes. Mass spectrometry indicated that during electron irradiation, positive oxygen ions were the dominant desorbing particles and accounted for the oxygen deficiency on the surface observed by XPS. No negative oxygen ions or vanadium particles were detected. The shift of the vanadium characteristic peak to the lower binding energy in the XPS spectrum suggested that V^{5+} was reduced to the lower oxidation states. Studies of electron microscopy showed that the desorption of positive
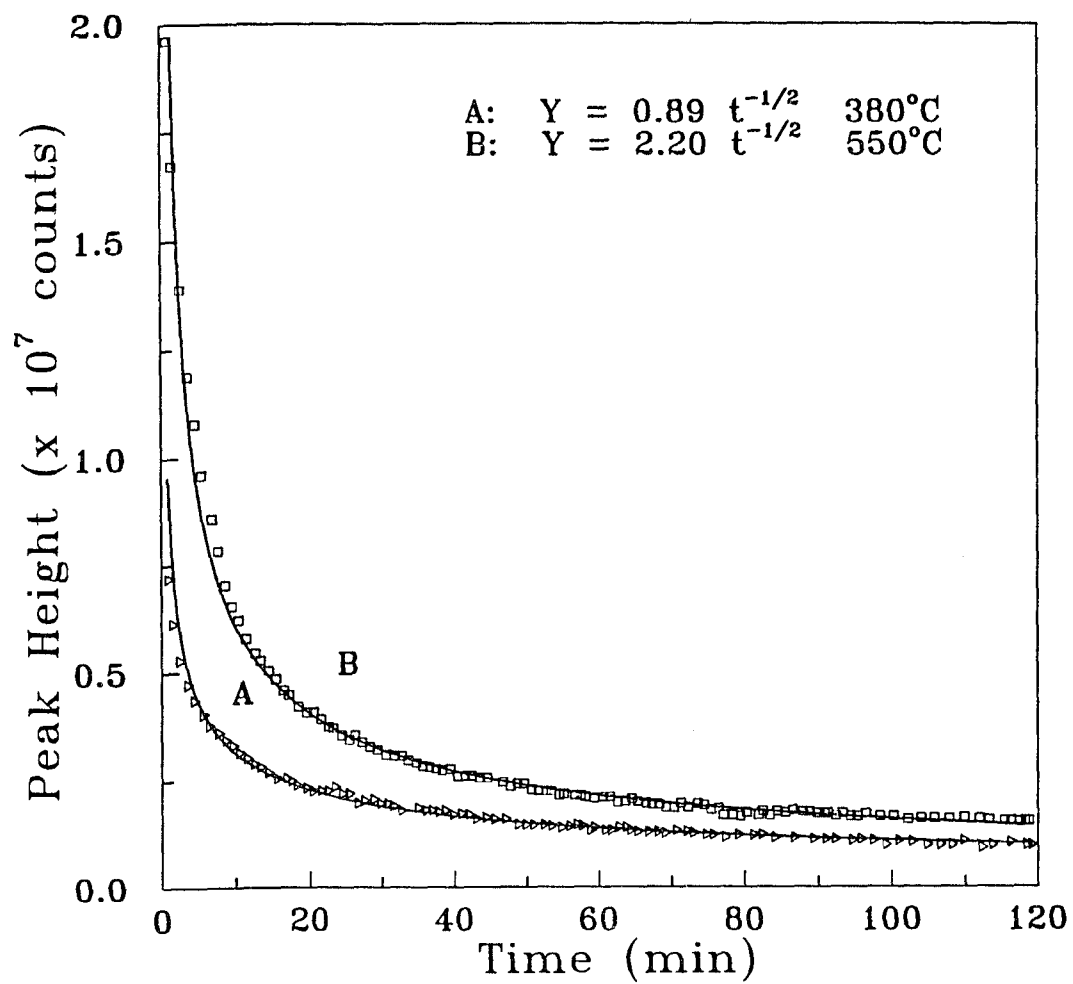
Figure 4.43   Plots of the O^+ yield vs. time taken during 700 eV electron irradiation at a flux of 0.3 mA/cm² and substrate temperatures of 380°C and 550°C.

oxygen ions led to a phase transformation of V_2O_5 to VO through different intermediate phases. The intermediate phases observed were V_4O_9, β-V_6O_{13}. Well defined orientation relationships among V_2O_5, V_4O_9, V_6O_{13} and VO were observed. The phase transformation route and kinetics depend strongly on the electron energies and fluxes, crystal orientations. The variation of the microstructure of the irradiated surfaces as a function of electron beam energies and fluxes can be attributed to the changes of the nucleation and growth processes under different experimental conditions. A theoretical model was proposed to simulate the kinetics of the damage process. In this model the phase transformation was considered as an one dimensional diffusion problem with a radiative boundary for the oxygen desorption. This model explains the variation of the phase transformation route with electron beam fluxes and suggests that the rate-limiting step of the phase transformation is oxygen diffusion from the bulk.

CHAPTER 5 ELECTRON STIMULATED SURFACE DAMAGE AND REACTIONS IN ReO₃ AND ALKALINE EARTH FLUORIDES

§5.1 INTRODUCTION

As demonstrated in chapter 4, the dominant damage mechanism in V_2O_5 is electron stimulated desorption of oxygen. In many cases, the surface environment can play a significant role in the damage process under electron beam irradiation. For example, it has been observed that the chemical reaction of atomic oxygen on the surface of space shuttles in the space environment causes material transformation, resulting in performance degradation (Fella 1981). The objectives of this study are two folds. The first is to evaluate the effect of surface environment on the electron-induced damage process. The second is to extend the studies of surface radiation damage to other less studied systems, such as a metallic oxide (ReO_3) and a fluoride (CaF_2).

§5.2 REVIEW OF PROPERTIES OF ReO₃ AND CaF₂

§5.2.1 Structural and Electronic Properties of ReO₃

The structure of ReO_3 was first determined by Meisel (1932) using x-ray diffraction. ReO_3 has a simple cubic structure as shown in Figure 5.1. It belongs to the Pm3m space group with a lattice parameter of 3.742 Å. The unit cell contains a single molecule with atoms at the following positions:

Re: (1a) 0, 0, 0

O: (3c) ½, 0, 0; 0, ½, 0; 0, 0, ½

154

$\circ = \mathrm{Re}^{6+}; \quad \bigcirc = \mathrm{O}^{2-}$
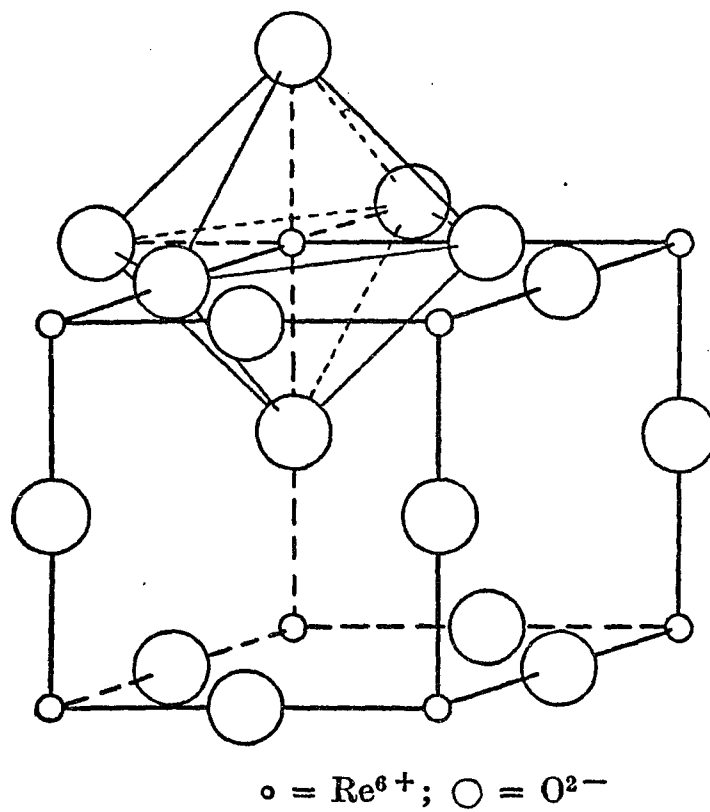
Figure 5.1 Structure of ReO_3.

The basic building blocks are ReO_6 octahedra joined by sharing corners.

The electrical properties of transition metal oxides range from insulators, to semiconductor to metals (Henrich 1985). The common feature of these oxides is an incomplete electron d shell of the metal ions which determines the diverse properties of these compounds. Among the group of transition metal oxides, rhenium trioxide exhibits properties of a good metallic properties (Ferretti 1965). The outer electron shell in the rhenium atom has the configuration of $5d^6 6s^2$. In a purely ionic ReO_3 compound of Re^{6+} and O^{2-}, the cation would have one electron remaining in the d shell. The delocalization of this d-electron gives rise to the metallic property of ReO_3 (Ferretti 1965). The similar oxide of tungsten, with an empty d shell is found to be an insulator.

The first experimental evidence showing the metallic conductivity of ReO_3 was reported by Ferretti *et al* (1965). The resistivity values are shown in Figure 5.2 as a function of temperature between 77 and 300°K. The values are remarkably low for a transition metal oxide. At room temperature the resistivity is about one order of magnitude lower than that of the most highly conducting tungsten bronzes and the value at 77°K is close to that of electrolytically pure silver at this temperature.

§5.2.2 Structural and Electronic Properties of CaF_2

CaF_2 has a fluoride structure with a lattice constant of 5.46 Å. It is a good insulator with a band gap energy of 12 eV. In recent years, there has been a growing interest in the incorporation of CaF_2 as an insulator in semiconductor devices. Unfortunately, the investigation of CaF_2 has been hampered by the decomposition caused by ionizing
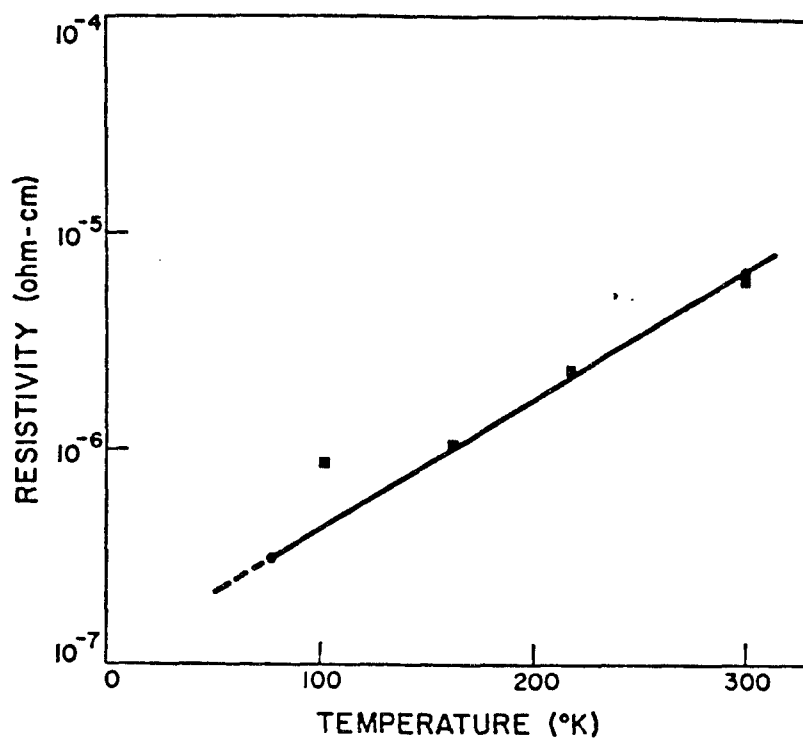
Figure 5.2   The resistivity values of ReO_3 as a function of time (Ferretti 1965).

radiation. Electron irradiation of CaF_2 with a typical energy range of 3 - 5 keV and beam currents of 5 - 10 µA employed in AES has been shown to cause pronounced changes in the surface chemical composition (Strecker 1981, Scheinfein 1986, Saiki 1987 and Baunack 1990). AES analysis shows that the decomposition is due to the fluorine desorption, indicated by a decrease of the fluorine signal. The surface left behind is Ca-rich in a metallic-like state.

§5.3 EXPERIMENT

Samples were made of high purity powders of ReO_3 (99.95%, Cerac) and CaF_2 (99.99%, AESAR/Johnson Matthey). The impurities detected in ReO_3 include Ca and Mg with a concentration of less than 0.001%. The impurities detected in CaF_2 include less than 0.035% of Na, 0.01% of Al, Ba, Mn, Sr and K, 0.005% of Cl and Mg, 0.001% of Cl, Cr, Co, Fe, Pb and Ni, and 0.0001% of Cu. The data on impurities were provided by the Johnson Matthey Company.

TEM samples were prepared by grinding powders in an alumina mortar and pestle while dispersed in methanol or acetone, which was then deposited on a holey carbon or silica film supported on a copper grid. Each sample was baked on a 150 W light bulb to reduce the surface hydrocarbon contaminations just prior to insertion into the Hitachi H-9000 electron microscope. For UHV observation, ReO_3 samples were annealed at about 600°C in 1 torr partial pressure of high purity oxygen for about half hour in the side chamber before being loaded into the Hitachi UHV H-9000 electron microscope. The electron flux was measured by an exposure meter which was calibrated by a Faraday cup.

During observation of ReO_3, the electron flux was maintained at about 5.0 A/cm². For CaF_2, the electron beam flux was maintained at 1.0 A/cm². The resulting structures of the new phase were identified by SAED, optical diffraction and HREM

§5.4 RESULTS

Experimental results in this section are presented in two parts. The first part describes the electron induced surface reactions of ReO_3 with carbon. The second part details the results on the electron stimulated damage and oxidation of CaF_2 to CaO.

§5.4.1 Surface Reactions of ReO_3 with Carbon

Non-UHV on Carbon Substrates

The initial studies were carried out in the non-UHV environment of the Hitachi H-9000 electron microscope and samples used were generally on holey carbon substrates. Figure 5.3 shows the selective area diffraction patterns taken from a ReO_3 crystal oriented along [011]. Figure 5.3a was taken as soon as the crystal was tilted to the zone axis. Figure 5.3b was taken after 30 min electron irradiation, in which a new set of diffraction spots was observed, indicating the formation of a new phase. The new phase can be indexed as an fcc structure with a preferred orientation of [110] and a lattice parameter of 4.00 ± 0.05 (Å).

Figure 5.4 shows a time sequence of high resolution images taken from the same crystal. Figure 5.4a was taken as soon as the bulk crystal was tilted to the [011] zone axis (about 5 min), showing that a thin layer of the new phase has formed on the surface.

Figure 5.3   Time sequence of selected area diffraction patterns taken along [011]. a) initial; b) 30 min.
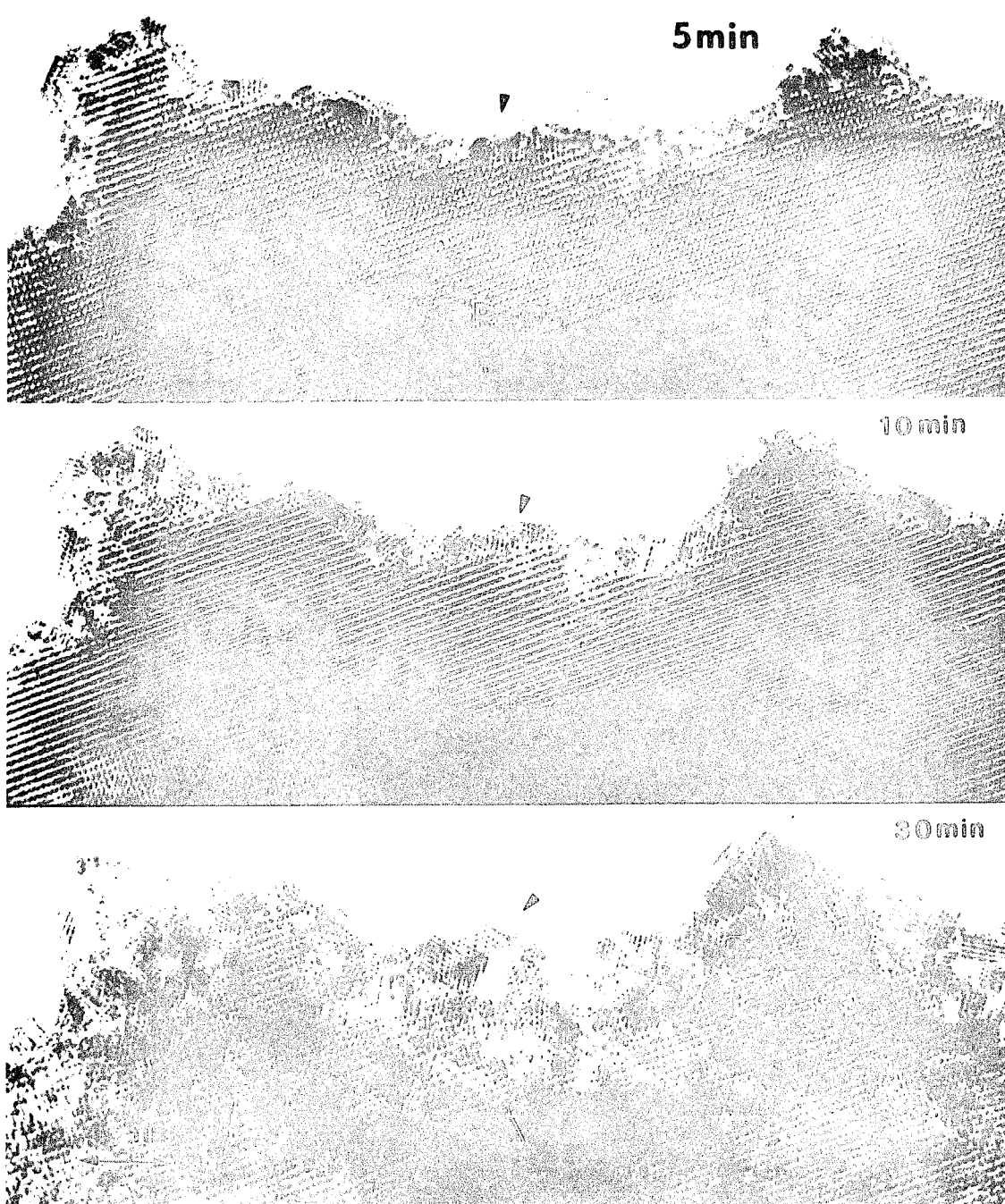
Figure 5.4   Time sequence of high resolution image taken along [011]. a) initial (5 min); b) 15 min; c) 30 min.

With increasing irradiation time, this layer of new material grew thicker, as indicated in Figure 5.4b and 5.4c. More importantly, Figure 5.4c which was taken after 30 min of irradiation, shows that the new phase not only formed on the surface that is parallel to the electron beam direction, but also formed on the top and bottom surfaces as indicated by the arrows. This damage behavior is different from that in the maximal transition metal oxides, where electron radiation damage always initiated at the surface and propagated into the bulk with a clear reaction front (Fan 1989 and Singh 1989). In addition, a thin layer of amorphous contaminants indicated by arrows in these images can be clearly seen. These contaminants resulted from the sample preparation in air.

Figure 5.5 was taken from a ReO_3 single crystal oriented along the [100] zone axis after about 20 min of irradiation. A layer of the same new phase can be observed in this image. The fringes indicated by arrows correspond to the (111) planar distance of the new phase.

The same phase transformation was observed in a ReO_3 crystal oriented along [112]. As shown in Figure 5.6, a thin layer of the new phase can be seen after about 20 min of electron irradiation. However, it should be pointed out that the phase transformation rates along [100] and [112] are noticeably slower than that along [011]. It was also noticed that regardless of the crystal orientations, the new phase always has an orientation of [110].

In the studies of phase transformations, two aspects are equally important. One is to study what is the final phase. The other is to study the kinetics, i.e. the rate of phase transformation. In this study the kinetics of the phase transformation was measured by

3 nm
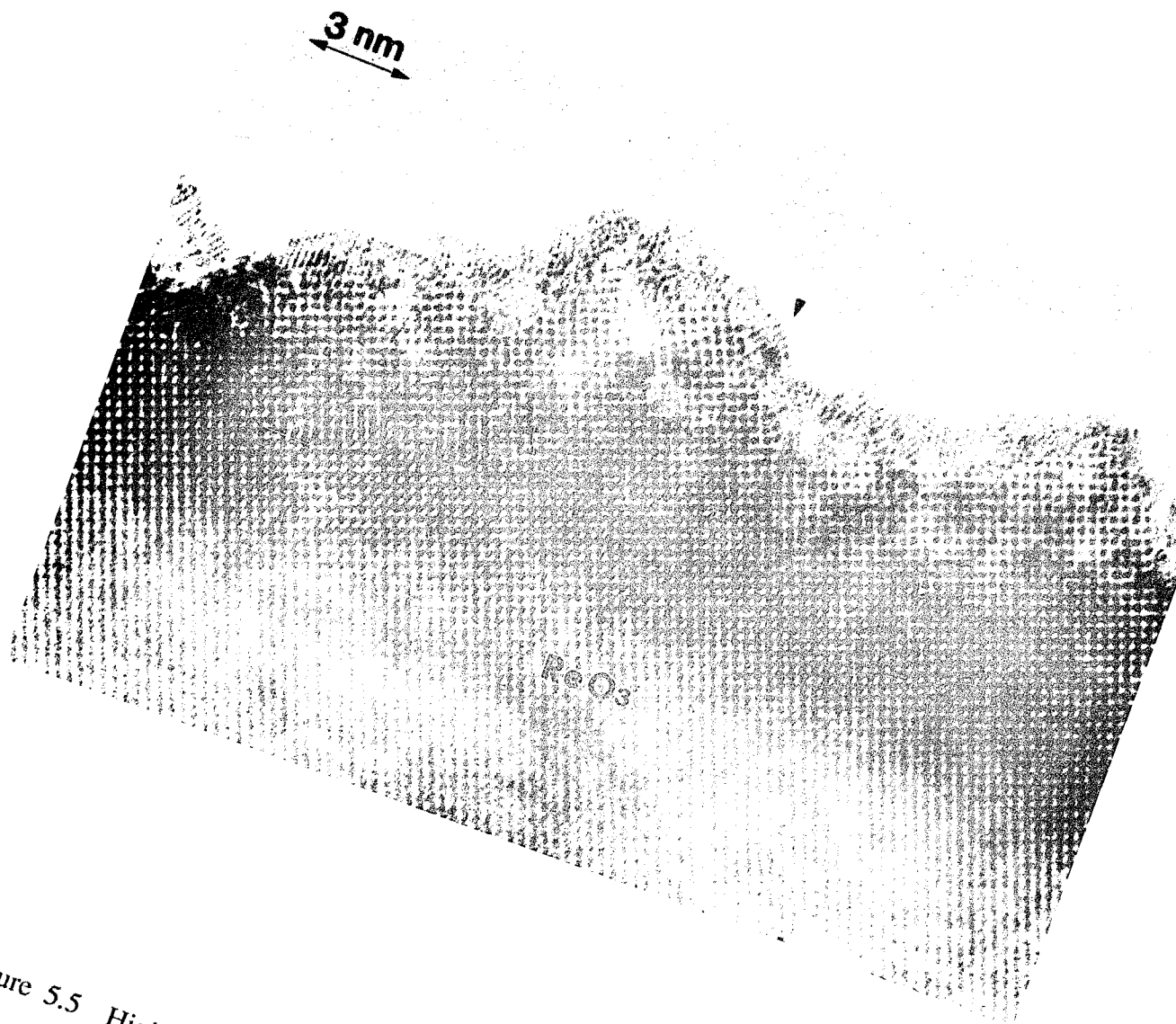
Figure 5.5 High resolution image taken along [100] after about 20 min electron irradiation.
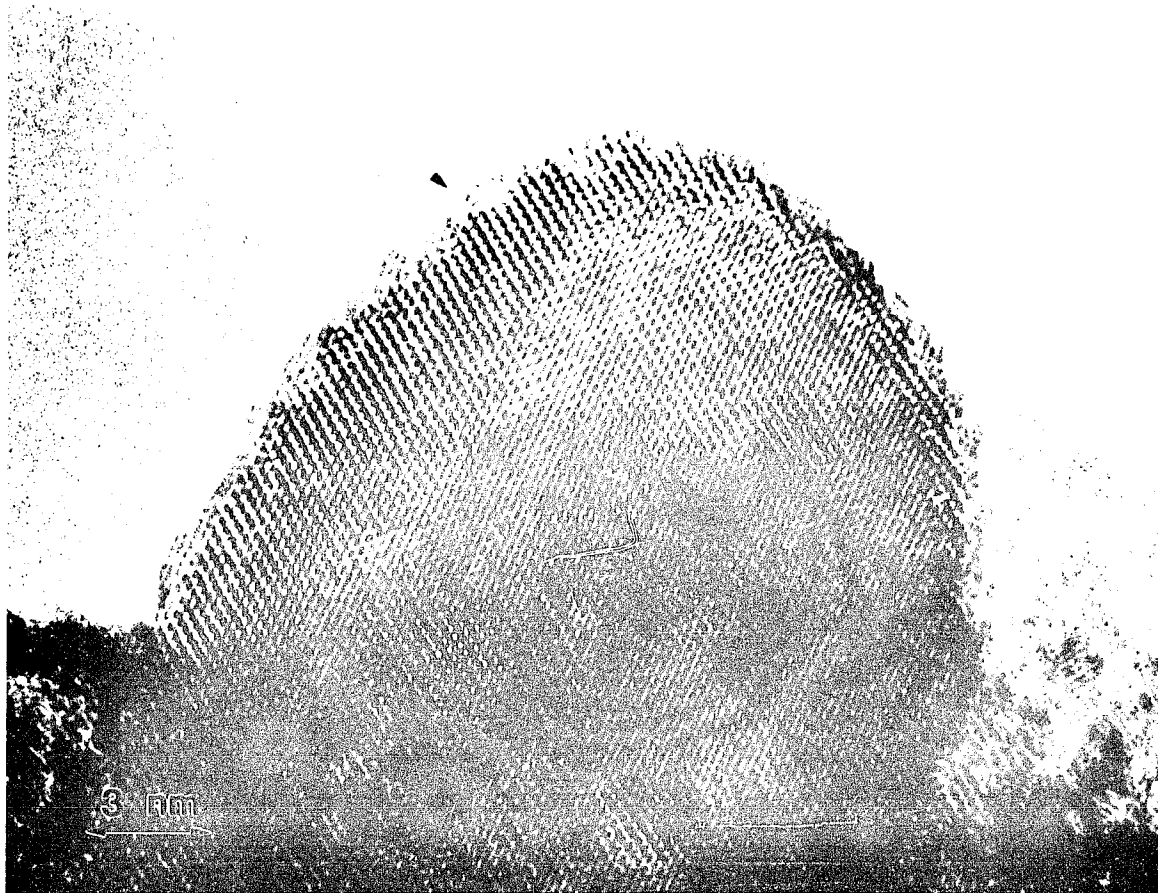
Figure 5.5   High resolution image taken along [112] after about 20 min electron
irradiation.

monitoring the decrease of the ReO_3 grain size in real time as shown in Figure 5.7. The result is shown in Figure 5.8 which is a plot of the ReO_3 grain size as a function of time. The data can be approximately fitted by a straight line, suggesting that the kinetics of the reaction are interface-controlled. This type of reactions occurs when the reaction rate is much faster than mass transport across the interface.

To elucidate the mechanism of phase transformation, we repeated the experiment using 100 keV electron irradiation. The same phase transformation occurred, however at a faster rate. This indicates that the phase transformation is not due to high energy processes, but low energy excitations such as core Auger excitations which take place at a faster rate at lower electron energies.

Non-UHV on Silica (SiO) Substrates

More by accident than design, we repeated the experiment on SiO substrates. It was found that during the observations, 50% of the time the same phase transformation took place, and the other 50% of the time it did not. Prior to a minor maintenance of the instrument, no reaction was observed; after it reactions occurred. In a conventional microscope, there is too little control of the conditions to make any conclusions. However, it would be fair to conclude that the background gases were different in the two conditions.

UHV on Carbon Substrates

In a non-UHV environment, the time for surface observation is on the order of a few
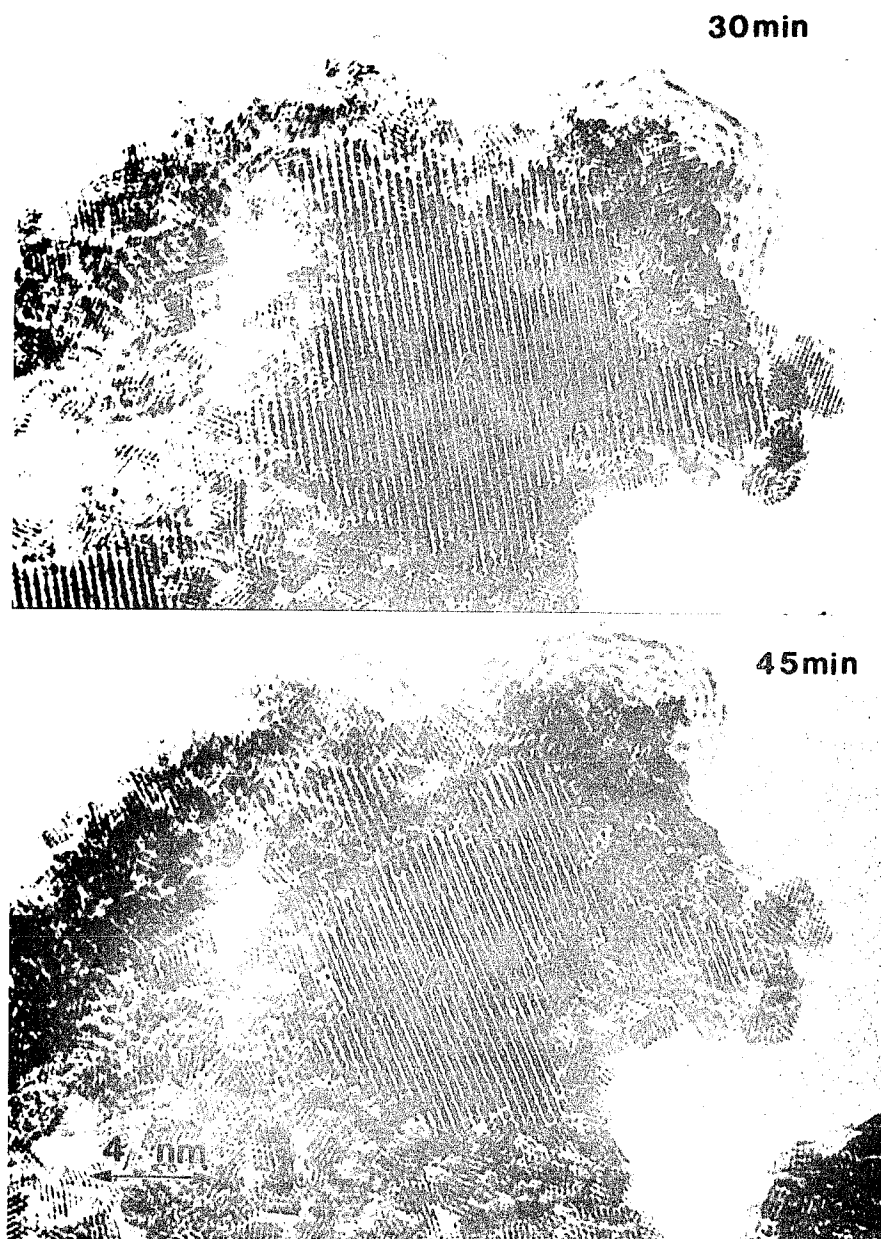
30min

45min

Figure 5.7 High resolution images taken along [110] showing the decrease of a ReO₃ grain with increasing electron irradiation time. a) 30 min; b) 45 min.
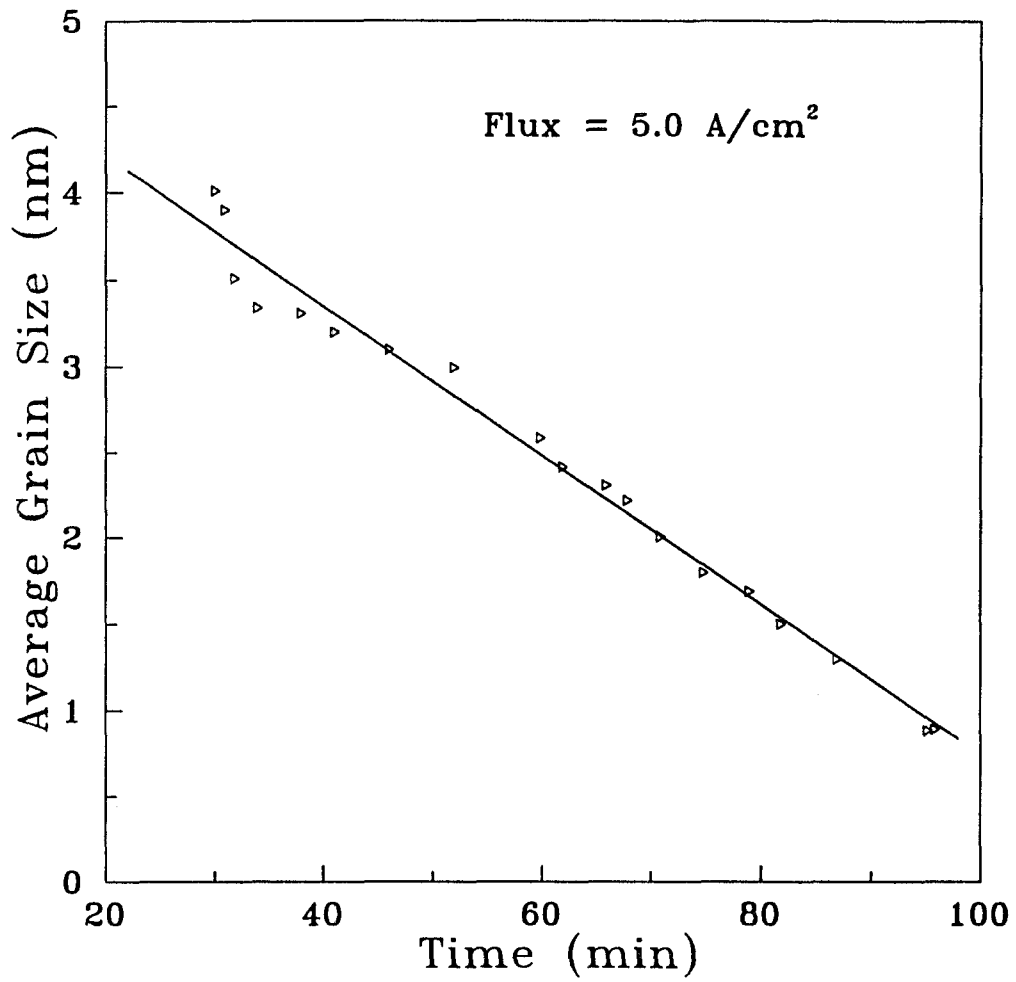
Figure 5.8   A plot of the ReO₃ grain size as a function of time.

seconds for most materials. That means that as soon as samples are loaded into the microscope, the surface of the specimen is contaminated. Under electron beam irradiation, this thin layer of contaminants can actively interact with the final phase or substrates leading to a misleading conclusion about the true effects of electron irradiation. Other interferences can also occur as a result of interaction with the gaseous species in the vacuum. For example, in the case of WO_3, in the non-UHV environment, the final phase observed is WO or WC, but W is the final product in the UHV environment (Singh 1991). This illustrates the necessity of performing experiments in a controlled environment.

The experiment was repeated in the UHV environment of the Hitachi UHV H-9000 electron microscope and on a carbon substrate. Figure 5.9 shows the high resolution images taken along [011], showing that the same phase transformation occurred, ruling out the possibility of interactions with the gaseous species in the vacuum. Note that this was with a carbon substrate and the surface cleanness of the sample was in contrast to the images shown in Figure 5.4 where at thin layer of amorphous contaminants can been clearly seen.

UHV on Silica Substrates

For the UHV observation on a silica substrate, samples were cleaned by annealing at about 600°C for about half hour in high purity oxygen gas with a partial pressure of 1 torr in the side chamber just before being loaded into the UHV microscope. Samples after annealing had a clean surface as observed by high resolution images. Under these
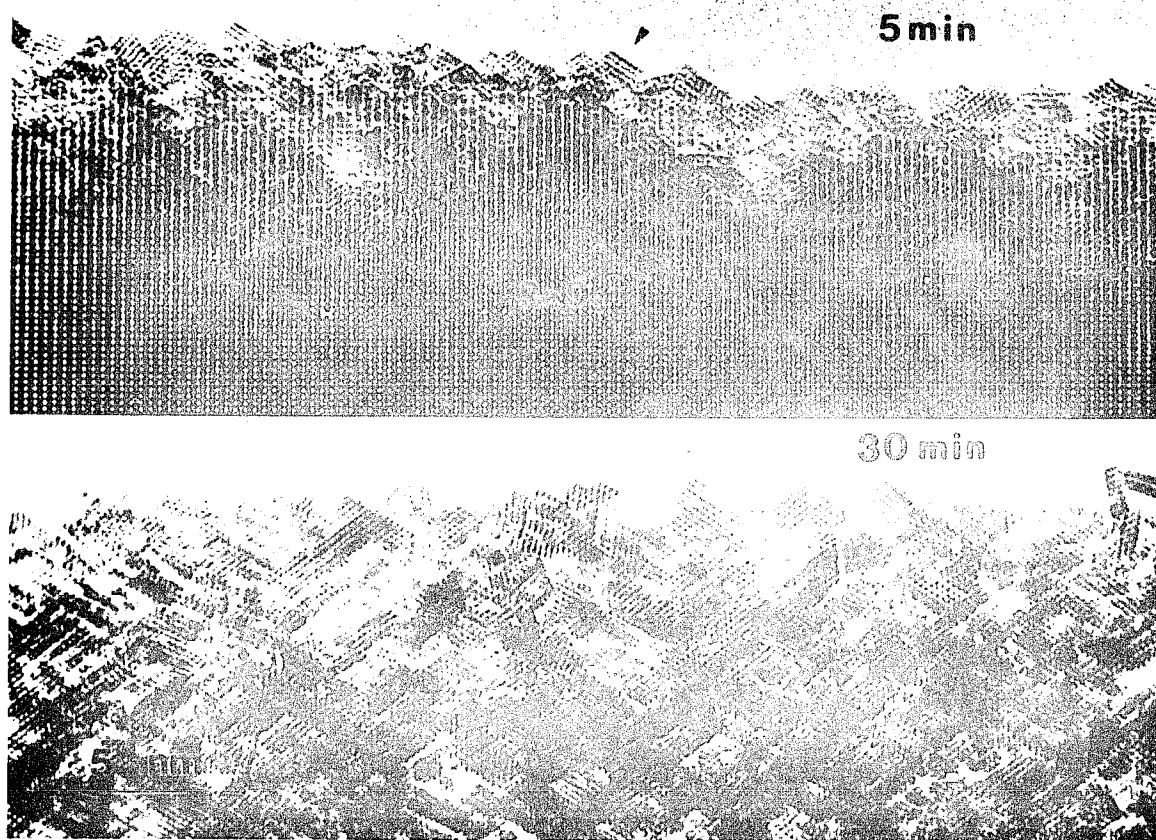
Figure 5.9   Time sequence of high resolution images taken along [011] in UHV after
a) 5 min; b) 30 min electron irradiation.

conditions, it is observed that electron beam irradiation has no effect on the ReO_3 crystals, indicating that the clean ReO_3 crystals in a carbon free environment are stable under electron irradiation.

§5.4.2 Surface Reaction and Damage in CaF_2

CaF_2 was found to be particularly sensitive to electron irradiation. A stable phase, CaO, was formed as soon as the specimen was exposed to the electron beam. The same results were observed in both non-UHV (2×10^{-7} torr) and UHV (2×10^{-10} torr) environments, under 100 and 300 keV electron irradiation. Results presented in this section, unless specified, were obtained in the non-UHV environment of the Hitachi H-9000 electron microscope.

Figure 5.10 shows a time sequence of SAED patterns taken from a CaF_2 single crystal along [110] under electron irradiation with a flux of 1.0 A/cm^2 . The appearance and enhancement of the diffraction rings, characteristic of CaO, clearly indicated the formation and growth of a polycrystalline phase of CaO with increasing irradiation time. A detailed indexing of the diffraction rings indicates that CaO has a prefer orientation of [110].

Figure 5.11 is a HREM image taken after about 10 min of electron irradiation. A surface layer of CaO can be clearly seen in this image. The spacing observed is 2.6 Å, corresponding to the d_{111} of CaO. Domains of different sizes can been clearly seen, in agreement with the observation of polycrystalline rings in the diffraction pattern. In some regions of the image, it is noted that CaO has a well defined epitaxial relationship with
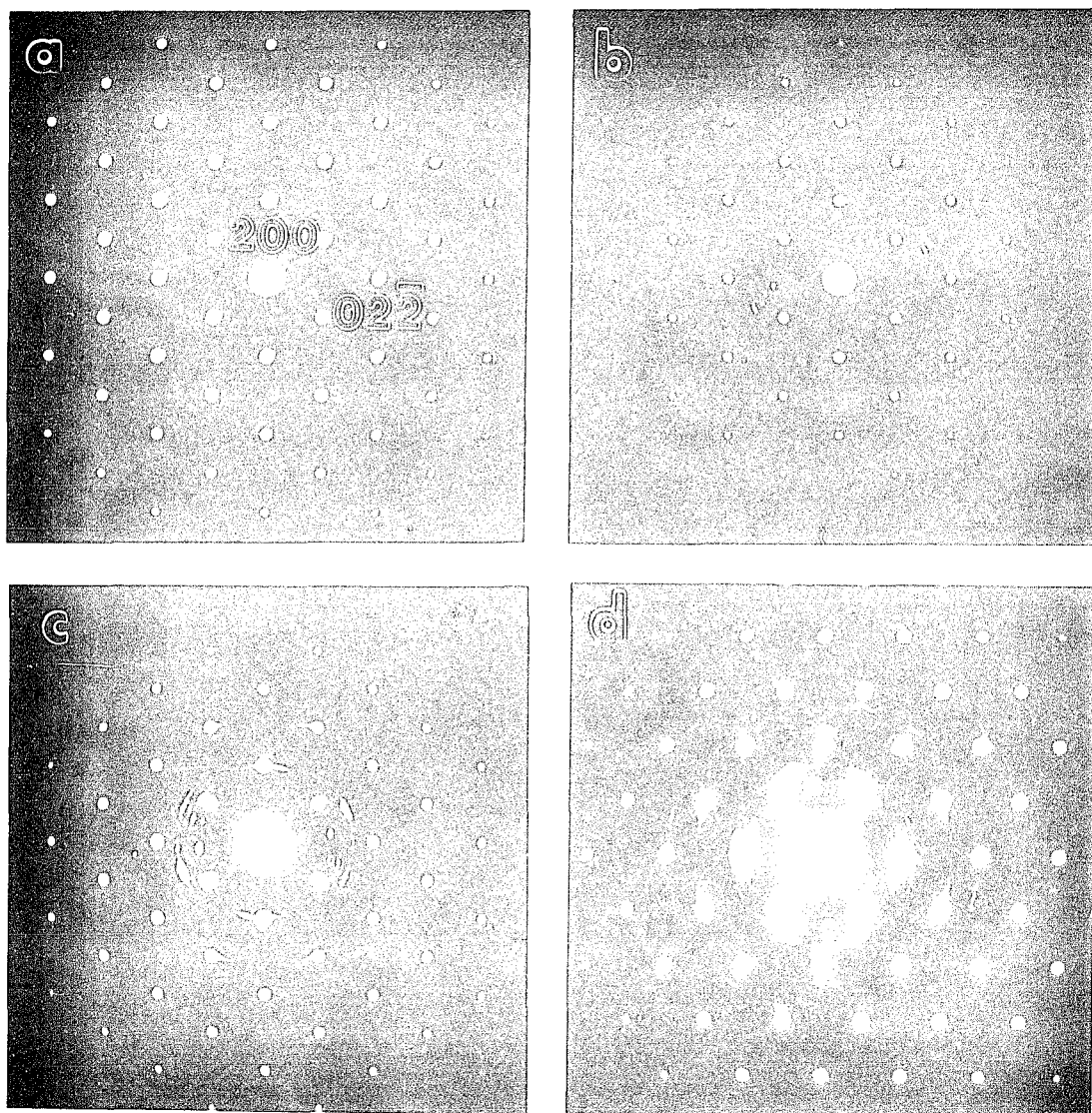
Figure 5.10   Time sequence of SAED patterns taken from CaF$_2$ along [110]. a) initial;
b) 20 min; c) 30 min; d) 60 min.
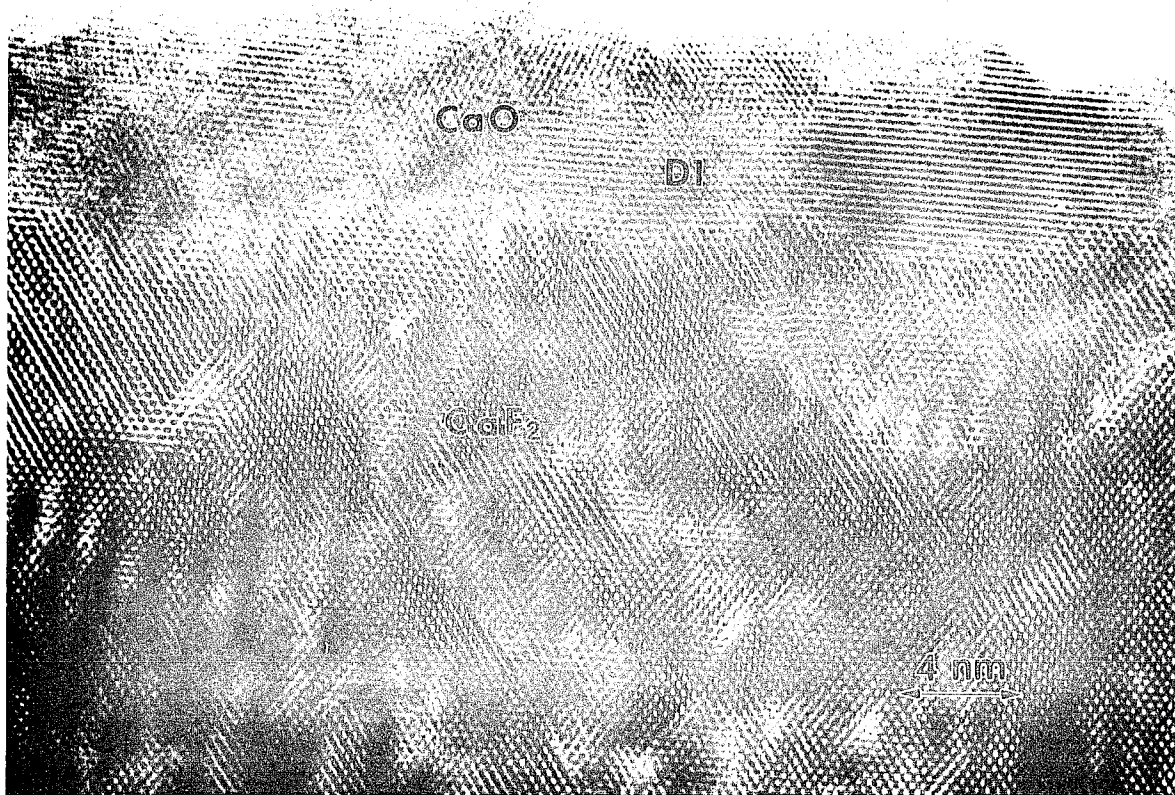
Figure 5.11   HREM image taken after about 10 min electron irradiation at a flux of
1.0 A/cm².

the parent CaF$_2$ phase. For example, in the area marked by "D1", the epitaxial relationship is derived to be the following.

$$(100)\text{CaO} \; // \; (111) \; \text{CaF}_2$$

$$(111)\text{CaO} \; // \; (100) \; \text{CaF}_2$$
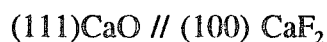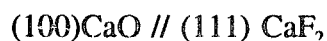
At the surface of CaO, (111) facets were commonly observed. In the bulk, moriè fringes of different spacings were noticed. They are due to the overlapping of CaF$_2$ with the CaO formed on the top or bottom surface of the crystal.

It is interesting to note that the microstructure of CaO varies with experimental conditions. Figure 5.12 is a HREM image taken on a different date under the electron irradiation at the same flux as Figure 5.11. The only difference is the uncontrolled vacuum of the microscope. In this case, CaO formed as a crystalline phase with a well defined orientation relationship with CaF$_2$.

With increasing irradiation time, preferential sputtering of Ca occur along [111] of CaF$_2$ due to the knock-on effect. Rows of Ca atoms on the (111) plane of CaF$_2$ were removed as indicated by arrows in Figure 5.13 taken after 30 min electron irradiation. It should be pointed out that the knock-on effect was only observed in the parent CaF$_2$ phase, implying that Ca in CaO has a higher threshold energy for knock-on displacement. This observation can be understood since CaO has a larger cohesive energy than CaF$_2$.

The same phase transformation was observed in the UHV. Shown in Figure 5.14 is a HREM image taken after 15 min of electron irradiation at a flux of 1.0 A/cm^2 in the UHV environment of the Hitachi UHV H-9000 electron microscope. In this image, formation of CaO can be clearly seen. It is also noted that under UHV condition, the

Figure 5.12 HREM image taken after about 10 min electron irradiation showing the well defined epitaxial relationship between CaO and CaF$_2$.
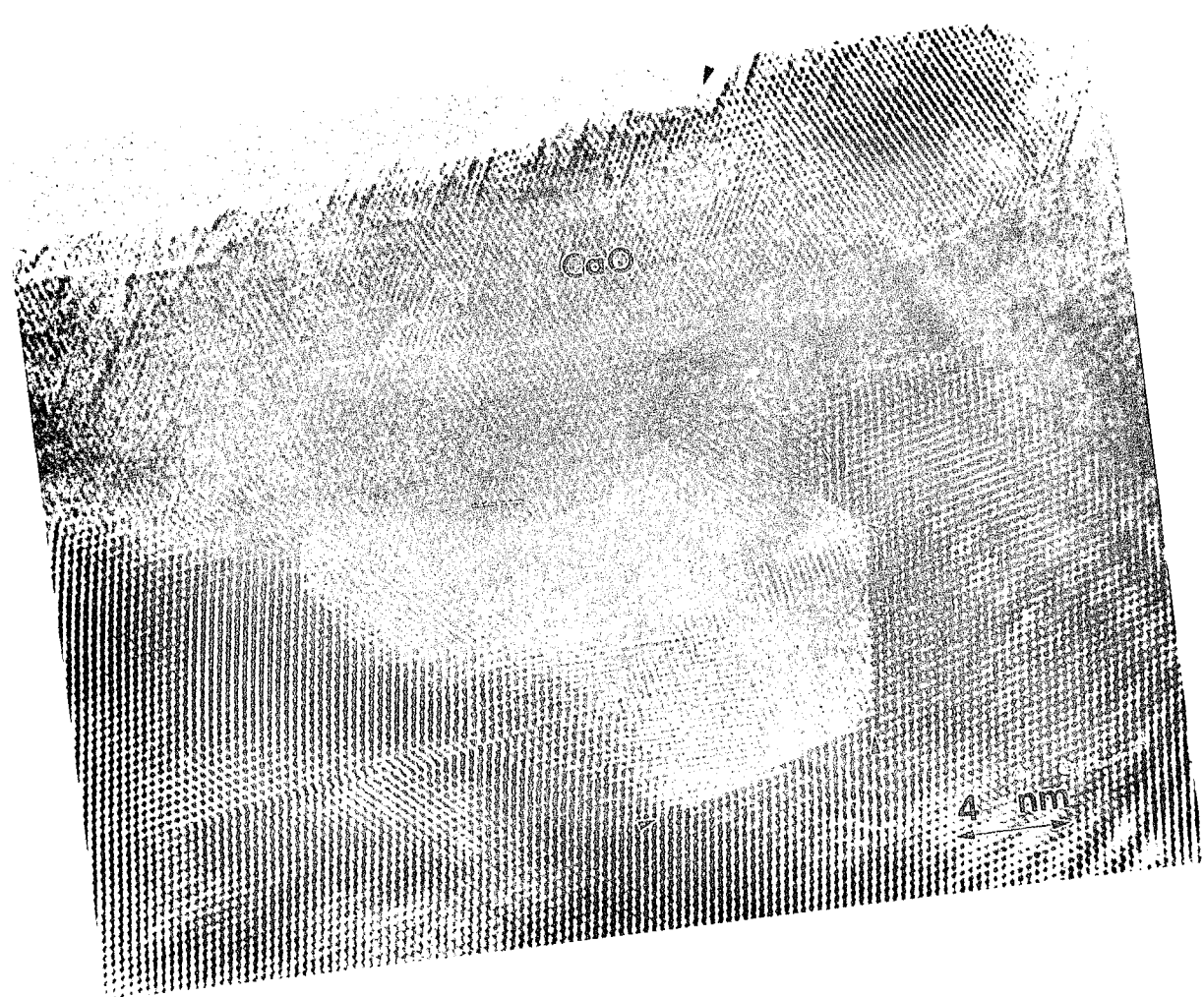
Figure 5.13 HREM image taken after 30 min electron irradiation showing the knock-on effect.

Figure 5.14 HREM image taken after about 30 min electron irradiation in the UHV
environment of the hitachi H-9000 electron microscope.

CaO phase tends to have a smaller domain size and less defined orientational relationship to the parent CaF_2 phase.

§5.5 DISCUSSION

ReO_3

The results of ReO_3 are summarized in Table 5.1. It can be concluded that clean ReO_3 is stable to electron irradiation. This is easy to understand in term of the metallic

Table.5.1 Summary of Effects of electron irradiation on ReO_3

Substrates	Non-UHV	UHV
On Carbon	New Phase	New Phase
On Silica	50% New Phase	No Effect
	50% No Effect	

properties of ReO_3; free electrons in the conduction band rapidly delocalized the electron excitation before it can be transferred into kinetic energy to cause any atomic displacement. The only condition under which the phase transformation took place was in the presence of carbon. The carbon came from two sources: the carbon substrate and the surface hydrocarbon contaminants. Therefore the phase transformation can be attributed to the surface reaction of ReO_3 with carbon, in which the electrons act as a catalyst in the reaction.

From the results, three possible reaction equations can be proposed.

$$ReO_3 + C \rightarrow ReO + CO_2 \qquad (5.1)$$

$$ReO_3 + C \rightarrow ReC + 3\,O_2 \tag{5.2}$$

$$ReO_3 + C \rightarrow ReCO_3 \tag{5.3}$$

In order to elucidate the chemical reaction, the final phase has to be identified. A careful survey of all the thermodynamically stable rhenium compounds revealed no structural match to the new phase. The two possible final phases, ReO and ReC, are not stable at room temperature and atmosphere. Metal carbonates tend to decomposed into either carbides or monoxides under electron beam irradiation. Rhenium is the only d-transition metal that does not form stable carbides. The Re-C phase diagram shows that at room temperature rhenium forms a solid solution with carbon. At high temperatures and high pressures, two polymorphic modifications of rhenium monocarbides are obtained. One is the hexagonal $\tau' = $ MoC type (Popova 1971) and the other one is the cubic NaCl type (Popova 1972). The τ' MoC type rhenium carbide was produced at pressures > 60 kbar and temperatures above 800°C. The cubic type was obtained at a pressure of 160 - 180 kbar and at temperatures of about 1000°C. The lattice parameter of the cubic rhenium carbide was 4.005 ± 0.002 Å. The cubic rhenium carbide is a superconductor with a critical temperature at 3.4 ± 0.2°K. Both rhenium carbides are metastable at atmospheric pressure. Annealing at 1200°C, the τ' MoC type will decompose into a rhenium-carbon solid solution. The cubic rhenium carbide decomposes at about 1000°C. Since the new phase has the same structure and lattice parameter as ReC, it can be therefore identified to be ReC. In the microscope, the ReC was stabilized by electron beam at room temperature and in UHV. The chemical reaction can be written as equation (5.2).

The undamaged ReO_3 crystal is usually covered by a thin layer of hydrocarbon

contaminants introduced during sample preparation. Under electron irradiation the hydrocarbon contaminants decomposed into carbon that reacted with ReO_3 to form ReC. At the same time surface reaction took place in the ReO_3 in contact with the holey carbon substrate. The ReC phase is polycrystalline with a preferred orientation of <110>, and an average domain size of 1 nm. This observation indicates that the reaction process could be is controlled by nucleation, i.e. the ReC nucleated at such a fast rate that the grain did have time to grow. Another explanation for this observation is that grain boundary diffusion is the dominate diffusion process and diffusion through lattice can be ignored. The observation of the <110> preferred orientation confirmed the existence of the "electron wind" in electron microscopy (Marks & Zhang 1989). Marks et al (1992) proposed that momentum transferred by the electron beam to the solid during elastic scattering could be equivalent to an electron wind of velocity of up to 200 miles/hour. Particles under this wind are consequently force to line up with a major zone axis such as <110> along the beam direction.

CaF$_2$

The electron-induced damage in CaF_2 is a multi-stage process: metallization of Ca due the desorption of fluorine followed by the oxidation of Ca to CaO, representing by the following equations.

$$CaF_2 \ -> \ Ca + F^+ \ (F^o) \tag{5.4}$$

$$Ca + H_2O \ (CO, CO_2 \text{ or } O_2) \ -> \ CaO + H_2 \ (C) \tag{5.5}$$
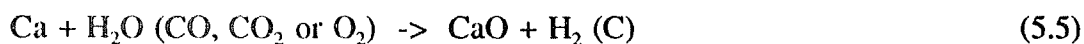
There are two possible mechanisms via which the electron beam can cause desorption of

fluorine. One mechanism is the Pooley-Hersh (Hersh 1966 and Pooley 1965). The other possible mechanism is the K-F mechanism (1978). However, our studies can not clarify which mechanism is operative. It is very possible that the two mechanisms operated simultaneously during electron irradiation. The desorption step proceeds quickly (Tully 1983), typically on the order of 10^{-11} sec, while the diffusion step takes 10^{-3} sec (Buckett 1991). Therefore the reaction rate is limited by the oxidation of Ca to CaO by long range diffusion.

In the experiment, the surface environment plays a important role in determining the oxidation of Ca and the microstructure of the CaO phase. Under the electron beam, Ca was found to be particular sensitive to oxygen and was oxidized by the residual gas components to form CaO. Even at a vacuum of 2×10^{-10} torr, no metallization of Ca were observed. The observation agrees with the results reported by Strecker *et al* (1981). In their studies, metallization of Ca was observed only when the partial pressure of the oxygen containing gases was below 1.0×10^{-10} torr.

The pressure was found to be a major factor in determining the microstructure of CaO. The non-UHV environment favored the growth of large domains of CaO with a well defined orientational relationship to the parent CaF_2 phase. In the UHV environment, small domains of CaO were formed. These observations can be attributed to the increase of the oxygen diffusion rate at the higher oxygen partial pressure.

CHAPTER 6   SUGGESTIONS FOR FUTURE WORK

Electron-induced structural and chemical changes in V_2O_5, ReO_3 and CaF_2 have been investigated systematically. The roles of the controlled experimental parameters such as electron beam energies and fluxes, crystal orientations and surface environments have been evaluated. In light of the results obtained in this work, some future work is proposed.

HREM studies of the effects of low energy electron irradiation in V_2O_5 presented in section 4.3.3 has been the first attempt to bridge the studies in the high energy regime with those in the low energy regime, allowing the electron-induced surface damage to be characterized chemically as well as structurally. From this preliminary study, it is concluded there exist a strong dependency of the microstructure of the damage layers on the electron beam fluxes and energies. For example, the end product of the 3 keV electron irradiation is polycrystalline β-V_6O_{13}, whereas at 300 keV, β-V_6O_{13} formed as a crystalline phase. Further studies are therefore suggested to investigate the effect of electron irradiation of different energies and fluxes on the nucleation an growth of the new phases, which lead to the variations of the microstructure. The experiment can be carried out in the Hitachi UHV H-9000 electron microscope using a 3 mm thin disk of V_2O_5 single crystal. The sample needs to be thin enough for HREM observation and large enough for surface science studies. Samples can annealed in the O_2 and checked for surface chemical stoichiometry by the AES/LEED in the side chamber. An electron gun by Kimball Physics which is capable of delivering electron beam energy up to 10

keV and current to 3 mA can be used as a radiation source. The electron-induced damage can be studied by AES/LEED and HREM as a function of irradiation time, electron energy and fluxes, allowing the various stages of the damage process to be studied. The damaged sample can be replenished in the side chamber by annealing in O_2, allowing the oxidation processes to be studied. The studies of the oxidation and reduction processes in V_2O_5 are important in understanding its catalytic properties.

It is clear from this study that the rate limited step of the phase transformation is diffusion. Since diffusion is a process that strongly depends on temperature, it would be interesting to study the kinetics of the phase transformation under various temperatures. This experiment will allow the roles of the thermal diffusion and electron irradiation assisted diffusion in the damage process to be evaluated and differentiated.

In this study, ReC has been identified by the structural match. A complete phase identification should include the determination of the chemical composition. The experiment can be performed in the VG ESCA lab. The sample can be dosed by carbon under electron beam irradiation in the SIMS chamber and then transferred to the XPS chamber for the study of the surface stoichiometry. This would also allow the changes of the surface chemistry during the reaction to be investigated. Moreover, the microscopy results suggested that the metastable phase ReC is stabilized by electron beam at room temperature and atmosphere. This is a phenomena that is commonly observed during electron microscopy. The formation of V_4O_9 which is not a thermodynamically stable phase is another example. The dissociation of these metastable phases would be an interesting subject to study.

ReO₃ is a metallic oxide and in many ways behaves like metals. It would be interesting to study the dissociation of molecules adsorbed on ReO₃ and compare the results with systems such as CO and NO on metals which have been studied extensively. Even though the study presented provided a indirect evidence of a surface reaction, the exact reaction mechanism is still unclear. Studies of the adsorption of C on ReO₃ can provide insights into the nature of the surface bondings, and therefore the primary electronic excitation and the energy localization during the reaction, allowing the reaction mechanism to be elucidated.

Many improvements are needed for the microscope-compatible AES. One improvement would be the implementation of the constant field mode to eliminate the electron beam drift. The microchannel plate charge particle detector can be replaced by a channeltron detector which has less surface area and therefore less susceptible to x-ray damage.

REFERENCES

Aebi, F. 1948. *Helv. Chim. Acta.* 21: 8.

Ai, R., H.-J. Fan and L. D. Marks. 1991. Electron-induced surface reactions of ReO_3 with carbon. *Surf. Sci.* Submitted.

Antoniewicz, P. R. 1980. Models for electron- and photon-stimulated desorption. *Phys Rev.* B21.9: 3811-3815.

Auger, P. 1925. *J. Phys. Radium* 6: 205.

Austin, I. G. 1962. *Phil. Mag.* 7: 961.

Avouris, P., and R. E. Walkup. 1989. Fundamental Mechanisms of Desorption and Fragmentation Induced by Electronic Transitions at Surfaces. *Annu. Rev. Phys. Chem.* 40: 173-206.

Ayukhanov, A. KL., and E. Turmashev. 1977. *Soc. Phys. - Tech. Phys.* 22: 1289.

Aziz, M. J. and T. Kaplan. 1988. Continuous growth model for interface motion during alloy solification. *Acta. Metall.* 36.8: 2335-2347.

Bachmann, H. G., F. R. Ahmed and W. H. Barnes. 1961. *Z. Krist.* 115: 110.

Banks, B. M., M. J. Miritch, S. K. Rutledge, D. M. Swec and H. K. Nahra. 1985. Ion beam sputter-deposited thin film coating for protection of spacecraft polymers in low earth orbit. *NASA TM 87051*. AIAA 23rd Aerospace Sciences Meeting at Reno, Nevada. (January): 14-17.

Banus, M. D., and T. B. Reed. 1970. *Chemistry of Extended Defects in Non-Metallic Systems.* ed. L. Eyring and M. O'Keefe. 488. Amsterdam: North-holland Publishing Co.

Bareiss, L., Sjolander, and L. Wahlin. 1985. Atomic oxygen stimulated system, design review. *Martin Marieta-Colution Research* MRC-85: 648.

Baunack, S., and A. Zehe. 1990. Electron-beam-induced decomposition and oxidation of thin CaF_2-layers on Si(111) studied by Auger electron spectroscopy. 1990. *Surf. Sci.* 225: 292-300.

Bell, P. S., and M. H. Lewis. 1971. *Phys. Status Solidi* 7: 431-439.

Bleeker, A. J., and P. Kruit. (1990a). A condenser objective lens with asymmetric Polepieces to facilitate the extraction of secondary and Auger electrons. *Rev. Sci. Instr.*

Bleeker, A. J., and P. Kruit. 1990b. The magnetic parallelizer as an optical element for Auger electron: further characterization. *Nucl. Instr. Meth.*

Bonevich, J. E. 1991. Atomic structure and sintering behavior of ultrafine ceramic particles. *Ph.D. Thesis*, Northwestern University: 64-71.

Brenig, W. 1983. The role of the excited state in DIET electronic structure and evolution in Time. In *DIET I Desorption Induced by Electronic Transitions*, ed. N. H. Tolk, M. M. Traum, J. C. Tully and T. E. Madey, 90-101. Berlin: Springer Verlag.

Buckett, M. I., J. Strane, D. E. Luzzi, J. P. Zhang, B. W. Wessel and L. D. Marks. 1989. Electron irradiation damage in oxides. *Ultramicroscopy* 29: 217-227.

Buckett, M. I., and L. D. Marks. 1990. Electron radiation damage in NiO. *Surf. Sci.* 232.

Buckett, M.I. 1991. Electron irradiation damage in transition metal oxides. *Ph.D. Thesis*, Northwestern University: 133-149.

Burns, G. 1985. *Solid State Physics*. London: Academic Press.

Catlow, C. R. A., M. J. Norgett and T. A. Ross. 1977. *J. Phys.* C10: 1627.

Catlow, C. R. A. 1979. *J. Phys.* C12: 969.

Chazelas, J., A. Friederich and J. Cazaux. 1988. *Surf. Interface. Anal.* 11: 36.

Chen, F. F. 1974. *Introduction to Plasma Physics*. London: Plenum.

Christian, J. W. 1981. *The Theory of Transformation in Metals and Alloys*. 2nd ed. New York: Pergamon Press.

Clinton, W. L. 1977. *Phys. Rev. Lett.* 39: 965.

Chuang, T. J. 1983. *Surf. Sci. Rep.* 3: 1.

Colpaert, M. N., P. Clauws, Fiermans and J. Vennik. 1973. Thermal and low energy electron bombardment induced oxygen loss of V_2O_5 single crystal: transition into V_6O_{13}. *Surf. Sci.* 36: 513-525.

Curelaru, I. M., E. Suonien and E. Minni. 1983. An APS-XPS study of vanadium Pentoxide. *J. Chem. Phys.* 78(5): 2262-2264.

Curelaru, I. M. 1980. Electron beam induced decomposition of vanadium pentoxide as seen in appearance potential spectroscopy. *Solid State Commun.* 34: 729-732.

Curelaru, I. M., E. Suoninen, E. Minni, K. G. Strid and T. Ronnhult. 1981. *J. Microsc. Spectrosc. Electron.* 6: 9.

DIET I. 1983. Desorption induced by electronic transition. *Proceedings of the First International Workshop*, ed. N. H. Tolk, M. M. Traum, J. C. Tully and T. E. Madey, Berlin: Springer-Verlag.

DIET II. 1985. Desorption Induced by Electronic Transition. *Proceedings of the Second International Workshop*, ed. W. Brenib and D. Menzel, Berlin: Springer.

DIET III. 1987. Desorption Induced by Electronic Transition. *Proceedings of the Second International Workshop*, ed. R. H. Stulen and M. L. Knotek, Berlin: Springer.

DIET IV. 1989. Desorption Induced by Electronic Transition *Proceedings of the Second International Workshop*, ed. G. Betz and P. Varga, Berlin: Springer.

Dziembaj, R., and J. Piwowarczyk. 1977. Oxygen equilibrium pressure as a measure of oxygen binding energy in the V_2O_{5-x} system. *J. Solid State Chem.* 21: 387-392.

Fan, H. J., and L. D. Marks. 1989. Phase transitions in V_2O_5 in a high resolution electron microscope. *Ultramicroscopy* 31: 357-364.

Farago, P. S. 1970. *Free Electron Physics*. London: Penguin.

Feibelman, P. J. 1981. *Inelastic Particle-Surface Collisions*, ed. E. Taglauer and W. Heiland, 104. Berling: Springer-Verlag.

Fellas, C. N., and S. Richardson. 1981. Internal charging of indium oxide coated mirrors. *IEEE Trans. on Nuclear Science* NS-28.6: 4523-4528.

Ferretti, A., D. B. Rogers and J. Goodenough. 1965. The relation of the electrical conductivity in single crystals of rhenium trioxide to the conductivities of Sr_2MgReO_6 and Na_xWO_3. *J. Phys. Chem. Solids* 26: 2007-2011.

Fiermans, L, and J. Vennik. 1967. *Phys. Letters* A25: 687.

Fiermans, L, and J. Vennik. 1968. LEED study of the vanadium pentoxide (010). *Surf. Sci.* 9: 187-197.

Fiermans, L, and J. Vennik. 1969. Particular LEED features on the V_2O_5 (010) surface and their relation to the LEED beam induced transition: $V_2O_5 \rightarrow V_{12}O_{26}$. *Surf. Sci.* 18: 317-324.

Fiermans, L, and J. Vennik. 1971. Auger electron emission spectroscopy on the V_2O_5 (010) and V (100) surfaces. *Surf. Sci.* 24: 541-554.

Fiermans, L. R. Hoogewijs and J. Vennik. 1975. Electron spectroscopy study of transition metal oxide surfaces. *Surf. Sci.* 47: 1-40.

Fiermans, L., P. Clauws, W. Lambercht, L. Vandenbroucke and J. Vennik. 1980. Single crystal V_2O_5 and lower oxides: a survey of their electronic, optical, structural, and surface properties. *Phys. Stat. Sol.* 59(a): 485-504.

Flood, H., and O. J. Kleppa. 1947. *J. Ame. Chem. Soc.* 69: 998.

Goddard, L. S., and O. Klemperer. 1944. Electron ray tracing through magnetic lenses. *Proc. Phys. Soc.* 56A: 378-396.

Goldstein, J. I., D. E. Newbury, P. Echlin, D. C. Joy, C. Fiori and E. Lifshin. 1984. *Scanning Electron Microscopy and X-ray Microanalysis.* New York: Plenum Press.

Goodenough, J. B. 1971. Metallic oxides. *Prog. Solid State Chem.* 5: 145-393.

Green, B. D., and E. Murad. 1986. The shuttle glow as an indicator of material changes in space. *Planet. Space Sci.* 34.2: 219-224.

Grymonprez, G., L. Fiermans and J. Vennik. 1977. Structural properties of vanadium oxides. *Acta. Cryst.* A33: 834-837.

Harris, L. A. 1968. *J. Appl. Phys.* 39: 1419.

Hayes, W., A. M. Stoneham. 1985. *Defects and Defect Processes in Nonmetallic Solids.* New York: John Wiley & Sons.

Hembree, G. G., F. C. H. Luo and J. A. Venables. 1991. Presented at the 49th Annual Meeting of Electron Microscopy Society of America.

Henrich, V. E. 1985. The Surface of metal oxides. *Rep. Prog. Phys.* 48: 1481- 1541.

Hersh, H. N. 1966. Proposed excitronic mechanism of color-center formation in alkali halides. *Phys. Rev.* 148.2: 928-932.

Hillert, M. 1975. Diffusion and interface control of reactions in alloys. *Metallurgical Transactions* 6A: 5-19.

Ho, W. 1988. *Comments Condens. Matter Phys.* 13: 293.

Hobbs, L. W. 1979. Radiation effects in analysis of inorganic specimens by TEM. In *Introduction to analytical Electron Microscopy*, ed. J. J Hren, J. I. Goldstein and D. C. Joy, 437-480. New York: Plnum Press.

Hock, J. L. and D. Lichtman. 1978. *Surf. Sci.* 77: L184.

Jackson, J. D. 1975. *Classical Electrodynamics.* New York: Wiley.

Jacoby, M., and P. Stair. 1990. Electron stimulated desorption of oxygen from oxidized silver and V_2O_5: a comparison. *Proceedings of the 3th Annual Air Force Workshop on Surface Reactions in the Space Environment.*

Jacoby, M, and P. Stair. 1991. Presented at the 4th Annual Air Force Workshop on Surface Reactions in the Space Environment.

Jeland, W., and D. Menzel. 1973. *Chem. Phys. Lett.* 21: 178.

Kachi, S., T. Takada and K. Kosuge. 1963. Electrical conductivity of vanadium oxides. *J. Phys Soc. Japan* 18: 1839-1840.

Kawano, S. K. Kosuge and K. Kachi. 1966. *J. Phys. Soc.* (Japan) 21: 2744.

Kern, D. P., T. F. Kuech, M. M. Oprysko, A. Wagner and D. E. Eastman. 1988. *Science* 241: 936.

Knotek, M. L., and P. J. Feibelman. 1978a. Ion desorption by core-hole Auger decay. *Phys. Rev. Letters* 40.14: 964-967.

Knotek, M. L. and P. Feibelman. 1978b. Reinterpretation of electron-stimulated desorption Data from chemisorption systems. *Phys. Rev. B* 18.12: 6531-6539.

Knotek, M. L., and P. Feibelman. 1979. Stability of ionically bonded surfaces in ionizing environments. *Surface Science* 90: 78-90.

Knotek, M. L. 1983. Surface chemical information from electron- and photon-stimulated desorption. *Physica Scripta* T6: 94-103.

Knotek, M. L. 1983. Stimulated desorption from surfaces. *Physics Today* (September): 24-32.

Knotek, M. L. 1984. Stimulated desorption. *Rep. Prog. Phys.* 47B: 1499-1561.

Kofstad, P. 1972. *Nonstoichiometry, Diffusion, and Electrical Conductivity in Binary Metal Oxides*. New York: Wiley-Interscience.

Kruit, P., and J. A. Venables. 1988. High-spatial-resolution surface sensitive electron spectroscopy using a magnetic parallelizer. *Ultramicroscopy* 25: 183-194.

Lin, T. T., and D. Lichtman. 1979a. *J Appl. Phys.* 50: 1298.

Lin, T. T., and D. Litchman. 1979b. *J. Mater. Sci.* 14: 455.

Liu, Z. X., and D. Litchman. 1981. *Surf. Sci.* 114: 287.

Lochman, R. E., C. N. R. Rao and J. Honig. 1969. *J. Phys. Chem.* 73: 1781.

Madey, T. E., and J. T. Yates. 1971. *J. Vac. Sci. Technol.* 8: 525.

Madey, T. E., and J. T. Yates. 1977. *Surf. Sci.* 63: 203

Madey, T. E., D. E. Ramaker and R. L. Stockbauer. 1984. *Annu. Rev. Phys. Chem.* 35: 215

Marks, L. D. 1983. Direct imaging of carbon-covered and clean gold(110) surfaces. *Phys. Rev. Lett.* 51: 1000-1002.

Marks, L. D. 1984. Direct atomic imaging of solid surfaces I: image simulation and interpretation. *Surf. Sci.* 139: 281-298.

Marks, L. D. 1985. Image localization. *Ultramicroscopy* 18: 33-38.

Marks, L. D., A. K. Petford and M. O'Keefe. 1986. Atomic imaging of oxygen desorption from tungsten trioxide. *Surf. Sci.* 172: 496.

Marks, L. D., and D. J. Smith. 1983. Direct surface imaging in small metal particles. *Nature* 303: 316-317.

Marks, L. D., and D. J. Smith. 1984. Direct atomic imaging of solid surfaces II: gold(111) surfaces during and after *In-situ* carbon etching. *Surf. Sci.* 143: 495.

Marks, L. D., and J. P. Zhang. 1990. Is there an electron wind? *Proceeding of the 48th Annual Meeting of Electron Microscopy Society of America*: 789-799.

Marks, L. D., and J. P. Zhang. 1992. Is there an electron wind. *Ultramicroscopy* 42: 420-422.

Marks, L. D. 1991. Private communication.

McCartney, M. R., and D. J. Smith. 1989. Epitaxial relationships in electron-stimulated desorption processes at transition metal oxide surfaces. *Surf. Sci.* 221: 214-232.

McCartney, M. R., and D. J. Smith. 1990. Surface structures and rearrangements in oxides." *Materials Research Society Symposium Proceedings* 183: 311-316.

McKliney, W. A., and H. Feshbach. 1948. The coulomb scattering of relativistic Electrons by nuclei. *Phys. Rev.* 74: 1759-63.

Meisel, K. 1932. *Z. Anaorg. Chem.* 217: 121.

Menzel, D. 1975. Electron stimulated desorption: principles and recent developments. *Surf. Sci.* 47: 370-383.

Menzel, D. 1982. *J. Vac. Sci. Technol.* 20: 538.

Menzel, D. 1986. Desorption induced by electronic transitions. *Nucl. Instr. and Methods in Phys. Res.* B13: 5007-517.

Menzel, D., and R. Gomer. 1964. Desorption from metal surfaces by low energy electrons. *J. Chem. Phys.* 41.11: 3311-3328.

Milne, W. E. 1933. On the numerical integration of certain differential equations of the second order. *Amer. Math. Monthly* 40: 322-327.

Morin, F. J. Oxides Which Show a Metal-To-Insulator Transition at the Neel Temperature. *Phys. Rev. Lett.* 3.1 (1959): 34-36.

Mott, N. F. The Scattering of fast electrons by atomic nuclei. *Proc. Roy. Soc.* (London) A124(1929): 425-442.

Niehus, H., W. Losch. 1981. *Surf. Sci.* 111: 344.

Ohno, T., Y. Nakamura and S. Nagakura. 1985. High resolution electron microscopic study of V_6O_{13}. *J. Solid State Chem.* 56: 318-324.

Osgood, R. M., and H. H. Gilgen. 1985. *Annu. Rev. Mater. Sci.* 15: 549.

Outlaw, R. A., W. K. Peregoy, G. B. Hoflund and G. R. Corallo. 1987. Electron stimulated desorption of atomic oxygen from silver. *NASA Technical Paper* 2668: 1-22.

Palmberg, P. W., G. K. Bohn and J. C. Tracy. 1969. *Appl. Phys. Lett.* 26: 182.

Petford, A. K., L. D. Marks and M. O'Keefe. 1986. Atomic imaging of oxygen desorption from tungsten trioxide. *Surf. Sci.* 172: 496-508.

Picht, J. 1939. *Einführung in die Theorie der Elektronenoptik.*

Pooley, D. 1965. F-center production in alkali halides by radiationless electron hole recombination. *Solid State Communications* 3: 241-243.

Popova, S. V., L. N. Fomicheva and L. G. Khvostantsev. 1972. Synthesis and superconducting properties of cubic rhenium monocarbide. *JETP Lett.* 16: 429-430.

Popova, S. V., and L. G. Boiko. 1971. *High Temperature High Pressures* 3: 237.

Powell, C. J. 1976. *Rev. Mod. Phys.* 48: 33.

Purcell, E. M. 1938. The focusing of charged particles by a special condenser. *Phys. Rev.* 54: 818.

Redhead, P. A. 1964. Interaction of slow electrons with chemisorbed oxygen. *Canadian J. Phys.* 42: 886-905.

Reimer, L. 1984. *Transmission Electron Microscopy.* New York: Springer-Verlag.

Saiki, K., Y. Sato, K. Ando and A. Koma. 1987. *In-Situ* observation of defect formation in $CaF_2(111)$ surfaces induced by low energy electron bombardment. *Surf. Sci.* 192: 1-10.

Sakata, K. and T. Sakata. 1969. *Trans. Nat. Res. Inst. Metals* (Japan) 10: 9.

Samsonov, G. V. 1973. *The Oxide Handbook,* 170. New York: IFI/Plenum.

Sata, T. and Y. Ito. 1968. *Kogyo Zasshi* 71: 647.

Satava, V. 1959. *Czech Chem, Commun.* 24: 3291.

Scheinfein, M., and M. Isaacson. 1986. Electronic and chemical analysis of fluoride interface structures at subnanometer spatial resolution. *J. Vac. Sci. Technol.* B4(1): 326-332.

Shin, F. 1992. Private communication.

Singh, S. R., and Marks, L. D. 1992. In preparation.

Singh, S. R., and L. D. Marks. 1989. Diffusion during electron-beam-induced reduction of tungsten trioxide. *Phil. Mag. Lett.* 60.1: 31-36.

Smith, D. J., M. R. McCartney and L. A. Bursill. 1987. The electron-beam-induced reduction of transition metal oxides surfaces to metallic lower oxides. *Ultramicroscopy* 23: 299-304.

Smith, D. J., and L. D. Marks. 1987. Direct atomic imaging of solid surfaces III: small particles and extended Au surfaces. *Ultramicroscopy* 23: 299-304.

Sørensen, O. T. 1981. Thermodynamics and defect structure of nonstoichiometric oxides. *Nonstoichiometric Oxides.* ed. O. T. Sørensen, 2-59. New York: Academic Press.

Strane, J. 1988. Irradiation damage on rutile surfaces observed in a high resolution electron microscope. *M.S. Thesis*, Northwestern University.

Strecker, C. L, W. E. Moddeman and J. T. Grant. 1981. Electron-beam-induced decomposition of ion bombardment calcium fluoride surfaces. *J. Appl. Phys.* 52(1): 6921-6927.

Suoninen, E., I. M. Curelaru and E. Mini. 1981. *J. Microsc. Spectrosc. Electron.* 6: 9.

Takei, H. and S. Koide. 1968. *J. Phys. Soc.* (Japan) 24: 1394.

Taylor, A., and N. J. Doyle. 1970. In *Chemistry of Extended Defects in Non-Metallic Systems.* ed. L. Eyring and M. O'Keefe, 523. Amsterdam: North Holland Publishing Co.

Taylor, N. J. 1969. *Rev. Sci. Instr.* 40: 792.

Théobald F, R. Cabala and J. Bernard. 1969. Action ménagée de certains réducteurs sur V_2O_5; mise en évidence de l'oxyde V_4O_9. *Compt. Rend.* 296c: 1209.

Tilley R. J. D. and B. G. Hyde. 1970. An electron microscopic investigation of the decomposition of V_2O_5. *J. Phys. Chem. Sol.* 31: 1613-1619.

Tompkins, H. G., I. M. Curelaru, K. S. Din, and E. Soninen. 1985. Auger electron spectroscopy observations of the V_2O_5 - V_6O_{13} phase transition. *Application. of Surf. Sci.* 21: 280-287.

Townsend, P. D., R. browning, D. J. Garlant, J. C. Kelly, A. Mahjoobi, A. J. Michael and M. Saidoh. 1976. Sputtering patterns and defect formation in alkali halides. *Radiation Effects* 30: 55-60.

Tully, J. C. 1983. Direct and indirect mechanisms of stimulated desorption. In *Desorption Induced by Electronic Transitions I.* ed. N. H. Talk, M. M. Traum, J. C. Tully and T. E. Madey, 31-38. Berlin: Springer Verlag.

Volpert, V. A, L. D. Marks and R. Ai. 1992. Phase transition kinetics of vanadium pentoxide II: theoretical results. In preparation.

Yin, L. I., T. Tsang, G. J. Coyle, W. Yin and I. Adler. 1982. Relative intensity changes of L_3MM Auger transitions in maximal-valent V and Cr compounds under Ion bombardment. *Phys. Rev.* B26: 1093-1098.

Yin, L. I., T. Tsang, G. J. Coyle, W. Yin and I. Adler. 1983. Interatomic Auger transitions in maximal valent V and Cr compounds. *J Vacuum Sci. Technol.* A1: 1000-1003.

Yu, M. L. 1979a. *Surf. Sci.* 84: 493.

Yu, M. L. 1979b. *Phys. Rev.* B19: 5995.

Wilhelmi K. A. and K. Waltersson. 1970. On the structure of a new vanadium oxide, V_4O_9. *Acta. Chem. Scand.* 24.9: 3409-3411.

Wilhelmi, K. A., K. Waltersson and L. Kihlborg. 1971. A refinement of the crystal Structure of V_6O_{13}. *Acta. Chem. Scand.* 25: 2675-2687.